

**ALKALINE POLYMER ELECTROLYTE WITH SUB-ZERO CONDUCTIVITY
FOR ZINC-AIR BATTERIES**

by

Chun Keat Khor

Bachelor of Science (Chemistry, UNB, 2021)

A Thesis Submitted in Partial Fulfillment
of the Requirements for the Degree of

Master of Science

in the Graduate Academic Unit of Chemistry

Supervisor: Anna Ignaszak, Ph.D., Chemistry

Examining Board: C. Adam Dyker, Ph.D., Chemistry
Allison Enright, Ph.D., Earth Science

This thesis is accepted by the
Dean of Graduate Studies

THE UNIVERSITY OF NEW BRUNSWICK

July, 2022

©Chun Keat Khor, 2022

Abstract

Due to the increasing demand for flexible electronics that can function in harsh environments, research on flexible solid-state batteries, especially zinc-air batteries (ZAB), is expanding. However, the electrolyte in the current commercially available ZAB still suffers from drying out after prolonged exposure to air. Here, the synthesis of a flexible conductive hydrogel electrolyte that can function at low temperatures was attempted. The polymer chain was made up of potassium polyacrylamide-co-acrylate and crosslinked using N,N'-methylenebisacrylamide. Three variants of cellulose were added to improve the stretchability of the hydrogel. We found out that acrylamide decomposed in the high concentration of base required for ZAB electrolyte. Further understanding of the polymer chains had helped improve our hydrogel design, which can tolerate high molarity of base and functions at -23°C . Electrochemical studies were carried out to understand the charge transport properties of the electrolyte in the hydrogel.

Dedication

I would like to dedicate this thesis to all the individuals in my professional or personal life that have helped or guided me throughout this memorable journey.

Acknowledgements

I would like to acknowledge all the people that have assisted and supported me throughout my work on this thesis. Firstly, I would like to thank all my family members who have been very supportive of my decision on acquiring a graduate degree in Canada, a country halfway across the globe from Malaysia. Next, I would like to thank Dr. Anna Ignaszak, my project supervisor, who has been immensely helpful throughout the entirety of the project. Besides that, I would like to thank Dr. Andreas Decken, Dr. Barry A. Blight, Dr. C. Adam Dyker, Dr. James Tait, Dr. Yang Qu, and Mr. Michael Paul Albright for all the suggestions and assistance with various techniques and instruments used throughout this thesis. I would also like to thank all the past and current members of Dr. Ignaszak's research group who have assisted and supported me in any ways. I had a lot of fun working in this research group. Last but not least, I would like to thank Dr. Gilles Villemure, Dr. Yang Qu, Dr. C. Adam Dyker, and Dr. Allison Enright, who are reading and examining this thesis.

Table of Contents

Abstract	ii
Dedication	iii
Acknowledgements	iv
Table of Contents	v
List of Tables	viii
List of Figures	ix
List of Symbols and Nomenclatures	xiii
1 Introduction	1
1.1 Metal-Air Batteries	2
1.2 Hydrogel	5
1.3 Crosslinker	6
1.4 Electrolyte System for ZAB	7
1.5 Recent Work on Hydrogel Synthesis for ZAB	8
1.6 Electrochemical Studies on Hydrogel	10
1.7 Project Goals	11
2 Theory	13
2.1 Ohm's Law	13
2.2 Voltage and Current in Alternating Current (AC) Circuits	13
2.3 Current Lag and Lead in Inductor and Capacitor	17
2.4 Inductive and Capacitive Reactance	19
2.5 Nyquist Plot	22
2.6 Nyquist Plot of an Electrolyte Material	23

2.7	Relationship between Time Expression and Loss Tangent.....	26
2.8	Calculation of Charge Transport Properties.....	28
3	Experimental.....	30
3.1	Chemical Reagents Used in Synthesis	30
3.2	General Considerations	30
3.3	Synthesis of Hydrogels.....	31
3.4	Analysis of Hydrogels.....	35
4	Results and Discussion	39
4.1	Effect of Concentration of KOH	39
4.2	Effect of KOH and Zinc Acetate Addition.....	47
4.3	Addition of Cellulose	52
4.4	Questioning Our Methodology	55
4.5	New Formulation.....	56
4.6	Potassium Polyacrylate Hydrogel with Glycerol: Synthesis, Freezing and Mechanical Properties.....	58
4.7	Charge Transport Properties Analysis.....	63
5	Conclusion and Future Work.....	73
6	Appendix	76
6.1	FTIR Spectra	76
6.2	Experimental Nyquist plot	80
6.3	Calculation of Charge Transport Properties.....	87
7	References	89

Curriculum Vitae

List of Tables

Table 1.5.1: Development of hydrogels for ZABs in the last four years and their reported ionic conductivity.....	10
Table 3.2.1: List of hydrogels synthesized, the chemical compositions, and their respective label for ease of discussion. Capital ‘B’ and ‘Z’ in the label stands for base and zinc acetate respectively. The subscript followed represents the concentrations. (a) An AM gel refers to hydrogel made from acrylamide and potassium acrylate monomer with MBAA as a crosslinker. (b) An acrylate-only gel refers to hydrogel made from potassium acrylate monomer only with MBAA as crosslinkers.....	31
Table 4.5.1: Comparison between the old formulation and the new formulation.	58
Table 4.6.1: Chemical compositions of the prepared sample to study the antifreeze properties of the electrolyte system and not the hydrogel.	61
Table 4.7.1: The mean and standard deviation (Std. Dev) of σ and D for two KPA samples.....	70
Table 4.7.2: The mean and standard deviation (Std. Dev) of μ and n for two KPA samples	70
Table 6.2.1: Values of ionic conductivity of KPA based on R_{bulk} determine through fitting	86
Table 6.2.2: Values of ionic conductivity of KPA-Gly based on R_{bulk} determine through fitting.....	86
Table 6.3.1: Values of $\tan(\phi)$ extrapolated from plotting Z'/Z'' against frequency of KPA	87
Table 6.3.2: Calculated values of D , μ , and n of KPA	87
Table 6.3.3: Values of $\tan(\phi)$ extrapolated from plotting Z'/Z'' against frequency of KPA-Gly.....	88
Table 6.3.4: Calculated values of D , μ , and n of KPA-Gly	88

List of Figures

Figure 1.1.1: Bar chart of the volumetric energy density of different MABs and commercially available LIB.....	3
Figure 1.3.1: Two main types of crosslinking in hydrogel, blue: physical crosslinking, and red: chemical crosslinking.....	6
Figure 2.2.1: Circuits with a resistor, capacitor, or an inductor connected to an AC power source.	14
Figure 2.3.1: Sinusoidal graph for voltage and current across a resistor when AC power source is applied. The maximum and minimum (amplitude of wave) are different so that the graphs are not overlapped. Hence, the difference in value should be ignored.	17
Figure 2.3.2: Sinusoidal wave for an inductor connected to an AC power source.....	18
Figure 2.3.3: Sinusoidal wave for a capacitor connected to an alternating current.	19
Figure 2.4.1: Diagram of RL circuit (left) and RC circuit (right).....	20
Figure 2.4.2: Vector arrows of resistance and reactance drew on a complex plane to find out the total impedance for RL and RC circuits.	21
Figure 2.6.1: A typical circuit of a capacitor connected to a power source. The ovals between the two electrodes represent molecules of the dielectric being polarized.	23
Figure 2.6.2: Schematic diagram of an electrolytic material connected to a power source, creating an electrical double layer (EDL).	25
Figure 2.6.3: Nyquist plot with a semicircle and a spike (left) and an equivalent circuit to represent the shape of the Nyquist plot (right). The arrow on top of the spectra shows the angular frequency of the AC voltage, where ω_{∞} and ω_0 represent the angular frequency approaching infinity and zero respectively. The numbers on the axis are just an example and they should not be treated as actual values.	26

Figure 2.7.1: Same Nyquist plot with a semicircle and a spike as Figure 2.6.3 (left). The real and imaginary part of impedance from a Nyquist plot with a semicircle and a spike plotted against frequency (right). Arrows show the angular frequency when Z'' is at its maximum and minimum. Recall that the negative signs of the imaginary part of the impedance, Z'' , only denotes the capacitive behavior (capacitive reactance) of the material and should be left out when comparing the values. 27

Figure 3.3.1: Photo of a mold used to form hydrogels with a specific shape in an ultrasonic bath..... 34

Figure 3.4.1: Images of equipment used for mechanical and tensile experiments; (a) a full image of the machine, (b) when the hydrogel is clamped, (c) when the hydrogel is being elongated. 36

Figure 3.4.2: Miniature experimental setup that is able to fit the freezer in our laboratory. 38

Figure 4.1.1: Photos of freshly synthesized hydrogels with different concentrations of KOH solution. (A) $B_{1.5}Z_{0.2}$, (B) $B_{3.0}Z_{0.2}$, (C) $B_{4.5}Z_{0.2}$, and (D) $B_{6.0}Z_{0.2}$ 40

Figure 4.1.2: Bar chart of the max load (red) and percentage of stretch (blue) of $B_{1.5}Z_{0.2}$, $B_{3.0}Z_{0.2}$, and $B_{4.5}Z_{0.2}$ 42

Figure 4.1.3: Experiment to identify the release of ammonia gas. (A) Color of pH paper before the experiment, (B) color of pH paper when exposed to hydrogel, and (C) color of pH paper when exposed to concentrated HCl..... 44

Figure 4.1.4: FTIR spectra of $B_{0.0}Z_{0.2}$, $B_{1.5}Z_{0.2}$, $B_{3.0}Z_{0.2}$, and $B_{4.5}Z_{0.2}$ stacked together for comparison..... 45

Figure 4.1.5: Spectra of total impedance for $B_{1.5}Z_{0.2}$, $B_{3.0}Z_{0.2}$, and $B_{4.5}Z_{0.2}$ as these hydrogels were elongated 46

Figure 4.2.1: Photos of synthesized hydrogels; (A) $B_{0.0}Z_{0.0}$, (B) $B_{0.0}Z_{0.2}$, (C) $B_{3.0}Z_{0.0}$, and (D) $B_{3.0}Z_{0.2}$. $B_{3.0}Z_{0.2}$ is added into the group for side-by-side comparison.	48
Figure 4.2.2: Bar chart of the max load (red) and percentage of stretch (blue) of $B_{0.0}Z_{0.0}$, $B_{0.0}Z_{0.2}$, $B_{3.0}Z_{0.0}$, and $B_{3.0}Z_{0.2}$	49
Figure 4.2.3: Spectra of total impedance for $B_{0.0}Z_{0.0}$, $B_{0.0}Z_{0.2}$, $B_{3.0}Z_{0.0}$ and $B_{3.0}Z_{0.2}$ as these hydrogels were elongated.	51
Figure 4.3.1: Images of freshly synthesized hydrogels with different variants of cellulose. (A) $B_{3.0}Z_{0.2}$ -Cell, (B) $B_{3.0}Z_{0.2}$ -CMC, and (C) $B_{3.0}Z_{0.2}$ -HPC	52
Figure 4.3.2: Bar chart of the max load (red) and percentage of stretch (blue) of $B_{3.0}Z_{0.2}$, $B_{3.0}Z_{0.2}$ -Cell, $B_{3.0}Z_{0.2}$ -CMC, and $B_{3.0}Z_{0.2}$ -HPC	53
Figure 4.3.3: Spectra of total impedance for $B_{3.0}Z_{0.2}$, $B_{3.0}Z_{0.2}$ -Cell, $B_{3.0}Z_{0.2}$ -CMC, and $B_{3.0}Z_{0.2}$ -HPC as these hydrogels were elongated.	54
Figure 4.6.1: Low-temperature tests of KPA and KPA-Gly in (A) $-25\text{ }^{\circ}\text{C}$ and (B) $-80\text{ }^{\circ}\text{C}$	59
Figure 4.6.2: Photos of 5 mL samples of different chemical compositions before and after they were frozen. These samples were prepared to study the antifreeze properties of the electrolyte system and not the hydrogel.....	61
Figure 4.6.3: Bar chart of the max load (red) and percentage of stretch (blue) of KPA and KPA-Gly.	62
Figure 4.7.1: Nyquist plot of KPA without any elongation recorded at room temperature ($23\text{ }^{\circ}\text{C}$).....	64
Figure 4.7.2: The circuit diagram used to describe all KPA and KPA-Gly spectra recorded. CPE stands for Constant Phase Element. It is a common element used to describe the behavior of a non-ideal capacitor.	65

Figure 4.7.3: Bar charts of the fitted ionic conductivity values of charge transport properties of KPA and KPA-Gly at 23°C (A) and -23°C (B).....	66
Figure 4.7.4: Bar charts of all the calculated charge transport properties of KPA and KPA-Gly at 23°C (A, C, E) and -23°C (B, D, F).....	68
Figure 6.1.1: FTIR spectrum of B _{0.0} Z _{0.2}	76
Figure 6.1.2: FTIR Spectrum of B _{1.5} Z _{0.2}	77
Figure 6.1.3: FTIR spectrum for B _{3.0} Z _{0.2}	78
Figure 6.1.4: FTIR spectrum for B _{4.5} Z _{0.2}	79
Figure 6.2.1: Nyquist plot of KPA at 23°C.....	80
Figure 6.2.2: Nyquist plot of KPA at 23°C after 50% elongation.....	80
Figure 6.2.3: Nyquist plot of KPA at 23°C after 100% elongation.....	81
Figure 6.2.4: Nyquist plot of KPA at -23°C.....	81
Figure 6.2.5: Nyquist plot of KPA at -23°C after 50% elongation.....	82
Figure 6.2.6: Nyquist plot of KPA at -23°C after 100% elongation.....	82
Figure 6.2.7: Nyquist plot of KPA-Gly at 23°C.....	83
Figure 6.2.8: Nyquist plot of KPA-Gly at 23°C after 50% elongation.....	83
Figure 6.2.9: Nyquist plot of KPA-Gly at 23°C after 100% elongation.....	84
Figure 6.2.10: Nyquist plot of KPA-Gly at -23°C.....	84
Figure 6.2.11: Nyquist plot of KPA-Gly at -23°C after 50% elongation.....	85
Figure 6.2.12: Nyquist plot of KPA-Gly at -23°C after 100% elongation.....	85

List of Symbols and Nomenclatures

μ	Mobility of Ions
AC	Alternative Current
APS	Ammonium Persulfate
CMC	Sodium Carboxymethyl Cellulose
D	Diffusion Coefficient
DC	Direct Current
EIS	Electrochemical Impedance Spectroscopy
FTIR	Fourier Transform Infrared
HPC	Hydroxypropyl Cellulose
LIB	Lithium-Ion Battery
MAB	Metal-Air Battery
MBAA	N'N-methylenebisacrylamide
MXene	A class of two-dimensional inorganic compounds, usually carbides or carbonitrides
n	Charge Density
NaPA	Sodium Polyacrylate
PAN	Polyacrylonitrile
PEO	Polyethylene Oxide
RC	Resistive-Capacitive
RL	Resistive-Inductive
Std. Dev	Standard Deviation
TMEDA	N,N,N',N'-tetramethylethyldiamine
UV	Ultraviolet
ZAB	Zinc-Air Battery
Zn(Ac) ₂	Zinc Acetate

1 Introduction

Humans have come a long way in terms of generating electricity. For over a century, we were able to sustain most of the world's electricity demand by burning fossil fuels. Fossil fuel is not a renewable resource, and it generates a lot of greenhouse gases, such as carbon dioxide (CO₂) and methane (CH₄), during combustion.¹ As a solution to fossil fuel power generation, clean energy technologies are paving the way to a carbon-free, or more realistically, carbon-reduced era. Thus, many countries are moving away from fossil fuel power plants, replacing them with renewable energy sources such as hydroelectric, solar energy, or wind power. Without a doubt, the above-listed renewable energy sources are great contributors toward carbon-reduced electrification.

Hand-in-hand with renewables, the second most important clean energy technologies are batteries, fuel and flow cells, and supercapacitors. Coupling them with renewable energy sources (creating a regenerative energy storage system) is an innovative approach that will lead to a cleaner future. This system is considered one of the most promising off-grid energy supplies. Unlike fossil fuel power plants, where these power plants can control the amount of energy produced by burning variable amounts of fuel, renewable energy power plants are unable to control the amount of energy harvested as they depend on natural phenomena. Hence, energy storage systems have to be integrated with renewables to collect the excess energy produced on certain days, such as during more sunny or windy seasons, so it can be used to energize facilities during nights or when higher electrical power demand is needed. As such, many ongoing projects already deal with prototyping various off-grid facilities, from small-scale (a single household) to large

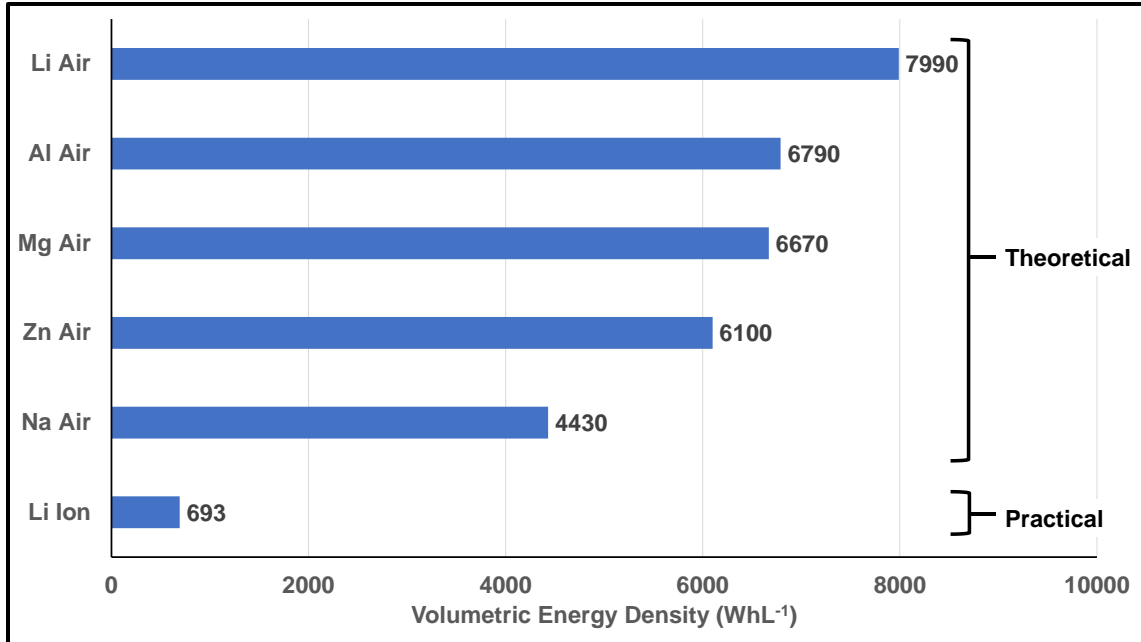
industrial self-sustained infrastructure (airport) that will help minimize overall carbon footprint and mitigate climate change.

This project focuses on an energy storage system, aiming to develop new functional materials that will hopefully contribute to discovering a battery with improved technical features and lifetime. Although this sounds like an obvious goal for many scientists and engineers, why do we still search for better sustainable power? What is the major issue regarding the currently available batteries? The majority of rechargeable batteries that are available in the market are lithium-ion batteries (LIB). Ever since the invention and commercialization of LIBs, the demand for the third element in the periodic table, lithium, has increased drastically. The lithium extraction process, on the other hand, is much slower. Unable to keep up with the ever-growing demand, the lithium shortage problem has become concerning.² Hence, a lot of research has been done to provide alternatives to LIBs.

1.1 Metal-Air Batteries

Metal-air batteries (MAB) are among the more promising batteries that can complement LIBs. A MAB contains an electrolyte system, either aqueous or non-aqueous, sandwiched between a metal electrode (e. g., Mg, Al, Zn, Na) and an air electrode. The air electrode often consists of two layers: a gas diffusion layer which facilitates diffusion of air from the surrounding into the battery system; and a catalyst layer which promotes oxygen reduction reaction.³

Figure 1.1.1: Bar chart of the volumetric energy density of different MABs and commercially available LIB.³ The energy density LIB is categorized as ‘practical’ while MABs are categorized as ‘theoretical’ because most of the MABs are still not commercialized and still in theory phase.



Volumetric energy density, which is the amount of energy that can be stored in a system, is often used to compare different energy storage. When compared to LIBs, MABs possess a much higher volumetric energy density (see Figure 1.1.1).³ However, most of the MAB still suffer from various problems. For example, sodium will react violently with water from the air. Thus, a lot of early-stage studies are still ongoing to design a safe and usable battery that can operate on less reactive components.⁴ Aluminum and magnesium-air batteries are much safer when compared to sodium-air batteries. But, these MABs have limited cell reversibility and the metal electrodes suffer from corrosion.^{5,6} The most researched MAB is lithium-air batteries since they possess the highest volumetric energy density among MABs, and their development is built on the knowledge that we already have from LIB technology. However, lithium-air batteries still need lithium, therefore their

use will only add to the problem of lithium shortage. Looking into the future, we are aware that a lot more work is needed to transfer these energizers from research labs to customers.

The only commercially available MAB right now is zinc-air batteries (ZAB). They are often incorporated into hearing aids and other smaller devices. These ZABs are primary cells, which means they are not rechargeable. They can often last up to 3 years if taken care of properly, which is a slightly lower shelf life than a typical primary LIB, which can last up to 5 years.⁷ This is because, after prolonged exposure to air, the electrolyte in ZAB will evaporate and eventually dry out, lowering its shelf life. Electrolyte evaporation is not the only issue that needs to be solved. Since ZABs operate using aqueous electrolytes, it becomes a priority to replace water-based liquids with a medium that can sustain temperatures falling below a freezing point of water. This is critical for ZABs to operate in all types of climates.

Why is it so important? The demand for flexible electronics that can function under harsh conditions, is increasing. For example, there is a demand for electrically heated gloves or other wearables for people living in countries with cold winters. These wearables can help blue-collar workers to continue their respective tasks safely and comfortably in a sub-zero environment. These flexible electronics are also easier to ship since they can be folded into different shapes to save more space. Besides that, there is a high demand for motion sensors, such as pulse sensors and epidermal sensors. These sensors are needed to aid doctors and physiotherapists in accurately detecting and analyzing the problems of their patients. So, these devices should be made from electronic materials that are responsive, deformable to fit the wearer, and yet operational within the user's range of motion. Therefore, this project is focused on electrochemical energy storage that can be designed

and fabricated to fit into the shape of wearable portable devices or even the wearer's clothing, rather than the stiff incompatible gear commonly presented in the past.

Altogether, our motivation is: (1) to explore flexible, stretchable, and leakage-free alkaline electrolytes for ZAB; (2) to create electrolytes that sustain all mechanical and electrochemical properties at sub-zero temperature; (3) to propose simplified synthetic pathways that exclude toxic reactants; and (4) ultimately to design and engineer electrolyte that can be integrated with other flexible components of ZABs.

1.2 Hydrogel

To tackle the problem of electrolytes evaporation in ZABs, while having a leakage-free flexible power source that operates in a broad range of temperatures, hydrogels have been an intriguing topic for this area of research. A hydrogel is a 3-dimensionally crosslinked hydrophilic polymer network that can hold a large amount of aqueous solution, very similar to a sponge. The hydrophilicity of the polymer network helps hold the absorbed solution for a prolonged duration, minimizing evaporation.

Depending on the type of monomer used to form the polymer network, these hydrogels often possess various properties, such as stretchability, self-healing, conductivity, and shape memory.⁸⁻¹⁰ Owing to their impressive stretchability and flexibility, hydrogel also plays an important role in a fully flexible solid-state battery design, meeting the increasing demand for flexible electronics mentioned earlier.¹¹

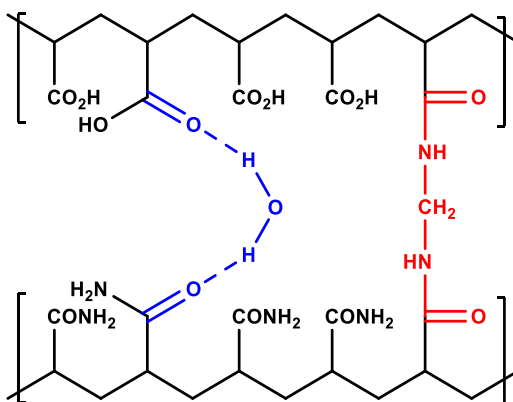
To stay relevant to the application for ZABs, only ionically conductive hydrogels will be discussed in this section. These hydrogels are generally synthesized from polymers containing hydroxyl or carbonyl functional groups, such as polyacrylamide, poly(vinyl-

alcohol), or polyacrylate salts.¹² These functional groups are responsible for holding large amounts of liquid through intermolecular interactions such as hydrogen bonds and dipole-dipole interactions.

1.3 Crosslinker

One of the main components in a conductive hydrogel is the crosslinker. Crosslinkers are responsible for connecting each polymer chain together, forming a network (see Figure 1.3.1). Hence, the amount of crosslinkers present in the polymer network plays a vital role in determining the flexibility and stretchability of hydrogels. As the density of crosslinkers increases in a hydrogel, the polymer chains are held together more tightly, making the hydrogel less stretchable and less flexible. Since the hydrogel is less flexible, the polymer chains cannot expand as much, hence affecting the liquid adsorption properties of the hydrogel.

Figure 1.3.1: Two main types of crosslinking in hydrogel, blue: physical crosslinking, and red: chemical crosslinking.

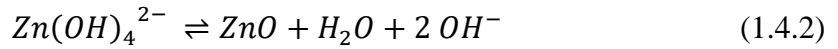
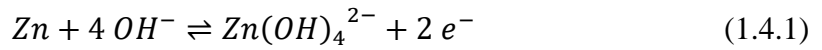


There are two main kinds of crosslinkers: physical crosslinkers and chemical crosslinkers.¹¹ Physical crosslinkers typically consist of weaker bonds or chemical

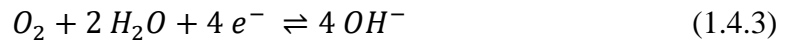
interactions such as hydrogen bonding and dipole-dipole interactions. These crosslinkers can be easily reformed once they are broken, giving hydrogel stretchability and flexibility. On the other hand, chemical crosslinkers are built on stronger chemical interactions such as covalent bonding. These crosslinkers cannot be reformed once broken. They are important as they hold all the polymer chains together to form a network, hence giving hydrogels their shape and enhancing their mechanical strength.

1.4 Electrolyte System for ZAB

To design a suitable hydrogel for ZAB, we need to start off by understanding the electrolyte system in ZAB. For a typical ZAB, the electrolyte used is potassium hydroxide (KOH) solution. At the metal electrode, Zn metal will react with hydroxide ions from the electrolyte to form zincate ions ($Zn(OH)_4^{2-}$), while releasing two electrons. When the concentration of zincate ions reaches a maximum, it promotes the formation and precipitation of zinc oxide.¹³



On the air electrode, oxygen reduction reaction occurs, consuming water and oxygen to produce hydroxide ions.



The overall reaction in a ZAB is as follows:



Since a large amount of OH^- ions are needed in the formation of zincate ions, the concentration of KOH solution used also plays a vital role in improving the conductivity

of ZABs. As the concentration of the KOH solution increases, the conductivity increases. However, if the concentration of KOH solution is too high, it will affect the solubility of zincate ions, promoting dendritic growth and shape change of the metal electrode.¹⁴ Hence, 6.0 M KOH solution is the usual concentration adopted in current ZABs.

The precipitation of zinc oxide often causes passivation at the metal electrode, which reduces the lifetime of ZABs. Furthermore, the precipitation of zinc oxide also decreases the concentration of zincate ions in the electrolyte solution. During the charging process, the reverse reaction of equation 1.4.1 cannot proceed due to the lack of zincate ions, hence affecting the rechargeability of ZAB.¹⁵

One common strategy to solve this problem is to introduce suitable additives into the electrolyte system to control the passivation process. For ZABs, zinc acetate is commonly used.¹⁶ This is because acetate ligands can coordinate more strongly with Zn^{2+} ions than hydroxide ligands.¹⁵ Hence, the addition of a small amount of zinc acetate (usually 0.2 M) can prevent the formation of zinc oxide when zincate ions are saturated.

1.5 Recent Work on Hydrogel Synthesis for ZAB

From section 1.4, we know that the composition of electrolytes for ZAB is usually 6.0 M KOH with 0.2 M zinc acetate as additives, which is extremely basic. The hydrogel synthesized should be chemically inert under this basic environment.

Starting off with simple polyacrylamide hydrogel, *Miao et al* were able to design an all-solid-state flexible ZAB.¹⁷ The hydrogel they used for the ZAB was polyacrylamide with N,N-methylenebisacrylamide (MBAA) as crosslinkers. They were able to load about

3.8 M KOH into the hydrogel and achieved ionic conductivity (σ) of 215.6 mS/cm. For comparison, the ionic conductivity of aqueous 6.0 M KOH solution is 626.6 mS/cm.¹⁸

Moving on, *Zhao et al* were able to synthesize a sodium polyacrylate (NaPA) hydrogel with MBAA as crosslinkers by neutralizing acrylic acid with sodium hydroxide.¹⁹ After soaking the hydrogel in 6 M KOH overnight, the hydrogel was able to absorb a large amount of KOH solution, reaching an ionic conductivity of 190 mS/cm.

To include new functionality to the hydrogel, *Chen et al* synthesized a hydrogel using two different monomers: polyacrylamide and polyacrylic acid with MBAA as crosslinkers.²⁰ The monomers were dissolved in a water-glycerol binary solution prior to polymerization. Since glycerol is normally used as an antifreeze agent, the addition of glycerol enabled the hydrogel to maintain stable ionic conductivity at a large temperature range (-20 °C to 70 °C). However, due to the presence of glycerol molecules impeding the movement of ions, the ionic conductivity was only 5 mS/cm.

Besides that, *Ma et al* were able to synthesize a dual-network hydrogel by incorporating cellulose polymer into the NaPA network.²¹ Since cellulose contains a lot of hydroxyl functional groups, the crosslinkers were mostly made up of physical crosslinks through hydrogen bonding. The hydrogel was stretchable, flexible, strong, and had a conductivity as high as 280 mS/cm. A list of other hydrogels designed for ZABs recently reported can be found in Table 1.5.1.

Table 1.5.1: Development of hydrogels for ZABs in the last four years and their reported ionic conductivity.

Year	σ (mS/cm)	Polymer Compositions
2022	78	A mixture of alkalized MXene and poly(vinyl-alcohol) ²²
2021	31	A mixture of carboxylated cellulose nanofibrils and poly(vinyl-alcohol) ²³
2021	82	A dual-polymer network of NaPA and starch crosslinked through MBAA ²⁴
2020	155	Co-crosslinked between poly(vinyl-alcohol), poly(acrylic acid), and graphene oxide ²⁵
2019	80	A mixture of bacterial cellulose and poly(vinyl-alcohol) ²⁶

1.6 Electrochemical Studies on Hydrogel

The electrochemical properties of the hydrogel are commonly reported in terms of ionic conductivity, with unit mS/cm. This is because ionic conductivity is the core property of electrolytes, and therefore, it is often used to compare the electrochemical performance of conductive hydrogels. Ionic conductivity is greatly dependent on the charge transport processes, such as the density of charge carriers, mobility of charge carriers, and ion diffusion. Although ionic conductivity is reported for the most promising alkaline hydrogel electrolytes, there is a lack of research on the mechanism of conduction, in particular on ion transport within a semi-liquid medium upon an applied electric field.

Until now, most of the research detailing charge transport processes is reported for polyethylene oxide (PEO)-based hydrogels, which are mostly used in a solid-state LIB design. These published works are focused on Li-ion mobilities.²⁷ PEO-based polymer electrolytes fall far behind current developments on alkaline hydrogels, not only with

regard to flexibility but also because they have significantly lower ionic conduction. With this in mind, we will apply electrochemical tools and models established for PEO-based systems to carry out analyses of the mass transport with respect to chemical composition, operating temperature, and polymer chain dynamics to our hydrogels.

1.7 Project Goals

Previous members in the research group had attempted to synthesize hydrogels with antifreeze properties through the addition of glycerol.²⁸ Similar to *Chen et al.*,²⁰ the monomer, polyacrylic acid, was dissolved in a water-glycerol binary solution prior to polymerization. The conductivity of the hydrogel was about 40 mS/cm. However, the hydrogel was not specifically designed for ZABs as the electrolyte incorporated was potassium chloride.

Building on the previous work, our project goal is to design a stretchable hydrogel specifically for ZAB with antifreeze properties. Inspired by both *Chen et al.*²⁰ and *Ma et al.*²¹, the polymer network chosen are polyacrylate and polyacrylamide. Cellulose will then be incorporated to improve the stretchability of the hydrogel, while glycerol will be added for the antifreeze property of the hydrogel.

As a new concept, we will combine different variants of cellulose into the same polymer network, mainly carboxymethyl cellulose and hydroxypropyl cellulose. These two derivatives are chosen because they are cheap and easily accessible. Until now, carboxymethyl cellulose and hydroxypropyl cellulose have been used as an additive in hydrogel electrolytes used in other batteries, but not in ZABs.^{29,30}

We are also proposing here a different method of incorporation of aqueous KOH solution into the polymer matrix. Most of the published work on synthetic procedures of similar hydrogels used a post-synthesis method via a soaking of polymer in KOH solution. This is time-consuming as the hydrogel normally needs to be dried overnight and then soak for another night until the electrolyte is fully absorbed. As such, we will attempt to add the electrolyte solution (6.0 M KOH and 0.2 M zinc acetate as additives) into the reaction mixture before polymerization.

The most important part of this proposed research relates to the electrochemical analyses of charge transport properties, mainly the density of charge carriers, mobility of charge carriers, and diffusion coefficient of the hydrogel. This will be carried out by electrochemical impedance spectroscopy (EIS) applied to theoretical models proposed by *Mellander et al.*³¹ This part of the project offers a new way of using electrochemical tools in quantifying important transport properties of electrolytes. Our hope is that we can provide new insight into ion dynamics taking place in this semi-liquid medium, contribute to a better understanding of the electrochemical properties of these materials, and ultimately aid in faster adaptation of these materials in real-world energy storage applications.

2 Theory

The electrochemical properties of the hydrogel throughout this project were determined using electrochemical impedance spectroscopy (EIS). However, basic definitions have to be recalled before we dive into the advanced analysis of impedance data.

2.1 Ohm's Law

Before defining impedance, a familiar equation to start with is Ohm's law:

$$R = \frac{V}{I} \quad (2.1.1)$$

where V is voltage, I is current, and R is resistance. For a direct current (DC) circuit, resistance is often used to describe the opposition of current in a circuit and it has a unit ohm (Ω). Another way of defining resistance based on equation (2.1.1) is the ratio of voltage to current. For a circuit with multiple elements connected in series or parallel, the term used to describe this ratio is then called impedance. So, equation (2.1.1) can be rewritten as:

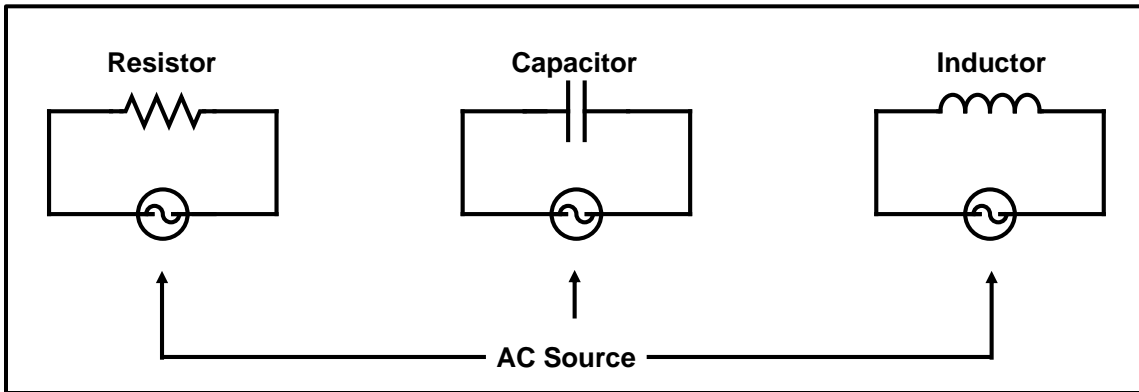
$$Z = \frac{V}{I} \quad (2.1.2)$$

where Z is impedance.

2.2 Voltage and Current in Alternating Current (AC) Circuits

In order to understand the impedance phenomenon, the behaviors of three circuit elements used to build EIS are considered. These three elements are a resistor, an inductor, or a capacitor element connected to an AC power source (see Figure 2.2.1)

Figure 2.2.1: Circuits with a resistor, capacitor, or an inductor connected to an AC power source.



When an AC power source is applied, the voltage across these three electrical elements is defined by:

$$V = V_0 \sin(\omega t) \quad (2.2.1)$$

Where ω is the angular frequency, t is time, and V_0 is the peak voltage. The term $\sin(\omega t)$ describes how the voltage is applied in a wave-like fashion. So, ωt represents the angle and has a unit of $^\circ$. Substituting equation (2.1.1), the equation for current across the resistor is:

$$I = \frac{V}{R} = \frac{V_0}{R} \sin(\omega t) \quad (2.2.2)$$

The expression of current across an inductor when an AC power source is applied is given by:

$$V = L \frac{dI}{dt}$$

$$dI = \frac{V}{L} dt$$

Where L represents inductance. Substituting equation (2.2.1) will give us:

$$dI = \frac{V_0}{L} \sin(\omega t) dt$$

When both sides of the equation are integrated, it will leave us with:

$$\int dI = \int \frac{V_0}{L} \sin(\omega t) dt$$

$$I = \frac{V_0}{\omega L} [-\cos(\omega t)]$$

Through trigonometry identities, the cosine term can be converted to a sine term, giving us:

$$I = \frac{V_0}{\omega L} \sin(\omega t - \frac{\pi}{2}) \quad (2.2.3)$$

For the capacitor, the expression of current across it will be:

$$I = C \frac{dV}{dt}$$

Where C represents capacitance. Once again, equation 2.2.1 can be substituted to give us:

$$I = C \frac{d}{dt} (V_0 \sin(\omega t))$$

A simple derivation of the equation will leave us with:

$$I = V_0 \omega C \cos(\omega t)$$

Once again, using trigonometry identities, the cosine term can be converted to:

$$I = V_0 \omega C \sin(\omega t + \frac{\pi}{2}) \quad (2.2.4)$$

Now that the equations for voltage and current for these three circuits are established, finding out the expression for impedance should be fairly easy since impedance, as defined in section 2.1, is the ratio of voltage to current. However, for real-world electronic applications where complex circuitry with multiple elements are involved, calculations for impedance are complicated since there will be a lot of sine terms. Hence, the voltage and current are normally written in complex exponential form to simplify these calculations.

In complex exponential form, the voltage is given by:

$$V = V_0 e^{j\omega t} \quad (2.2.5)$$

Where j is an imaginary number and j^2 is -1 . The imaginary number is denoted as j instead of the usual i in this thesis to avoid confusion with current, I . Using the same expressions above, the current can once again be defined as:

$$I = \frac{V_0}{R} e^{j\omega t} \quad (2.2.6)$$

$$I = \frac{V_0 e^{j\omega t}}{j\omega L} \quad (2.2.7)$$

$$I = j\omega C (V_0 e^{j\omega t}) \quad (2.2.8)$$

Where equations 2.2.6, 2.2.7, and 2.2.8 are the current expressions for a resistor, an inductor, and a capacitor connected to an AC power source respectively.

Starting off with the resistor, the ratio of voltage to current according to equations 2.2.5 and 2.2.6 will be:

$$Z = \frac{V}{I} = R \quad (2.2.9)$$

Since the only element in that circuit is only a resistor, it makes sense that the total impedance for that circuit is the resistance of that resistor. Moving on. from equations 2.2.5 and 2.2.7, the ratio of voltage to current for that inductor will be:

$$\chi_L = \frac{V}{I} = j\omega L \quad (2.2.10)$$

Where χ_L is called inductive reactance.

Last but not least, the ratio of voltage to current expression for a capacitor based on equations 2.2.5 and 2.2.8 will be:

$$\chi_C = \frac{V}{I} = \frac{1}{j\omega C} = -\frac{j}{\omega C} \quad (2.2.11)$$

Where χ_C is called inductive reactance. Just like resistance or impedance, χ_L and χ_C share the unit, Ohms.

2.3 Current Lag and Lead in Inductor and Capacitor

In section 2.2, the impedance equations for purely resistive, inductive, and capacitive circuits were established. It might be hard to imagine the relationship between the voltage and current of these elements just by knowing the equations. So, in this section, sinusoidal graphs are plotted to further understand their relationships.

Figure 2.3.1: Sinusoidal graph for voltage and current across a resistor when AC power source is applied. The x-axis (ωt) represents the angle while the y-axis represents the absolute value of voltage and current. The maximum and minimum (amplitude of wave) are different so that the graphs are not overlapped and the difference in value should be ignored.

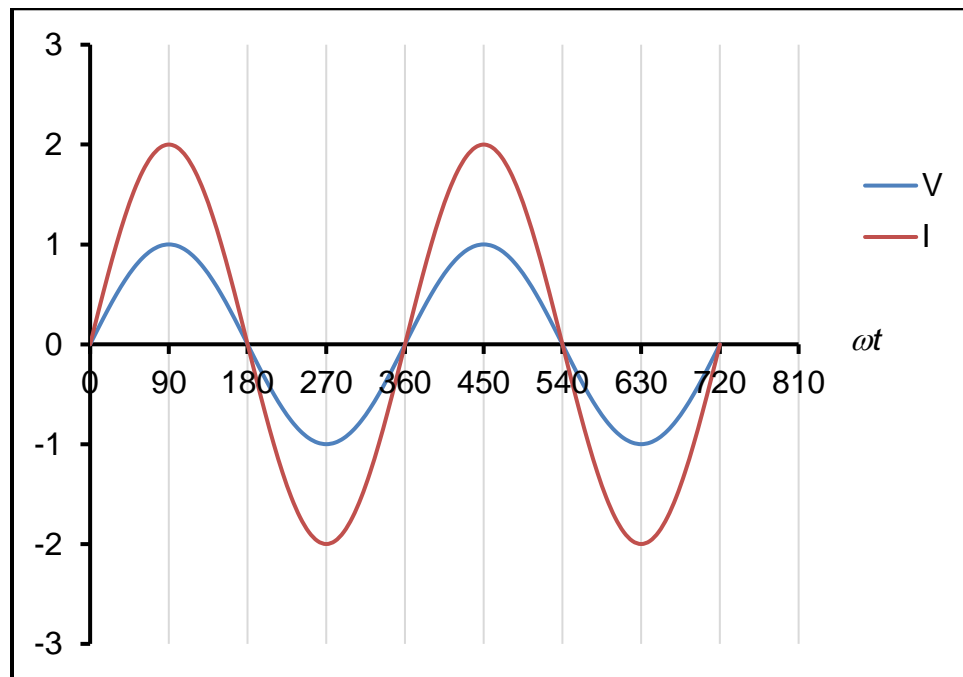
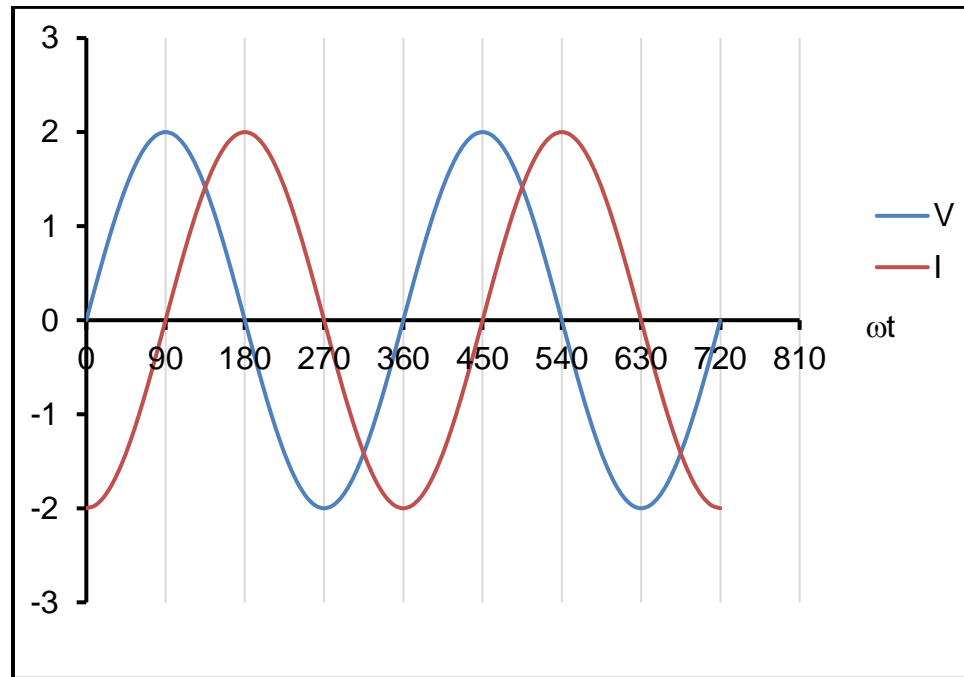


Figure 2.3.1 shows a graph of the voltage and current across a resistor when it is connected to an AC power source. From that figure, the voltage and current reach a

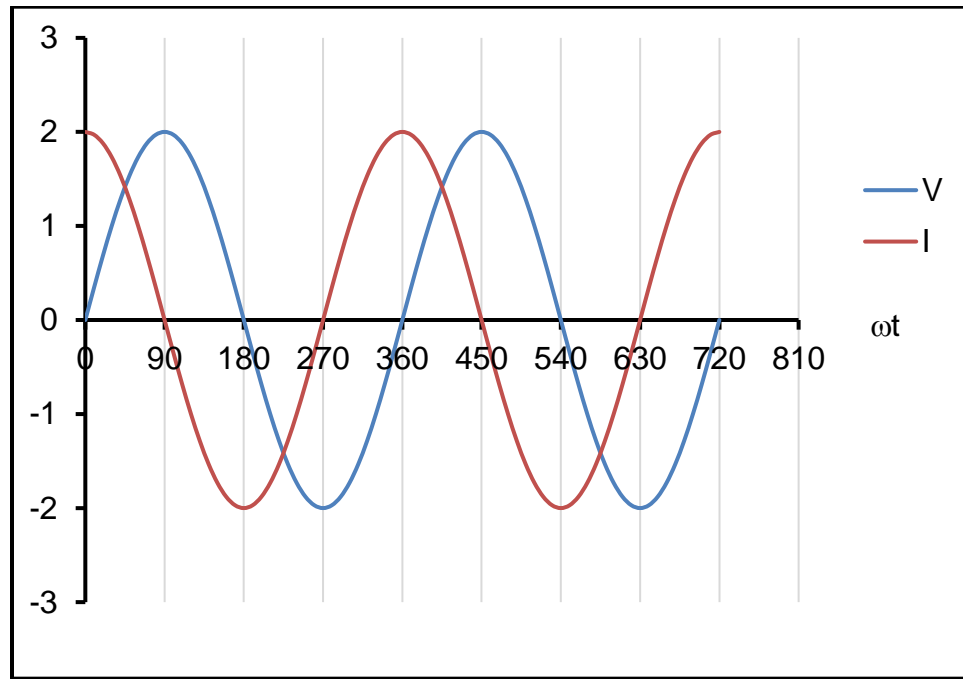
maximum (at 90° and 450°) and decrease to a minimum (at 270° and 630°) at the same angle. Hence, they are considered ‘in phase’.

Figure 2.3.2: Sinusoidal wave for an inductor connected to an AC power source. The x-axis (ωt) represents the angle while the y-axis represents the absolute value of voltage and current.



Moving on to an inductor in an AC circuit, a similar sinusoidal graph can again be plotted based on equations 2.2.1 and 2.2.3 (see Figure 2.3.2). By comparing these two equations, we can see that the voltage is always 90° ahead of the current. As such, the current maxima and minima appear 90° later than the voltage. Hence, the voltage and current in a purely inductive AC circuit are considered ‘out of phase’ by 90° ($\pi/2$). In this case, the current is lagging behind the voltage. This is because when voltage is applied to an inductor (a coil of wire), it will resist the change in current. Hence, the current builds up slower than the voltage.

Figure 2.3.3: Sinusoidal wave for a capacitor connected to an alternating current. The x-axis (ωt) represents the angle while the y-axis represents the absolute value of voltage and current.



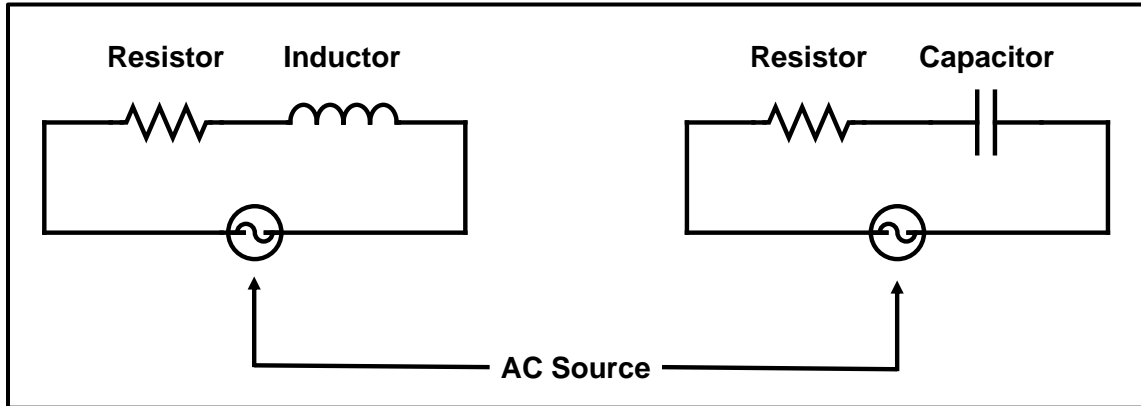
Finally, for a purely capacitive AC circuit, the sinusoidal graph based on equations 2.2.1 and 2.2.4 is represented in Figure 2.3.3. Similar to a purely inductive circuit, both the current and voltage are again ‘out of phase’, except that the current peaks are 90° ahead of the voltage peaks instead. In this case, the current is leading the voltage. This is because the current needs to lead the voltage to conduct charge to the capacitor plates to raise its voltage.

2.4 Inductive and Capacitive Reactance

The circuits that have been discussed in sections 2.2 and 2.3 are purely resistive, inductive, or capacitive. What about circuits with two different elements? In this section, resistive-inductive (RL) and resistive-capacitive (RC) circuits will be discussed (see Figure 2.4.1). These two circuits are chosen specifically to introduce the concepts needed to

understand a Nyquist plot, which is a common method used to analyze EIS data. Further discussion on Nyquist plot will be done in a later section of this chapter.

Figure 2.4.1: Diagram of RL circuit (left) and RC circuit (right)

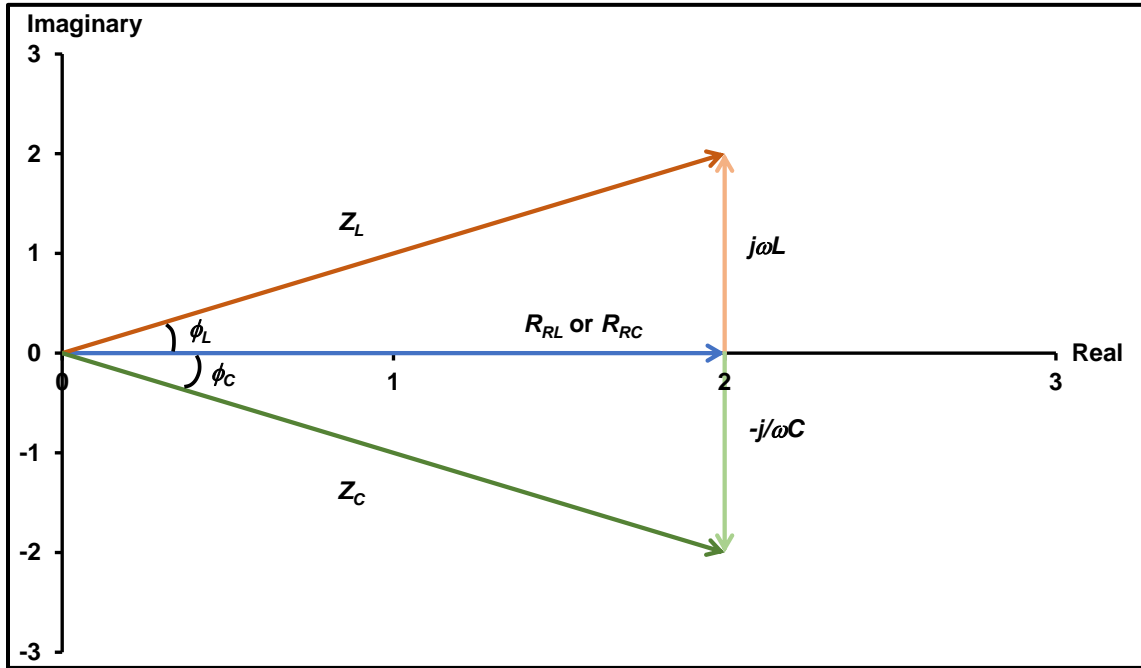


We have established that the voltage and current across these elements behave in a wave-like fashion. Hence, the resistance and reactance across them (from equations 2.2.9 to 2.2.11) can be depicted as vectors on a complex plane, which contain a magnitude component and a direction component.

In Figure 2.4.2, a vector arrow can be illustrated along the x-axis of the complex plane to represent resistance (R_{RL} or R_{RC} , blue arrow). From equations 2.2.10 and 2.2.11, the expressions for these two reactances contain the imaginary numbers j and $-j$, respectively. In mathematical terms, multiplying these vectors by j will rotate them by 90° on the complex plane (counterclockwise for $+j$ and clockwise for $-j$). This is consistent with the current leading and lagging phenomena for a purely inductive and capacitive discussed above. Therefore, the vector arrows representing both inductive and capacitive reactances are perpendicular to the real axis of the complex plane. The inductive reactance vector is

directed towards the positive quadrant (light orange arrow) while a vector represents the capacitive reactance towards the negative quadrant (light green arrow).

Figure 2.4.2: Vector arrows of resistance and reactance drawn on a complex plane to find out the total impedance for RL and RC circuits.



The total impedance of RL circuit (Z_L , orange arrow) and RC circuits (Z_C , green arrow) is the sum of these two vectors, giving us:

$$Z_L = |Z_L|e^{j\phi_L} \quad (2.4.1)$$

$$Z_C = |Z_C|e^{j\phi_C} \quad (2.4.2)$$

Where $|Z_L|$ and $|Z_C|$ are the magnitude of the impedance, while ϕ_L and ϕ_C are the angles from the real axis. These values can be calculated using simple trigonometry, where

$$|Z_L| = \sqrt{(R_{RL})^2 + (\omega L)^2}, \phi_L = \tan^{-1} \frac{\omega L}{R_{RL}}$$

$$|Z_C| = \sqrt{(R_{RC})^2 + \left(-\frac{j}{\omega C}\right)^2}, \phi_C = \tan^{-1} \frac{-1}{\omega C R_{RC}}$$

Aided by Euler's relationship, complex exponential numbers can be expressed as complex cartesian numbers. Hence, impedance, Z , can be written as:

$$Z = Z' + jZ''$$

Where both Z' and Z'' are the real part and the imaginary part of the impedance. For RL and RC circuits, equations (2.5.1) and (2.5.2) can be rewritten as:

$$Z_L = Z_L' + jZ_L'' = R_{RL} + j\omega L \quad (2.4.3)$$

$$Z_C = Z_C' + jZ_C'' = R_{RC} + \left(-\frac{j}{\omega C}\right) \quad (2.4.4)$$

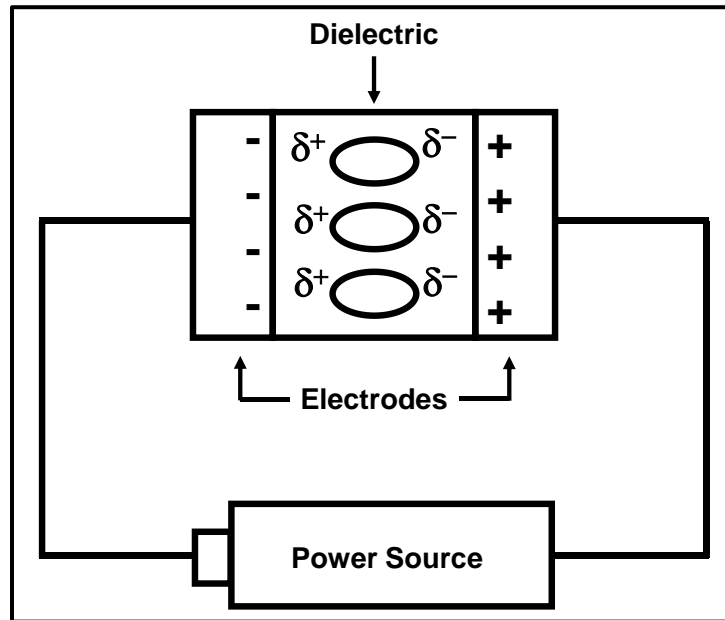
2.5 Nyquist Plot

Based on equations (2.4.3) and (2.4.4), the electrochemical phenomena occurring in materials including their surface and bulk electrochemical activities can be analyzed by plotting a complex plane diagram of Z'' against Z' . This spectrum is often called Nyquist plot. When AC voltage in a range of frequencies is applied to a material, the total impedance at each frequency can be projected on a Nyquist plot. The real part of the impedance (horizontal axis) describes the resistive behavior of a material while the imaginary part of the impedance (vertical axis) shows the reactive behavior of a material. If the spectrum appears at the $+Z''$ quadrant, inductive reactance can be determined and hence finding out the inductance of a material. The same logic can be applied to calculate the capacitance of material if the data is recorded at the $-Z''$ quadrant.

2.6 Nyquist Plot of an Electrolyte Material

From sections 2.1 to 2.5, we have discussed the general concept of impedance spectroscopy. To continue the discussion regarding the impedance of an electrolyte material, an understanding of a capacitor is required. A capacitor usually consists of two conducting electrodes being separated by an insulator, which is called a dielectric (see Figure 2.6.1).

Figure 2.6.1: A typical circuit of a capacitor connected to a power source. The ovals between the two electrodes represent molecules of the dielectric being polarized.



When the two electrodes are connected to a power source, charges will build up on either side of the electrodes (negatively charged on the left electrode while positively charged on the right electrode in Figure 2.6.1). This will create an electric field. The molecules in the dielectric will then be polarized, forming their own electric field of the opposite direction, hence resisting the applied electric field. This resistance is often known as permittivity. It is important to note that not all insulators can be dielectric, but all

dielectrics are insulators. The ability to be polarized when placed in an electric field is crucial to be considered a dielectric.

The permittivity of free space, also known as vacuum permittivity, which is often denoted as ϵ_0 , has a value of $8.854 \times 10^{-14} \text{ Fcm}^{-1}$. Dielectric constant, ϵ_r , is the ratio between the absolute permittivity of a material and permittivity of vacuum, giving us the equation:

$$\epsilon_r = \frac{\epsilon}{\epsilon_0} \quad (2.6.1)$$

Next, let's imagine that the power source in Figure 2.6.1 is removed. The negative charges built up on the electrode will stay on the electrode until the circuit is closed again. If a device is connected, the negative charges will move through the device and reach the positively charged electrode, hence powering the device. Once both electrodes reach an equilibrium in terms of charges (neutral), the capacitor will no longer be able to power a device until it is charged again.

Capacitance, C , is often used to describe the amount of energy stored in the form of charges in a capacitor. It depends on the area of the two electrodes (A), the distance between the two electrodes (d), and the absolute permittivity of the dielectric (ϵ), giving us:

$$C = \frac{\epsilon A}{d} = \frac{\epsilon_r \epsilon_0 A}{d} \quad (2.6.2)$$

What will happen if the dielectric in Figure 2.6.1 is replaced with an electrolyte? When an electrolytic material is connected to a power source, charges once again will build up on either side of the electrodes. Since electrolyte contains freely moving ions, the positive ions will move towards the negatively charged electrode while the negative ions migrate towards the positively charged electrode (see Figure 2.6.2). This will create an

electrical double layer (EDL), also commonly known as Helmholtz double layer. The capacitance of EDL is given by:

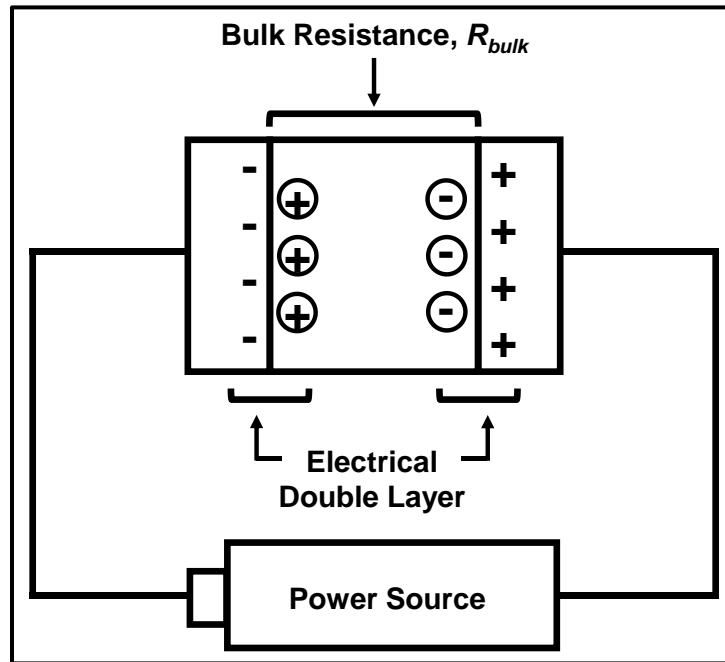
$$C_e = \frac{\epsilon_r \epsilon_0 A}{\lambda} \quad (2.6.3)$$

Where C_e is the capacitance of EDL and λ is Debye length. The resistance across the material, also known as bulk resistance, can be calculated as:

$$R_{bulk} = \frac{d}{\sigma A} \quad (2.6.4)$$

Where σ is the ionic conductivity of the electrolyte.

Figure 2.6.2: Schematic diagram of an electrolytic material connected to a power source, creating an electrical double layer (EDL).



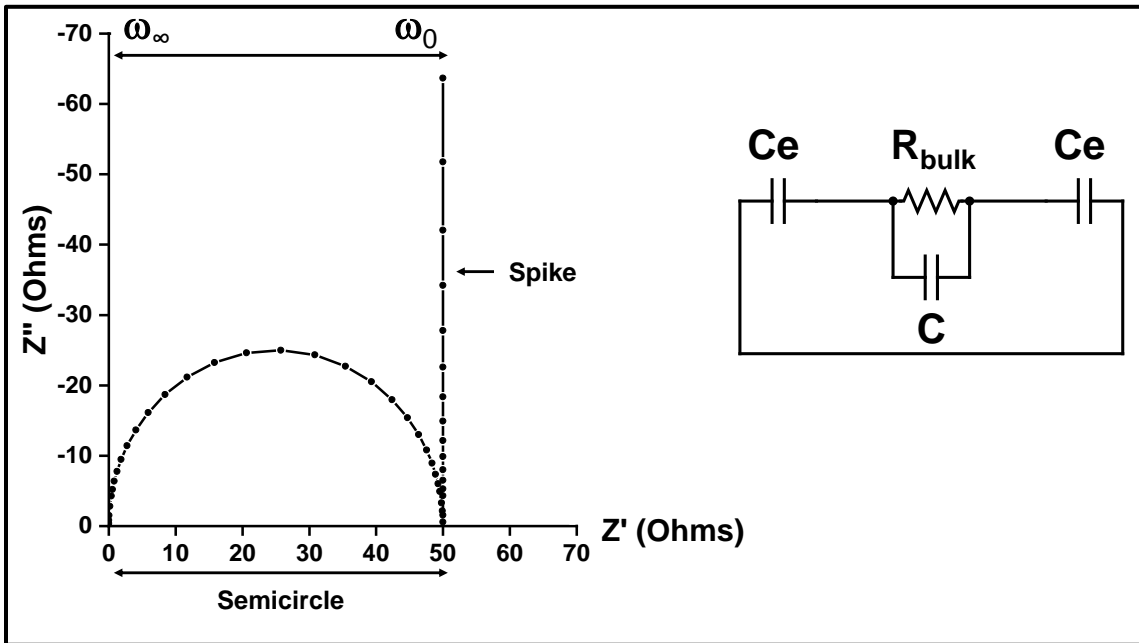
When the impedance of the above circuit is recorded over a range of frequencies, it will appear as a semicircle and a spike in the Nyquist plot (see Figure 2.6.3, left). This specific shape can be represented by an equivalent circuit of a parallel combination of a resistor and a capacitor that are connected in series with two capacitors (see Figure 2.6.3,

right). Thus, the real and imaginary part of the impedance of the equivalent circuit can be represented by:

$$Z' = \frac{R}{1+(\omega R_{bulk}C)^2} \quad (2.6.5)$$

$$Z'' = -(\omega R_{bulk}CZ' + \frac{2}{\omega C_e}) \quad (2.6.6)$$

Figure 2.6.3: Nyquist plot with a semicircle and a spike (left) and an equivalent circuit to represent the shape of the Nyquist plot (right). The arrow on top of the spectra shows the angular frequency of the AC voltage, where ω_∞ and ω_0 represent the angular frequency approaching infinity and zero respectively. The numbers on the axis are just an example and they should not be treated as actual values.



2.7 Relationship between Time Expression and Loss Tangent

When AC voltage is applied to a dielectric, there often will be dissipation of electrical potential energy in the form of heat. This dissipation factor is commonly known as loss tangent, and it can be calculated through:

$$\tan(\phi) = \frac{Z'}{Z''} \quad (2.7.1)$$

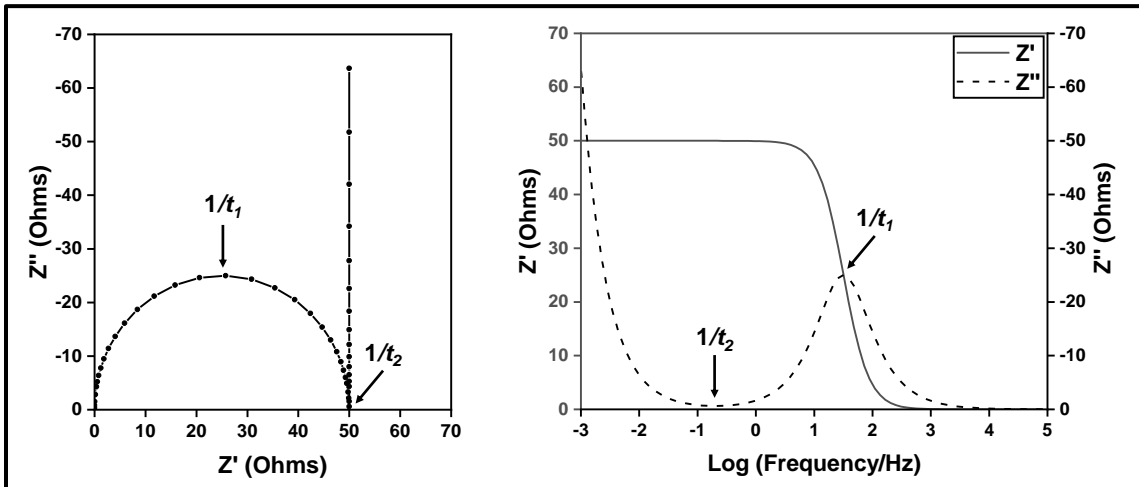
Where ϕ in this case, is similar to ϕ_L and ϕ_C , represents the angle from the real axis of the impedance spectra. According to Bandara and Mellandar,³¹ the peak of this dissipation factor of a Nyquist plot with a semicircle and a spike is related to:

$$\tan(\phi)_{max} = \frac{\sqrt{\delta}}{2}, \sqrt{\delta} = \frac{t_2}{t_1} \quad (2.7.2)$$

Where t_1 and t_2 are the time constant when Z'' is at its maximum and minimum respectively.

To find t_1 and t_2 , we can start by looking at the frequency corresponds to Z'' when it is at its maximum and minimum (see Figure 2.7.1).

Figure 2.7.1: Same Nyquist plot with a semicircle and a spike as Figure 2.6.3 (left). The real and imaginary part of impedance from a Nyquist plot with a semicircle and a spike plotted against frequency (right). Arrows show the angular frequency when Z'' is at its maximum and minimum. Recall that the negative signs of the imaginary part of the impedance, Z'' , only denotes the capacitive behavior (capacitive reactance) of the material and should be left out when comparing the values.



From Figure 2.7.1, we can see that the frequency when Z'' is at its maximum is at the halfway point of the semicircle of the Nyquist plot. Hence, we can substitute the expression ($Z' = Z'' = R/2$) into equation (2.6.5) and (2.6.6), giving us:

$$\omega_1 = \frac{2\pi}{t_1} = \frac{2\pi}{R_{bulk}C} \quad (2.7.3)$$

Where ω_1 is the angular frequency when Z'' reaches its maximum value. On the other hand, the frequency when Z'' is at its minimum is at the real axis intersection of the semicircle. Hence, we can substitute the expression ($Z' = R_{bulk}$, $Z'' = 0$) into equation (2.6.5) and (2.6.6), giving:

$$\omega_2 = \frac{2\pi}{t_2} = \frac{2\pi}{R_{bulk}C} \sqrt{\frac{2C}{Ce}} \quad (2.7.4)$$

Where ω_2 is the angular frequency when Z'' values reach a minimum. These frequency expressions are under the assumption that capacitance, C , is very small when compared to the capacitance of the electrical double layer, Ce , as the Debye length, λ is much smaller than the thickness of the electrolyte material, d .

2.8 Calculation of Charge Transport Properties

According to Bandara and Mellandar,³¹ the diffusion coefficient of an ionic conductor can be calculated if the values of t_2 and δ are known. The equation for the diffusion coefficient, D , is given by:

$$D = \frac{d^2}{t_2 \delta^2} \quad (2.8.1)$$

The average mobility of ions, μ , can then be calculated from diffusion coefficient through the Nernst-Einstein relation, giving us:

$$\mu = \frac{eD}{k_bT} = \frac{e}{k_bT} \left(\frac{d^2}{t_2\delta^2} \right) \quad (2.8.2)$$

Where k_B is Boltzmann constant and has the value of $1.38 \times 10^{-23} \text{ JK}^{-1}$, e is electron charge and has the value $1.60 \times 10^{-19} \text{ Coulomb}$, and T is temperature in Kelvin. Finally, the density of charge carrier, n , can be calculated by relating the mean mobility of ions and conductivity of the electrolyte material, where:

$$n = \frac{\sigma}{e\mu} = \frac{\sigma k_B T t_2 \delta^2}{e^2 d^2} \quad (2.8.3)$$

Recall that the conductivity of the electrolyte material, σ , is the inverse of the bulk resistance, R_{bulk} , of the electrolyte material, and can be calculated from equation (2.6.4).

In short, to find out the charge transport properties of an electrolyte material, EIS can be used. The Nyquist plot of the electrolyte material over a range of frequencies will be recorded. The Z' and Z'' values will then be extrapolated from the Nyquist plot. Values for $\tan(\phi)$ can simply be calculated from equation (2.7.1) and then a graph of $\tan(\phi)$ against frequency can be plotted. The frequency when $\tan(\phi)$ is at its maximum, will be used to find t_2 , while the value for δ can be calculated from equation (2.7.2). After solving the values for t_2 and δ , equation (2.8.1), (2.8.2), and (2.8.3) is used to determine the charge transport properties of the electrolyte, while the conductivity of the electrolyte material can simply be calculated from equation (2.6.4).

3 Experimental

3.1 Chemical Reagents Used in Synthesis

Acrylamide (99%), acrylic acid (99%) with 200 ppm 4-methoxyphenol as inhibitor, ammonium persulfate (APS, 98%), N,N'-methylenebisacrylamide (MBAA, 99%), N,N,N',N'-tetramethylethyldiamine (TMEDA, 99%), cellulose, hydroxypropyl cellulose (HPC), sodium carboxymethyl cellulose salt (CMC), and potassium persulfate (KPS, 99%) were purchased from Sigma Aldrich and used without further purification. Zinc acetate dihydrate (98%) and glycerol (99.5%) were purchased from Fischer Scientific and used without further purification. Potassium hydroxide (KOH) pellets were purchased from EMD Millipore Corporation respectively and used without further purification.

3.2 General Considerations

All hydrogels were formed in square molds purchased from a general dollar store (Dollarama). To have a consistent thickness for mechanical and electrochemical tests, the solution mixture was maintained to approximate 35.0 mL. Hence, all hydrogel formed has an approximate dimension of 8.2 cm × 8.2 cm × 0.35 cm.

13.0 M potassium hydroxide and 1.5 M zinc acetate stock solutions were prepared and diluted with distilled water to the molarity mentioned below during the synthesis of all hydrogels. In order to simplify the discussion of the hydrogels synthesized in the next few sections, the hydrogels are abbreviated and summarized as follows:

Table 3.2.1: List of hydrogels synthesized, the chemical compositions, and their respective label for ease of discussion. Capital ‘B’ and ‘Z’ in the label stands for base and zinc acetate respectively. The subscript followed represents the concentrations. (a) An AM gel refers to hydrogel made from acrylamide and potassium acrylate monomer with MBAA as a crosslinker. (b) An acrylate-only gel refers to hydrogel made from potassium acrylate monomer only with MBAA as crosslinkers.

Sample	Name / label	Chemical composition
1	B _{0.0} Z _{0.0}	AM gel ^(a)
2	B _{0.0} Z _{0.2}	AM gel with 0.2 M Zn(Ac) ₂
3	B _{3.0} Z _{0.0}	AM gel with 3.0 M KOH
4	B _{1.5} Z _{0.2}	AM gel with 0.2 M Zn(Ac) ₂ and 1.5 M KOH
5	B _{3.0} Z _{0.2}	AM gel with 0.2 M Zn(Ac) ₂ and 3.0 M KOH
6	B _{4.5} Z _{0.2}	AM gel with 0.2 M Zn(Ac) ₂ and 4.5 M KOH
7	B _{6.0} Z _{0.2}	AM gel with 0.2 M Zn(Ac) ₂ and 6.0 M KOH
8	B _{3.0} Z _{0.2} -Cell	AM gel with 0.2 M Zn(Ac) ₂ , 3.0 M KOH, and cellulose
9	B _{3.0} Z _{0.2} -CMC	AM gel with 0.2 M Zn(Ac) ₂ , 3.0 M KOH, and CMC
10	B _{3.0} Z _{0.2} -HPC	AM gel with 0.2 M Zn(Ac) ₂ , 3.0 M KOH, and HPC
11	KPA	Acrylate-only gel ^(b)
12	KPA-Gly	Acrylate-only gel with glycerol

3.3 Synthesis of Hydrogels

Synthesis of potassium poly(acrylate-co-acrylamide) based hydrogels

To synthesize B_{0.0}Z_{0.0}, acrylamide (5.01 g, 70.3 mmol), MBAA (0.0168 g, 0.109 mmol) and APS (0.102 g, 0.438 mmol) were added into a beaker containing 7.5 mL of distilled water. The solution mixture was left to stir for 10 minutes until all solids were dissolved. Then, the clear and colorless liquid was transferred into a 20 mL measuring cylinder and the solution was top up to 17.5 mL with distilled water. Next, the 17.5 mL

solution mixture was transferred back to the beaker and acrylic acid (0.476 mL, 6.94 mmol) was added with vigorous stirring. Then, 17.0 mL of KOH solution (0.408 M) was added slowly over the span of 5 minutes. After the addition of KOH, the solution was left to stir for another 5 minutes to make sure all the acids are fully neutralized. Then, TMEDA (13.4 μ L, 0.0896 mmol) was added and the solution mixture was immediately poured into a mold. Finally, free-radical polymerization was initiated in a UV reactor for 120 minutes.

To introduce 0.2 M zinc acetate into the hydrogel, the weighed-out solids were added to a beaker of 7.5 mL zinc acetate solution (0.933 M) instead of distilled water. The rest of the procedure remained the same. Different molarity of KOH was used instead to increase the concentration of KOH in the hydrogel. For hydrogels with 1.5 M, 3.0 M, 4.5 M, and 6.0 M of KOH, the concentration of 17.0 mL KOH used are 3.495 M, 6.584 M, 9.672 M, and 12.761 M.

Synthesis of cellulose hydrogels

For the synthesis of B_{3.0}Z_{0.2}-Cell, acrylamide (5.01 g, 70.3 mmol), MBAA (16.8 mg, 0.109 mmol), and APS (0.100 g, 0.438 mmol) were added to a beaker containing 7.5 mL of zinc acetate solution (0.933 M). The solution mixture was left to stir for 10 minutes until all solids were dissolved. Then, the clear and colorless liquid was transferred into a 20 mL measuring cylinder and the solution was top up to 17.5 mL with distilled water. Next, the 17.5 mL solution mixture was transferred back to the beaker and acrylic acid (0.476 mL, 6.94 mmol) was added. The solution mixture was left stirring from this point onwards until all other reactants were added. After stirring for 2 minutes, cellulose (0.275 g, 5% weight of polymer) was added. The cloudy white solution was left to stir until homogeneous before adding 6.584 M of KOH solution (17.0 mL) slowly over the span of

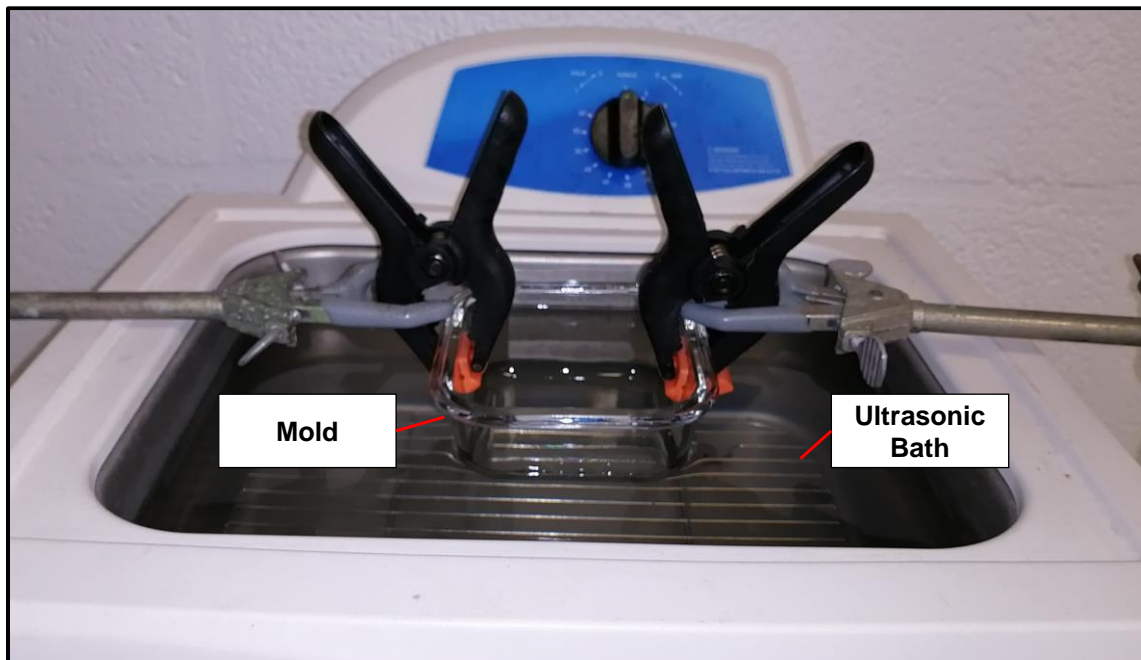
5 minutes. Then, TMEDA (13.4 μL , 0.0896 mmol) was added and the solution mixture was immediately poured into a mold. Finally, free-radical polymerization was initiated in a UV machine for 50 minutes.

For the synthesis of $\text{B}_{3.0}\text{Z}_{0.2}\text{-CMC}$ and $\text{B}_{3.0}\text{Z}_{0.2}\text{-HPC}$, the cellulose was replaced with the same weight percentage of CMC or HPC instead. The general observations during the synthesis were the same except after the addition of the different cellulose. For CMC, the solution remained clear and colorless after the addition, but the viscosity of the solution mixture increases. After the addition of HPC, white solid chunks were observed floating around the solution mixture instead.

Synthesis of KPA

MBAA (0.0336 g, 0.218 mmol) was added to a beaker containing 3.070 mL of water. The mixture was stirred until clear and colorless. Then, 4.667 mL of zinc acetate solution (1.5 M) was added, followed by 22.025 mL of potassium hydroxide solution (13.0 M). The clear and colorless solution turned cloudy but eventually turned back to clear and colorless again during the addition of potassium hydroxide solution. Next, the beaker was transferred to a cold-water bath and acrylic acid (5.238 mL, 76.3 mmol) was added dropwise in the span of 5 minutes. After neutralizing acrylic acid, the solution mixture was poured into a mold that was initially set up on an ultrasonic bath (see Figure 3.3.1) and potassium persulfate (0.1000 g, 0.370 mmol) was added to the mold. The solution mixture was left in that sonication bath for 30 minutes to initiate polymerization.

Figure 3.3.1: Photo of a mold used to form hydrogels with a specific shape in an ultrasonic bath



Synthesis of KPA-Gly

MBAA (0.0945 g, 0.613 mmol) and glycerol (0.4410 g, 4.78 mmol) were added to a beaker containing 2.720 mL of water. The mixture was stirred until clear and colorless. Then, 4.667 mL of zinc acetate solution (1.5 M) was added, followed by 22.025 mL of potassium hydroxide solution (13.0 M). The clear and colorless solution turned cloudy but eventually turned back to clear and colorless again during the addition of potassium hydroxide solution. Next, the beaker was transferred to a cold-water bath and acrylic acid (5.238 mL, 76.3 mmol) was added dropwise in the span of 5 minutes. After neutralizing acrylic acid, the clear and colorless solution mixture was poured into a mold that was initially set up on a sonication bath, and potassium persulfate (0.1000 g, 0.370 mmol) was added to the mold. The solution mixture was left in the sonication bath for 30 minutes to initiate polymerization.

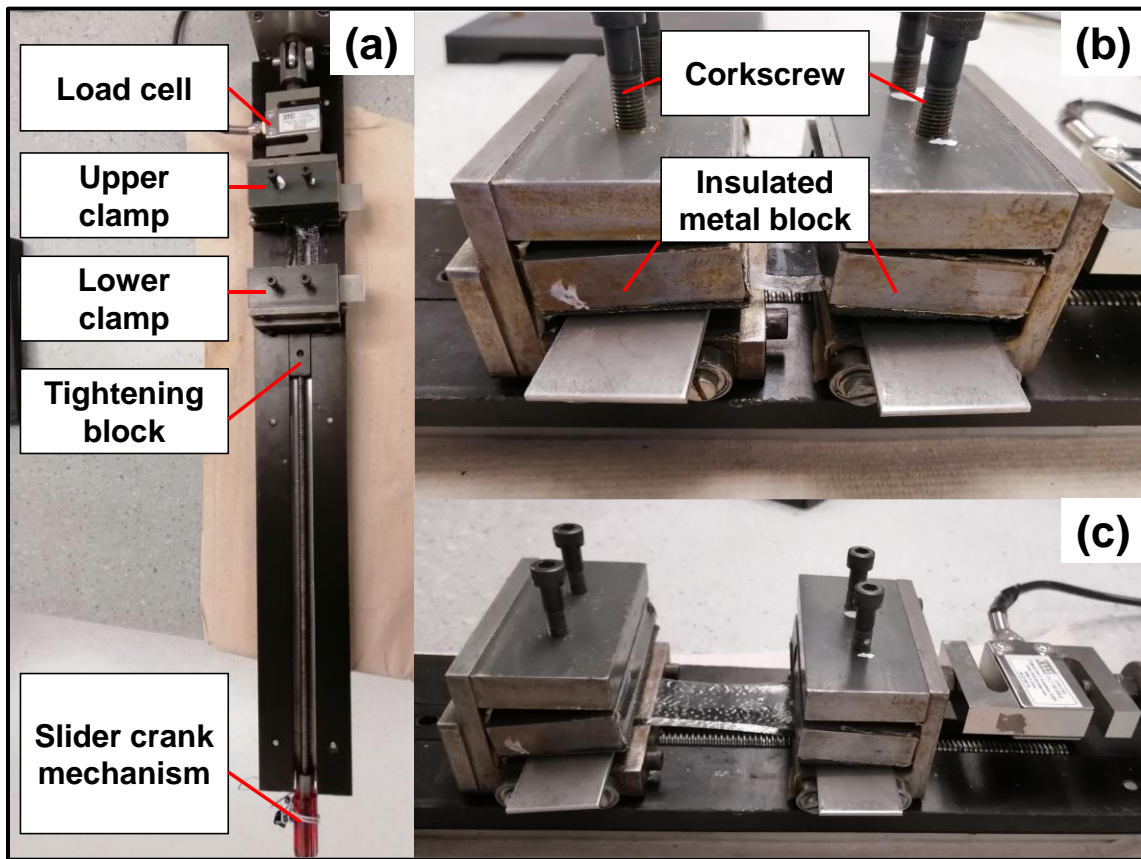
Synthesis of *Chen et al's* hydrogel

Acrylamide (4.997 g, 70.3 mmol), APS (0.0073 g, 0.0320 mmol), and MBAA (0.0043 g, 0.0279 mmol) was added to a beaker containing 4 mL of distilled water. The mixture was left to stir for ten minutes until all solids were dissolved. Then, AA (0.476 mL, 6.93 mmol) was added to the clear and colorless solution. The solution mixture was transferred to a fresh beaker containing glycerol (4.017 g, 43.6 mmol) and was left to stir for another 5 minutes until the solution became homogeneous. Next, TMEDA (7.43 μ L, 49.5 μ mol) was added and the solution mixture was immediately transferred to a mold. Finally, free-radical polymerization was initiated in a UV machine for 120 minutes, yielding a clear and colorless hydrogel.

3.4 Analysis of Hydrogels

Mechanical tests were performed using the equipment shown in Figure 3.4.1(a). The equipment consists of a calibrated 30 kg Load Cell, an upper and a lower clamp, a tightening block, and a slider-crank mechanism. One end of the calibrated 30 kg Load Cell was fitted to a semi-free moving point, while the other end was fitted onto the upper clamp. This allows a free-moving horizontal axis for the upper clamp. The lower clamp was connected to the slider-crank mechanism.

Figure 3.4.1: Images of equipment used for mechanical and tensile experiments; (a) a full image of the machine, (b) when the hydrogel is clamped, (c) when the hydrogel is being elongated.



During a mechanical experiment, the lower clamp will first be adjusted through the slider-crank mechanism to have a gap of 2 cm between the upper clamp and lower clamp. Then, the gel will be placed in between the two clamps and secured with two pieces of insulated metal blocks (see Figure 3.4.1(b)). The corkscrew will be tightened with light torque so that it will only firmly hold the hydrogel in place during the experiment but not too much to break the hydrogel. Next, the lower clamp was pulled downwards by rotating the slider-crank mechanism until the hydrogel breaks (see Figure 3.4.1(c)). The elongation of the hydrogel was calculated as:

$$\text{Elongation} = \frac{\text{Final length before breaking}}{\text{Initial length}} \times 100\%$$

Fourier Transform Infrared Spectroscopy (FTIR)

ATR-FTIR was performed on Bruker's Alpha II compact FTIR spectrometer with an accompanying ATR-FTIR attachment. A blank spectrum of the air was recorded before recording any FTIR of the samples. A 2 cm × 2 cm sample of hydrogel was cut out and dried in open air for a week before they were grounded into powder for FTIR analysis.

Electrochemistry

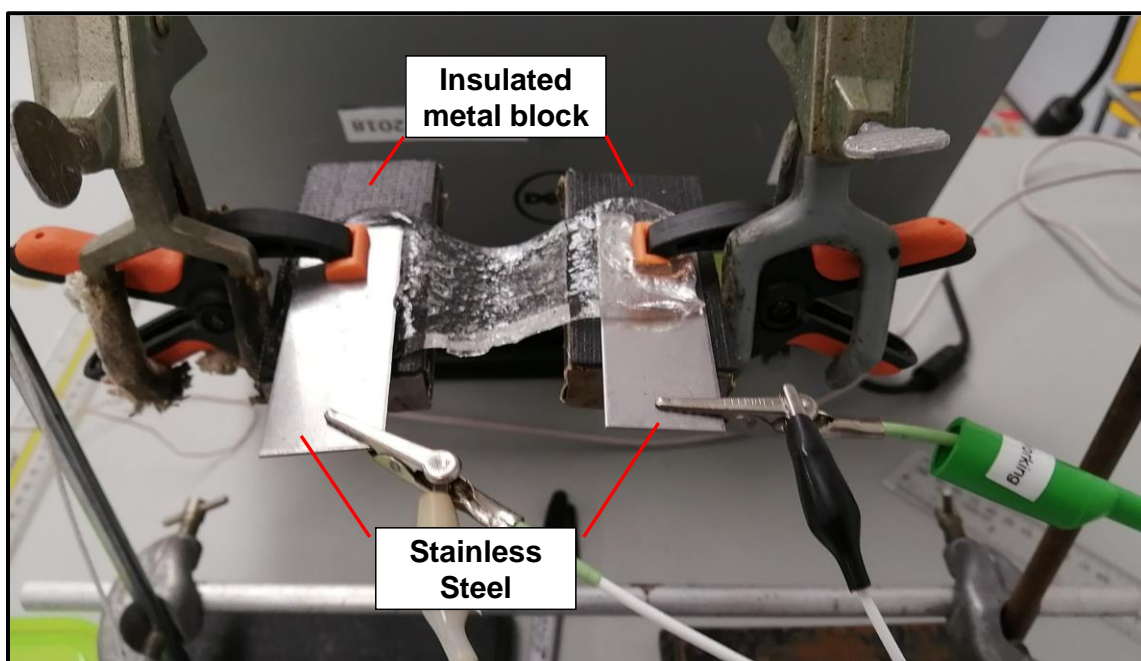
Electrochemical tests were recorded using a model CHI660E, CH Instruments electrochemical workstation. All electrochemical characteristics were carried out using a two-electrode cell that consists of two stainless steel plates (Corrosion-Resistant 316 - Resistivity 74 $\mu\Omega/\text{cm}$) used as current collectors. The 8.2 cm by 8.2 cm square hydrogels were about 3.8 mm to 4.2 mm in thickness. Each hydrogel was measured and cut in half, giving a 4.1 cm by 8.2 cm rectangular shape sample for electrochemical characterization.

For samples 1 to 10 from Table 3.2.1, impedance over time experiments were carried out. First, a Nyquist plot of $B_{3.0}Z_{0.2}$ was recorded in the frequency range between 1×10^6 Hz to 0.1 Hz, with a voltage amplitude of 0.005 V and at the constant polarization of 0 V. The gel was then elongated by 1 cm, 2cm, and 3 cm while the Nyquist plot of the hydrogel was recorded after every elongation. The evaluation of these four Nyquist plots showed us that the bulk conductance had to be evaluated at a frequency between 1000 to 2000 Hz. Hence, a frequency value of 1500 Hz was then used for subsequent impedance over time experiments. These spectra were also recorded at an amplitude of 0.005 V and

at the constant polarization of 0 V. The hydrogel was elongated at a rate of about 0.2 cm s^{-1} until each sample broke into 2 pieces.

To determine the charge transport properties of acrylate-only hydrogels (KPA and KPA-Gly), the hydrogels were set up according to Figure 3.4.2. This setup was used instead of the mechanical equipment shown in Figure 3.4.1(a) was too large to fit into the freezer we owned in our lab. A Nyquist plot was recorded in the frequency range between 1×10^5 Hz to 10 Hz, with an amplitude of 0.005 V and at the constant polarization of 0 V at room temperature (23°C). Then, the hydrogel was elongated by 50% and 100%, recording a Nyquist plot for each elongation. These procedures were repeated after moving the setup into the freezer for low-temperature experiments (-23°C).

Figure 3.4.2: Miniature experimental setup that is able to fit the freezer in our laboratory.



4 Results and Discussion

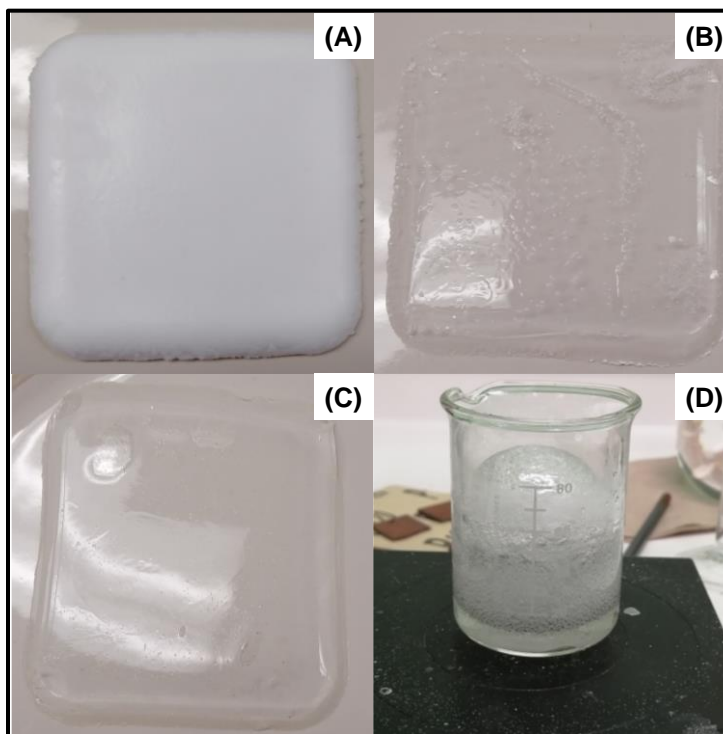
As mentioned in section 1.7, one of the new ideas in this work is to incorporate the electrolyte into the reaction mixture prior to polymerization to tremendously reduce the synthesis time of these hydrogels (from a few days to a few hours). Hence, a few preliminary experiments were carried out to determine the compatibility of this method.

4.1 Effect of Concentration of KOH

The first experiment was to study the effect of KOH concentration on the quality of hydrogels. These hydrogels were assessed by simple visual observations (transparency, homogeneity, color, surface texture), followed by a mechanical and electrochemical test to verify their strength, stretchability, and conductivity. Hence, four hydrogels with different KOH content ($B_{1.5}Z_{0.2}$, $B_{3.0}Z_{0.2}$, $B_{4.5}Z_{0.2}$, and $B_{6.0}Z_{0.2}$) were synthesized as mentioned in Table 3.2.1.

Figure 4.1.1: Photos of freshly synthesized hydrogels with different concentrations of KOH solution.

(A) $B_{1.5}Z_{0.2}$, (B) $B_{3.0}Z_{0.2}$, (C) $B_{4.5}Z_{0.2}$, and (D) $B_{6.0}Z_{0.2}$

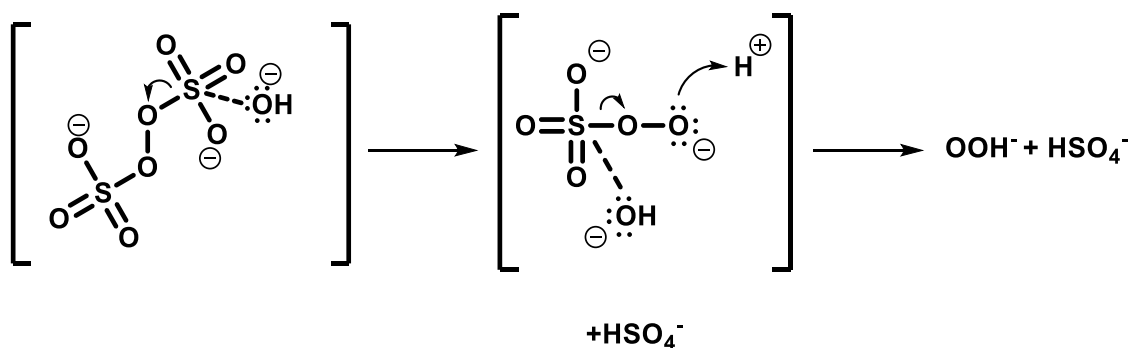


One important remark for all four hydrogels was that these hydrogels gave off a pungent smell, which was not mentioned in literature dealing with hydrogels of similar chemical composition. This phenomenon was further analyzed and will be discussed in detail later.

Starting off with $B_{6.0}Z_{0.2}$, it polymerized and formed a spherical hydrogel when a high concentration of KOH was added (see Figure 4.1.1(D)). This happened before the addition of any radical accelerator, TMEDA, which is a crucial component to activate APS for radical polymerization. We hypothesized that this rapid jellification was due to the base activation of persulfate ions when a high concentration of KOH was introduced.³² In an extremely alkaline environment (such as 6.0 M KOH in our case), the OH^- reacts with

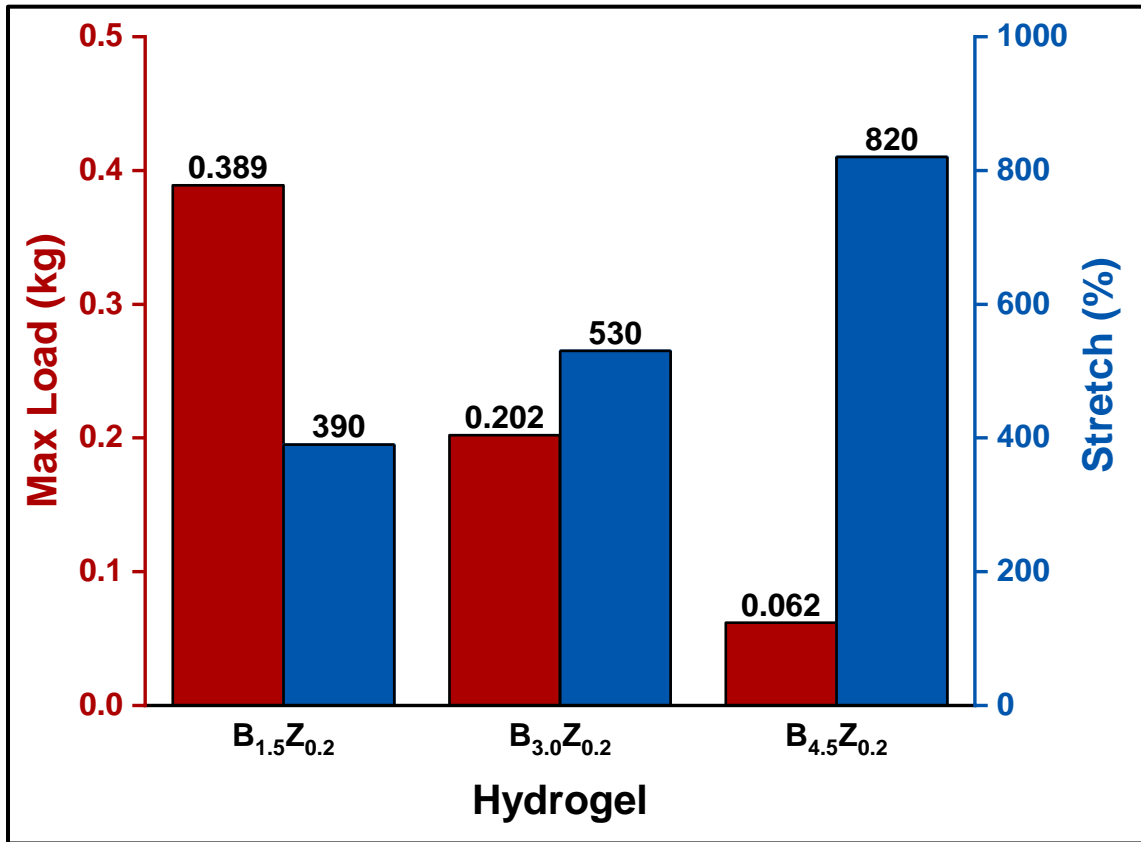
persulfate ions to form superoxide ions. These unstable superoxide ions will then react with other persulfate ions to form sulfate and oxygen radicals, allowing initiation of the polymerization process without TMEDA (see Scheme 4.1.1).

Scheme 4.1.1: Base activation of persulfate ions



For the hydrogel composition labeled as B_{1.5}Z_{0.2}, the liquid reaction mixture was initially transparent and colorless (before it was exposed to the UV rays needed for radical initiation). However, the hydrogel turned white and opaque as the polymerization proceeded (see Figure 4.1.1(A)). This is because zinc hydroxide precipitated out from the reaction mixture during the polymerization step.³³ Precipitation of zinc hydroxide, however, only occurs at a very low concentration of base, which explains why B_{3.0}Z_{0.2} and B_{4.5}Z_{0.2} remained clear and colorless (Figure 4.1.1(B) and (C)).

Figure 4.1.2: Bar chart of the max load (red) and percentage of stretch (blue) of $B_{1.5}Z_{0.2}$, $B_{3.0}Z_{0.2}$, and $B_{4.5}Z_{0.2}$.

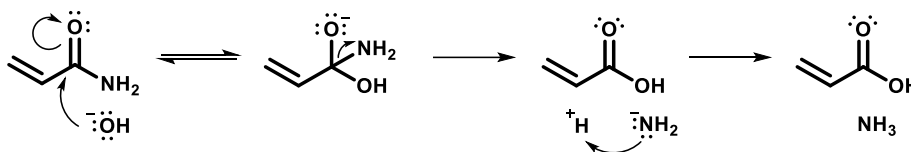


The hydrogels were then subjected to mechanical tests. Figure 4.1.2 displays the results of the mechanical test. The red bar chart represents the maximum load the hydrogel can withstand (in kg) before breaking; while the blue bar chart shows the maximum length the hydrogel can be stretched (in %) before breaking. Note that $B_{6.0}Z_{0.2}$ was not included in these tests as its shape was completely different than other hydrogels prepared in this series of compositions. From the bar charts in Figure 4.1.2, $B_{1.5}Z_{0.2}$ appeared to be the strongest hydrogel, withstanding 0.389 kg before breaking, while $B_{4.5}Z_{0.2}$ was the weakest. However, $B_{1.5}Z_{0.2}$ was the least stretchable (390 % elongation), but $B_{4.5}Z_{0.2}$ reached up to 820 % elongation from the hydrogel's initial length. One trend observed from this

experiment is that when the concentration of KOH increases, the hydrogels become more stretchable but weaker.

We hypothesized that KOH was chemically reacting with the polymer network, hence affecting the hydrogels' mechanical properties. After the assessment of all possible reactivities of the reactants, the most probable side reaction is the hydrolysis of acrylamide in highly concentrated KOH to form acrylic acid and ammonia (see Scheme 4.1.2).

Scheme 4.1.2: Hydrolysis of acrylamide to form acrylic acid and ammonia.

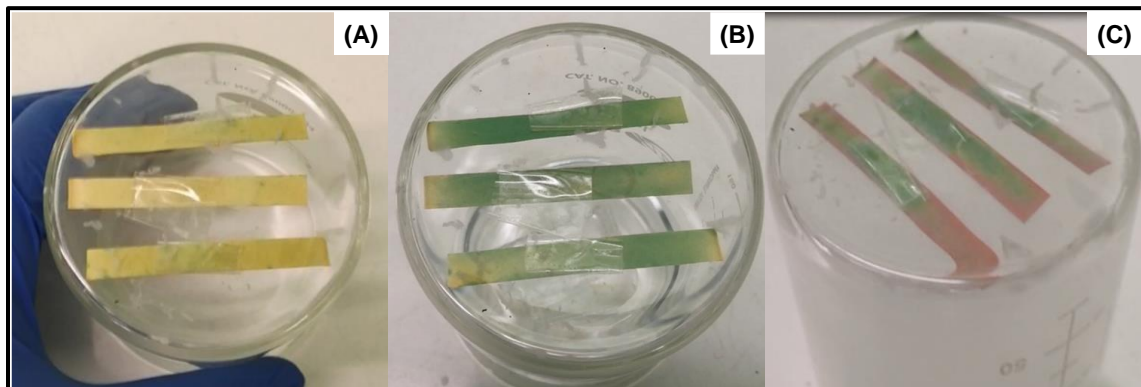


Before jumping into the discussion of the reaction mentioned above, one extremely important note to make here is that this problem was only discovered later in the project. However, we think that it is best to include the discussion here to clarify our observations before moving on to other experiments.

To prove that hydrolysis of acrylamide had happened, a simple gas-phase experiment was carried out. Since ammonia gas is basic, a few pH papers were taped in a beaker (see Figure 4.1.3(A)), and the beaker was used to cover a petri dish containing a piece of B_{3.0}Z_{0.2}. The pH paper turned from yellow (neutral) to blue (basic) after a few seconds (see Figure 4.1.3(B)). Then, the beaker was lifted and slowly moved to cover a petri dish containing concentrated HCl solution. White smoke was observed after a few seconds and the blue pH paper (basic) slowly turned red (acidic, see Figure 4.1.3(C)). The first part of the experiment proved that the fume formed here was alkaline. The second part of the experiment helped us identify that the fume was ammonia (NH₃) since the reaction

of NH_3 gas and hydrochloric acid vapor produces white smoke. The determination of NH_3 fume also matches the pungent smell for all the hydrogel mentioned initially.

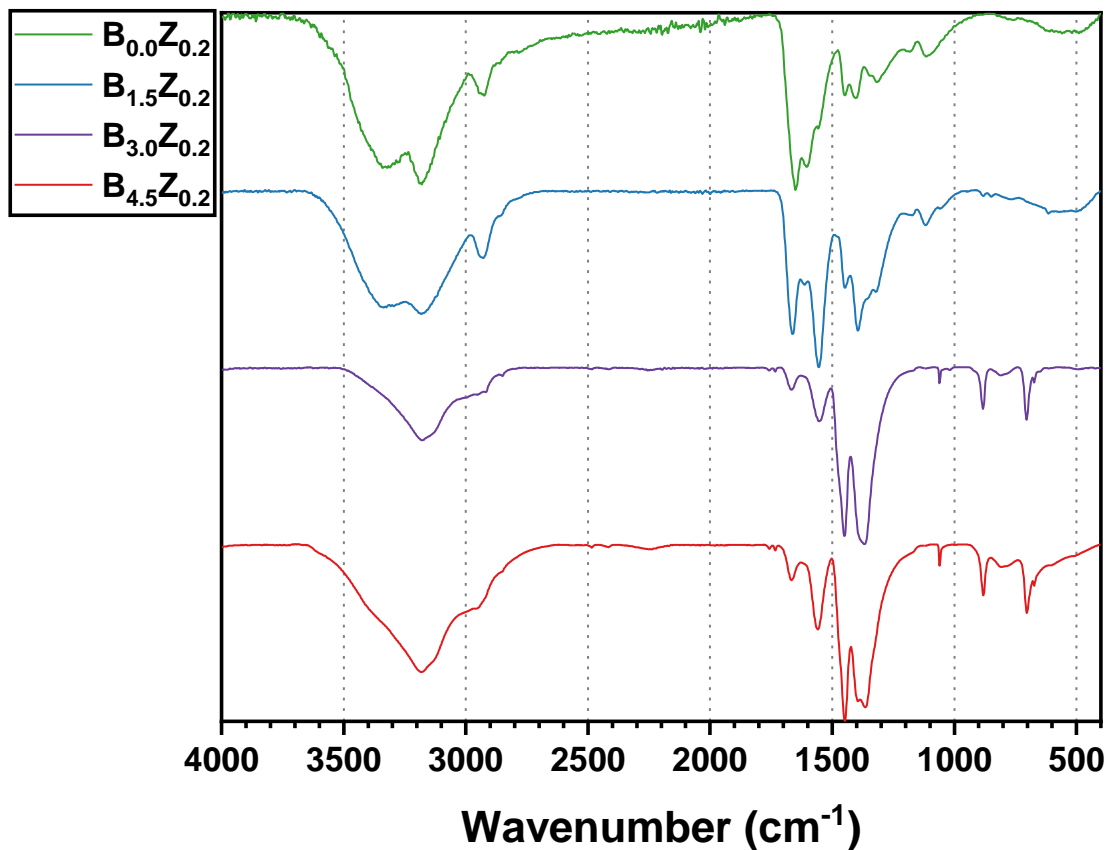
Figure 4.1.3: Experiment to show the release of ammonia gas. (A) Color of pH paper before the experiment, (B) color of pH paper when exposed to hydrogel, and (C) color of pH paper when exposed to concentrated HCl



Besides that, $\text{B}_{0.0}\text{Z}_{0.2}$, $\text{B}_{1.5}\text{Z}_{0.2}$, $\text{B}_{3.0}\text{Z}_{0.2}$, and $\text{B}_{4.5}\text{Z}_{0.2}$ were dried and ground to prepare suitable samples for FTIR analysis. For the ease of comparison, the FTIR of $\text{B}_{0.0}\text{Z}_{0.2}$, $\text{B}_{1.5}\text{Z}_{0.2}$, $\text{B}_{3.0}\text{Z}_{0.2}$, and $\text{B}_{4.5}\text{Z}_{0.2}$ were overlaid and shown in Figure 4.1.4. The fully assigned spectra of these four individual hydrogels can be found in the appendix.

Analysis of FTIR spectra presented in Figure 4.1.4 indicated that hydrolysis of acrylamide resulting in the production of acrylic acid was indicated by a decrease in the peak intensity around 1650 cm^{-1} region, which is assigned to the $\text{C}=\text{O}$ stretch of amide. Both $\text{B}_{0.0}\text{Z}_{0.2}$ and $\text{B}_{1.5}\text{Z}_{0.2}$ displayed strong signals in this wavenumber range as compared to hydrogels containing higher concentrations of KOH ($\text{B}_{3.0}\text{Z}_{0.2}$ and $\text{B}_{4.5}\text{Z}_{0.2}$). Also, acrylamide has two broad N-H stretch peaks around 3350 cm^{-1} and 3150 cm^{-1} regions. These two peaks were observed in $\text{B}_{0.0}\text{Z}_{0.2}$ and $\text{B}_{1.5}\text{Z}_{0.2}$ but the peak at 3350 cm^{-1} disappeared for $\text{B}_{3.0}\text{Z}_{0.2}$, and $\text{B}_{4.5}\text{Z}_{0.2}$.

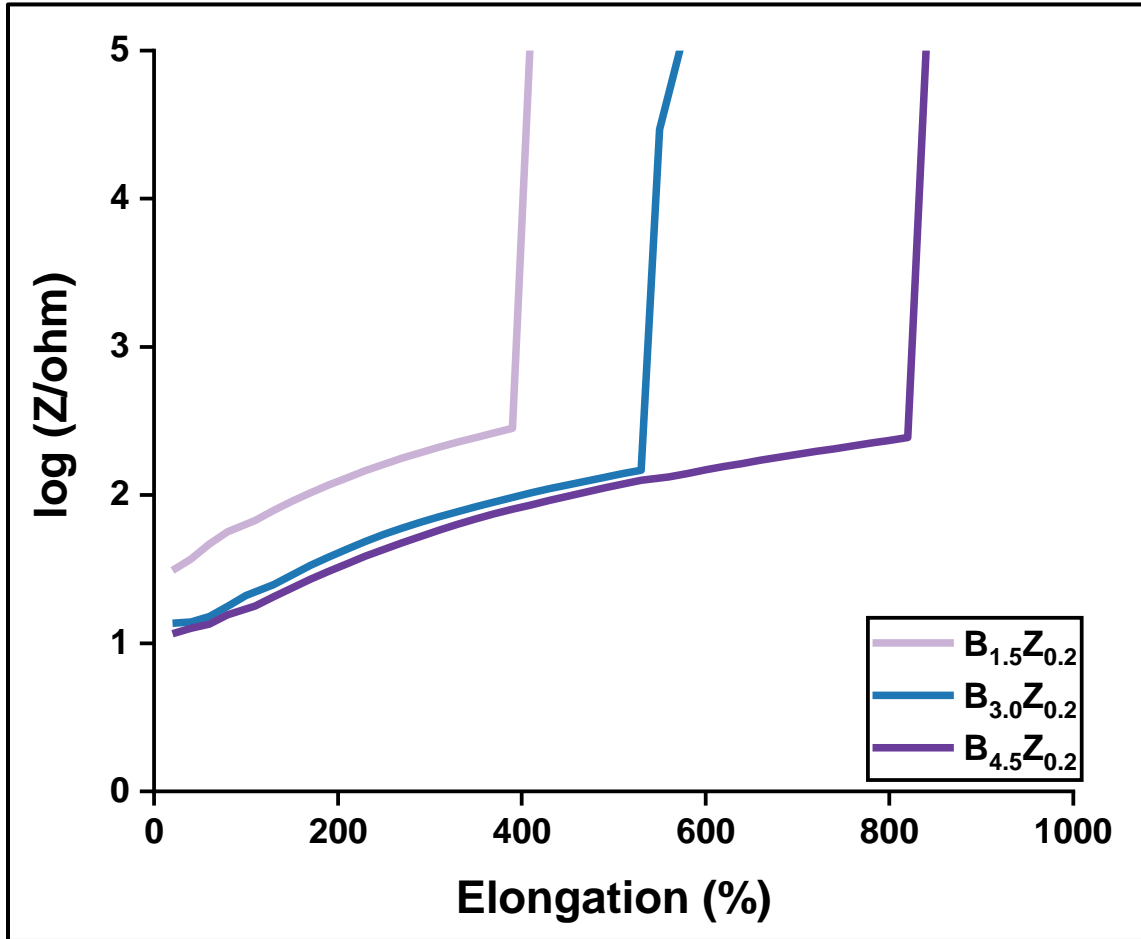
Figure 4.1.4: FTIR spectra of $B_{0.0}Z_{0.2}$, $B_{1.5}Z_{0.2}$, $B_{3.0}Z_{0.2}$, and $B_{4.5}Z_{0.2}$ stacked together for comparison.



One important signal that should be mentioned is the peak at 1750 cm^{-1} observed in $B_{3.0}Z_{0.2}$ and $B_{4.5}Z_{0.2}$, which is the C=O stretch for carboxylic acid. However, since this signal was very weak, it could be argued that it is just a noise. On a side note, three very distinct signals in the range from 700 cm^{-1} to 1050 cm^{-1} can be identified for $B_{3.0}Z_{0.2}$, and $B_{4.5}Z_{0.2}$ but not $B_{0.0}Z_{0.2}$ and $B_{1.5}Z_{0.2}$. These peaks were assigned as C=C bend for amide (700 cm^{-1}), C=C bend for carboxylic acid (880 cm^{-1}), and C-N bend for amide (1050 cm^{-1}). These peaks indicated that there might be starting material (acrylamide and acrylate monomer) left unreacted in the last two hydrogels.

The impedance over time spectra of these hydrogels were recorded as described in the experimental section. The goal of this test was to compare how their bulk impedance changes while being elongated (see Figure 4.1.5).

Figure 4.1.5: Spectra of total impedance for $B_{1.5}Z_{0.2}$, $B_{3.0}Z_{0.2}$, and $B_{4.5}Z_{0.2}$ as these hydrogels were elongated. These spectra were recorded at frequency of 1500 Hz.



Since the time scale in these experiments is defined as the time needed to elongate the sample from its initial length to its breaking point, we can estimate the % elongation of these hydrogels using the rate of elongation, which is 0.2 cm/s. A trend of increasing total impedance (bulk resistance and capacitive reactance) as the hydrogels were elongated,

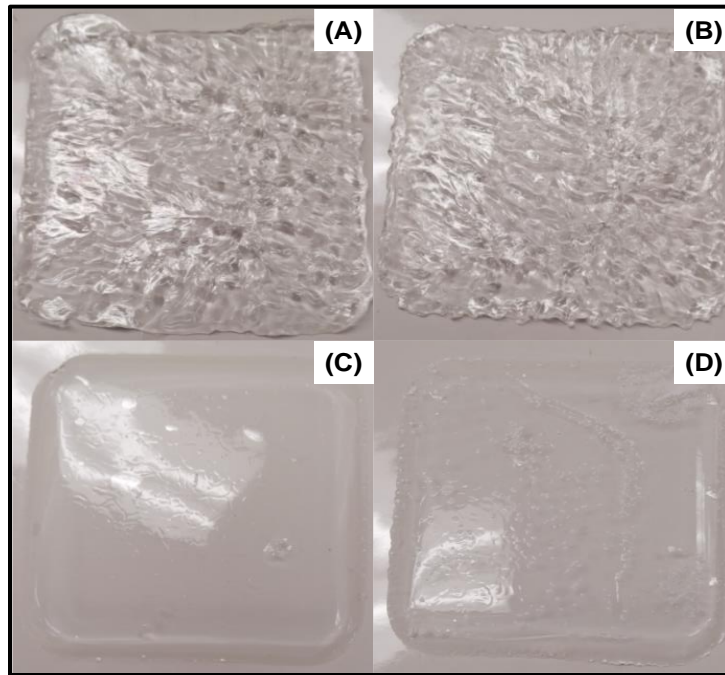
followed by a sharp spike was observed for all hydrogels. This is an obvious behavior because ions had to travel a longer distance to reach the polarized electrodes. The sharp spike of total impedance indicates the moment when the hydrogel breaks.

From Figure 4.1.5, $B_{1.5}Z_{0.2}$ had the highest initial impedance, followed by $B_{3.0}Z_{0.2}$ and lastly $B_{4.5}Z_{0.2}$, though the difference between these two samples is minimal. Since zinc hydroxide precipitated during the polymerization of $B_{1.5}Z_{0.2}$, this material has lower ionic conductivity (highest bulk impedance) not only because of its lowered KOH concentration (KOH is the main contribution to ionic conduction) but also due to the presence of the solid fraction with the polymer impeding the movement of mobile ions. This in total makes $B_{1.5}Z_{0.2}$ the least favorable for our application. Altogether, the trend demonstrated in Figure 4.1.5 follows the trend normally observed in most of the liquid and hydrogel electrolytes in terms of the effect of concentration on mobile ions and also agrees well with the literature.¹⁴

4.2 Effect of KOH and Zinc Acetate Addition

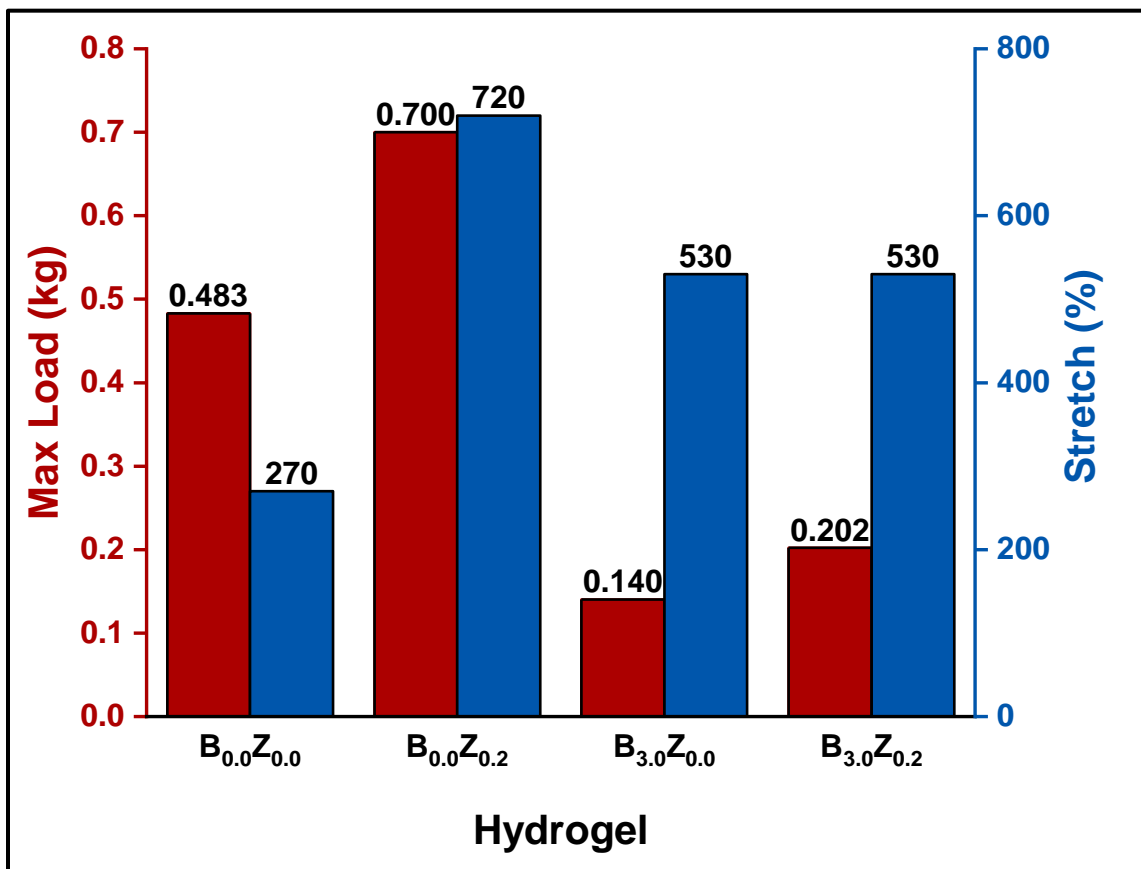
Based on the results demonstrated in the previous section, 3.0 M KOH was introduced to the hydrogel and was further tested for the effect of zinc acetate additive. 0.2 M of zinc acetate was chosen as a standard concentration based on optimization carried out by other groups,¹⁵ which was also justified in the introduction. Furthermore, three hydrogels: one without any ionic component ($B_{0.0}Z_{0.0}$), one with 0.2 M zinc acetate ($B_{0.0}Z_{0.2}$), and the last with 3.0 M KOH without any zinc acetate ($B_{3.0}Z_{0.0}$), were compared. Their chemical compositions are detailed in Table 3.2.1 and photos of these hydrogels after the synthesis are presented in Figure 4.2.1.

Figure 4.2.1: Photos of synthesized hydrogels; (A) $B_{0.0}Z_{0.0}$, (B) $B_{0.0}Z_{0.2}$, (C) $B_{3.0}Z_{0.0}$, and (D) $B_{3.0}Z_{0.2}$. $B_{3.0}Z_{0.2}$ is added into the group for side-by-side comparison.



As demonstrated in Figure 4.2.1, all four hydrogels were colorless and transparent. One distinctive difference was that the $B_{0.0}Z_{0.0}$ and $B_{0.0}Z_{0.2}$ had uneven wrinkled surfaces as compared to $B_{3.0}Z_{0.0}$ and $B_{3.0}Z_{0.2}$. What we recognized from this series of samples was that $B_{0.0}Z_{0.0}$ and $B_{0.0}Z_{0.2}$ samples did not release the pungent smell that we had identified to be NH_3 .

Figure 4.2.2: Bar chart of the max load (red) and percentage of stretch (blue) of $B_{0.0}Z_{0.0}$, $B_{0.0}Z_{0.2}$, $B_{3.0}Z_{0.0}$, and $B_{3.0}Z_{0.2}$.



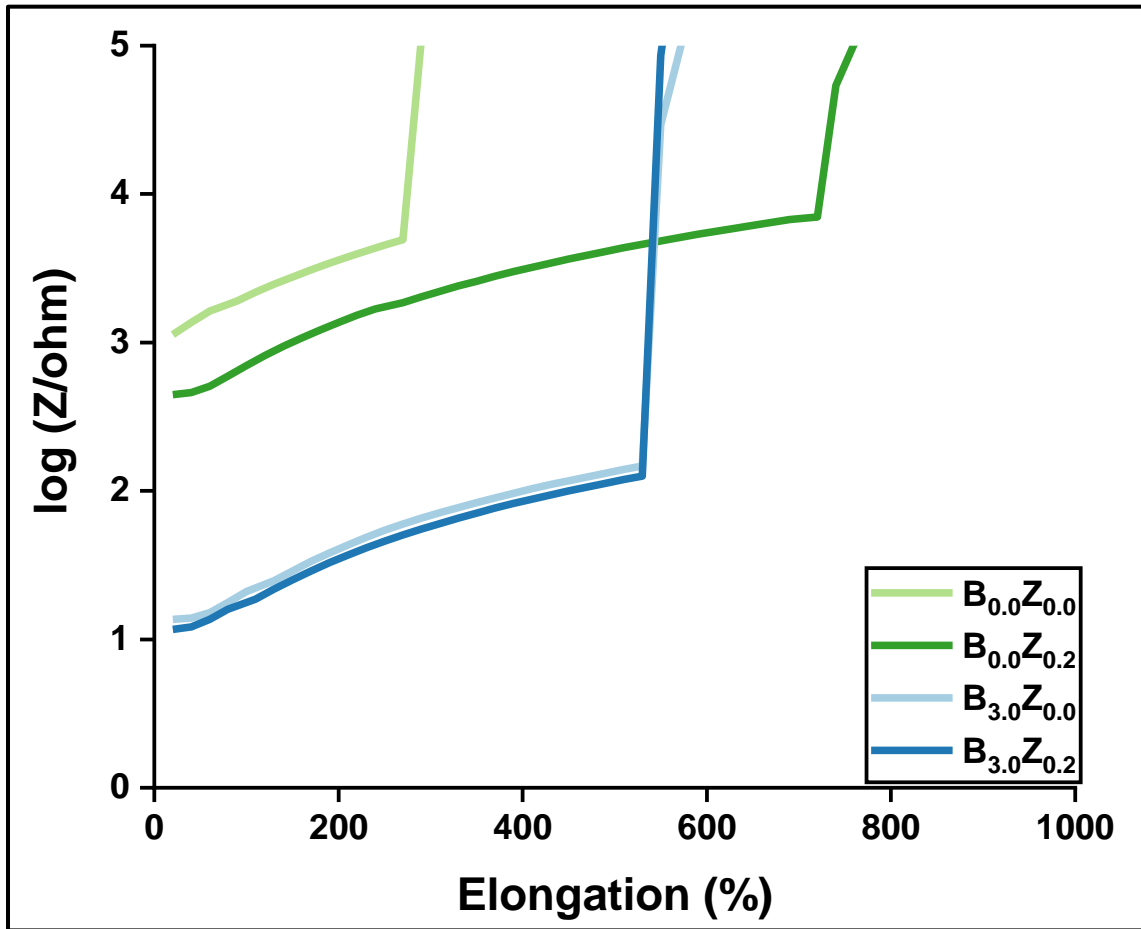
These four hydrogels were also subjected to mechanical tests. It is important to make clear that the results should be treated in two separate groups: (1) between $B_{0.0}Z_{0.0}$ and $B_{0.0}Z_{0.2}$; (2) between $B_{3.0}Z_{0.0}$ and $B_{3.0}Z_{0.2}$. As mentioned in the previous section, acrylamide will decompose to acrylic acid when exposed to high molarity of KOH. The polymer compositions are very different, hence making it unfair to compare all four hydrogels at the same time.

When a comparison was made between hydrogels with and without zinc acetate, the hydrogels with zinc acetate ($B_{0.0}Z_{0.2}$ and $B_{3.0}Z_{0.2}$) appeared to be stronger than those without zinc acetate ($B_{0.0}Z_{0.0}$ and $B_{3.0}Z_{0.0}$). This can be understood as an effect of zinc ions.

The Zn^{2+} ions in $\text{B}_{0.0}\text{Z}_{0.2}$ and $\text{B}_{3.0}\text{Z}_{0.2}$ are acting as an ionic crosslinker, further increasing the crosslink density of the hydrogel, hence improving the mechanical strength of the hydrogel.³⁴

In terms of the stretchability of the hydrogels, no obvious trend was observed. For example, after the addition of zinc acetate, the stretchability of the hydrogel was significantly improved (increased by 450 %) between $\text{B}_{0.0}\text{Z}_{0.0}$ and $\text{B}_{0.0}\text{Z}_{0.2}$. On the other hand, it did not have any effect on $\text{B}_{3.0}\text{Z}_{0.0}$ and $\text{B}_{3.0}\text{Z}_{0.2}$. We hypothesized that this inconsistency in trend might be due to experimental errors. As described in the experimental section, the corkscrews were tightened to firmly hold the hydrogels in place before they were elongated. Since hydrogels are soft materials, they can be easily squished. Hence, too much torque might be applied to the corkscrews during this step, affecting the results of some of the hydrogels.

Figure 4.2.3: Spectra of total impedance for $B_{0.0}Z_{0.0}$, $B_{0.0}Z_{0.2}$, $B_{3.0}Z_{0.0}$ and $B_{3.0}Z_{0.2}$ as these hydrogels were elongated. These spectra were recorded at frequency of 1500 Hz.

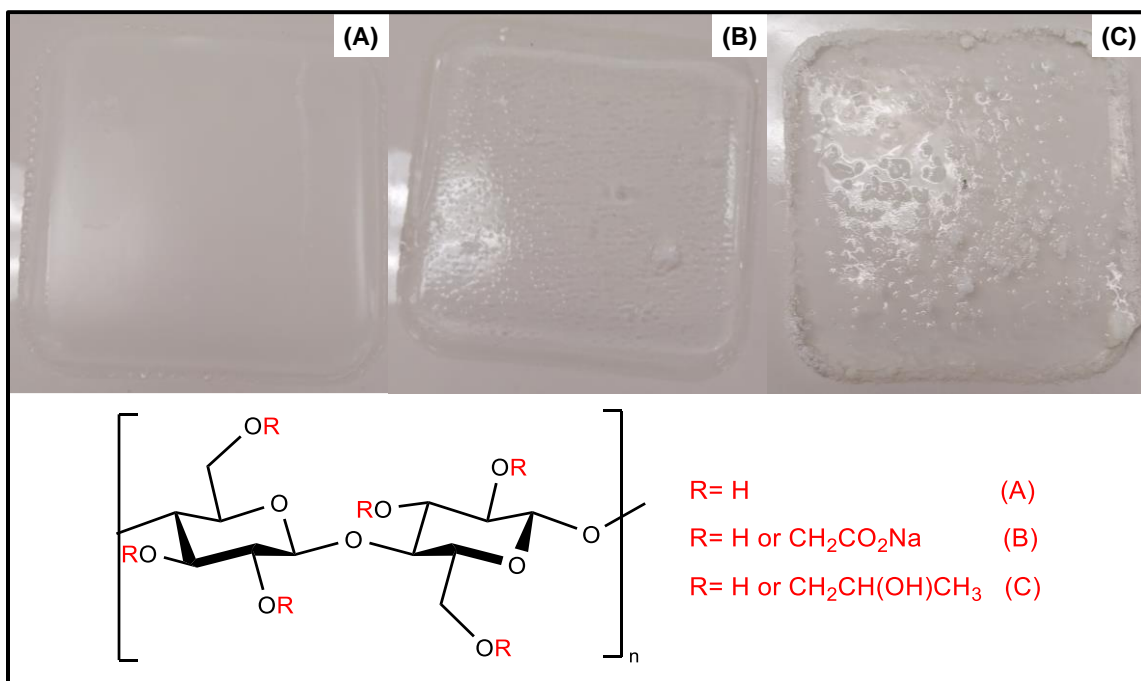


Moving on, for this series of samples, the impedance over time characteristics were also recorded. The x-axis (time) of the spectra was once again converted to percentage elongation as shown in Figure 4.2.3. What can be concluded is that $B_{0.0}Z_{0.0}$ had the highest initial impedance. As more ions were introduced into the hydrogel matrix, the conductivity of the hydrogel increased. Hence, $B_{0.0}Z_{0.2}$ had a lower impedance than $B_{0.0}Z_{0.0}$, followed by $B_{3.0}Z_{0.0}$ and $B_{3.0}Z_{0.2}$. Both $B_{3.0}Z_{0.0}$ and $B_{3.0}Z_{0.2}$ had a very similar impedance because the concentration of zinc acetate solution (0.2 M) introduced was minor compare to KOH and thus, its contribution to the number of mobile charge carriers is negligible. On the other

hand, the addition of 3.0 M KOH solution to the polymer matrix leads to an increase in conductivity (decrease in impedance) by two orders of magnitude. It is important to recall at this point of optimization of proposed chemistries that the zinc acetate solution was introduced to help improve the rechargeability of the ZAB system (as mentioned in section 1.4), not to improve the conductivity of the electrolyte itself.

4.3 Addition of Cellulose

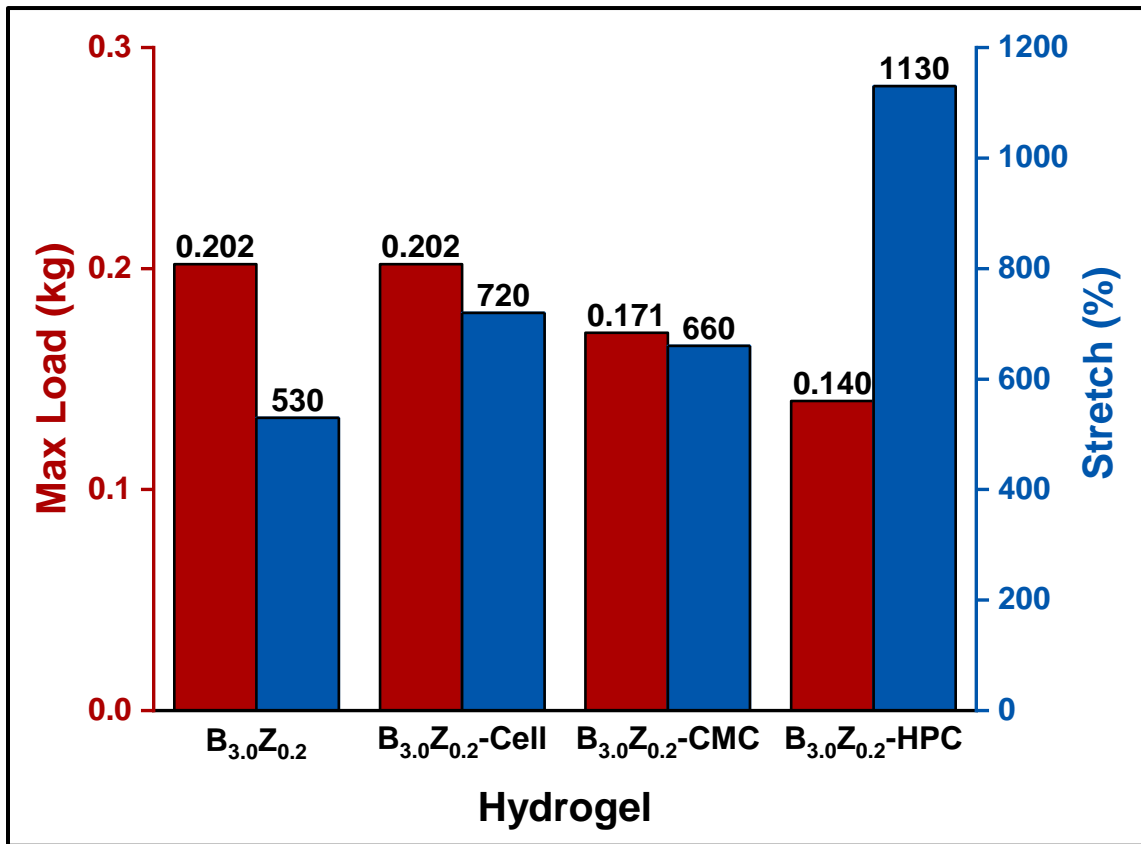
Figure 4.3.1: Images of freshly synthesized hydrogels containing different variants of cellulose. (A) B_{3.0}Z_{0.2}-Cell, (B) B_{3.0}Z_{0.2}-CMC, and (C) B_{3.0}Z_{0.2}-HPC



The last experiment planned for the optimization of the proposed electrolyte was the incorporation of different types of cellulose into the hydrogel (see Figure 4.3.1). The chemical structures of cellulose used in this work are also shown in the same figure. Since celluloses are natural polymers that are insoluble in the solvent (water), therefore the solid remains could be observed. For B_{3.0}Z_{0.2}-Cell (Figure 4.3.1(A)), the solid was spread

homogeneously throughout the hydrogel, giving translucent and colorless hydrogel. For $B_{3.0}Z_{0.2}$ -CMC and $B_{3.0}Z_{0.2}$ -HPC (Figure 4.3.1(B) and (C)), large agglomerates of CMC salt were spread throughout the hydrogel, giving a clear and colorless hydrogel with uneven surfaces.

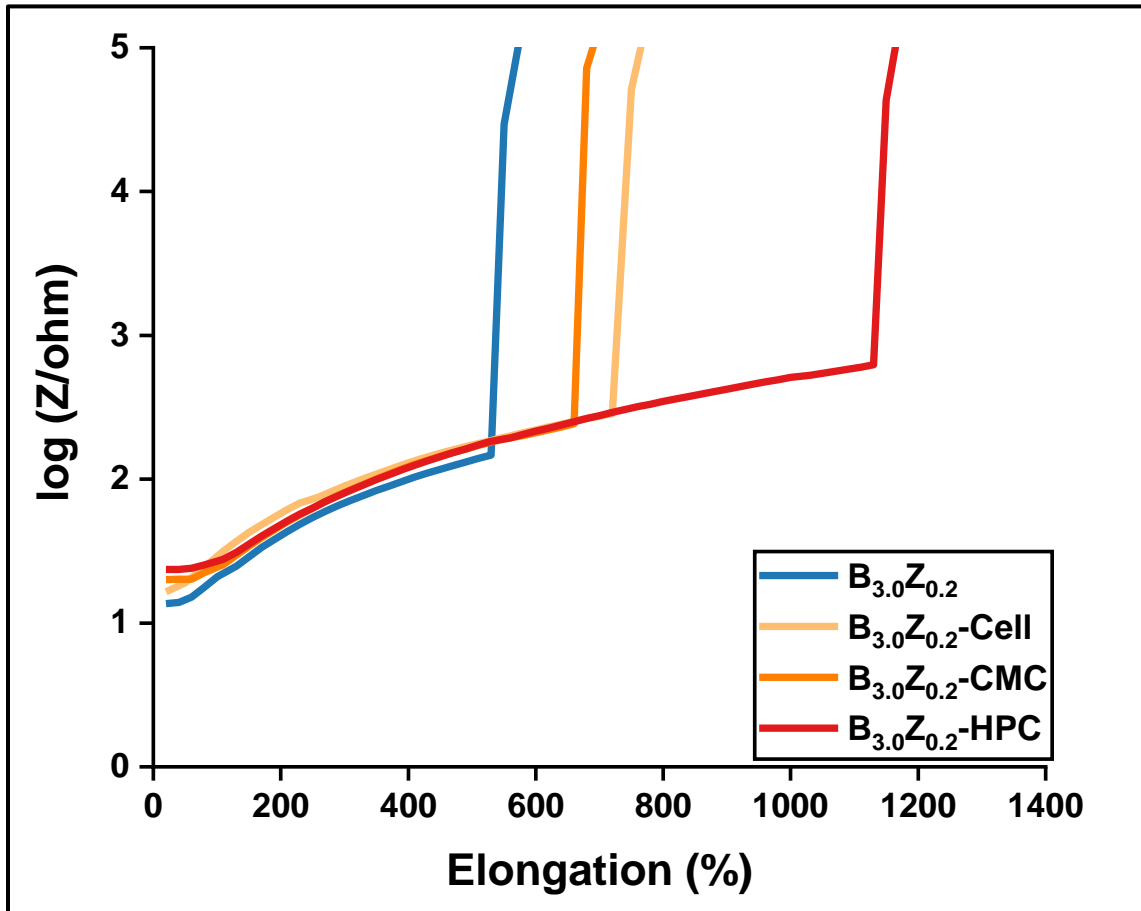
Figure 4.3.2: Bar chart of the max load (red) and percentage of stretch (blue) of $B_{3.0}Z_{0.2}$, $B_{3.0}Z_{0.2}$ -Cell, $B_{3.0}Z_{0.2}$ -CMC, and $B_{3.0}Z_{0.2}$ -HPC



Regarding the mechanical characteristics of cellulose-modified hydrogels, we observed that the addition of plain cellulose did not change the mechanical strength of sample $B_{3.0}Z_{0.2}$ -Cell. On the other hand, the addition of CMC and HPC slightly lowered the mechanical strength of the hydrogel (by 0.031 kg and 0.062 kg respectively). However, an improvement in the stretchability of all three hydrogels was observed. Comparing the

three hydrogels with cellulose, we can conclude that the addition of plain cellulose and CMC improved the stretchability of the original hydrogel (without cellulose) to almost the same extent. Surprisingly, even though the HPC cellulose agglomerated within the hydrogel, this sample demonstrated notable improvement in stretchability, exceeding the stretchability of $B_{4.5}Z_{0.2}$ shown in the previous section. Since cellulose contains a lot of hydroxyls (OH) functional groups, a lot of hydrogen bonds can be formed either between polymer chains. These weak hydrogen bonds can be readily broken when stretched, enhancing the stretchability of the hydrogels.²¹

Figure 4.3.3: Spectra of total impedance for $B_{3.0}Z_{0.2}$, $B_{3.0}Z_{0.2}$ -Cell, $B_{3.0}Z_{0.2}$ -CMC, and $B_{3.0}Z_{0.2}$ -HPC as these hydrogels were elongated. These spectra were recorded at frequency of 1500 Hz.



Furthermore, similar impedance over time experiments were carried out and the time axis were converted to percentage elongation to assess the effect of cellulose on electrical properties. From Figure 4.3.3, all three hydrogels had a slightly higher initial impedance after the addition of cellulose. This could be due to the presence of agglomerates embedded within the material, disrupting the movement of ions, and thus increasing the impedance. Based on a set of mechanical and electrochemical tests we have concluded that the cellulose additive did not influence the hydrogel's conductivity, but at the same time, it improved the mechanical characteristics. These observations are very consistent with literature, where cellulose was proposed to be a good additive to improve the stretchability of similar hydrogels.²¹

4.4 Questioning Our Methodology

As mentioned above in section 4.1, we discovered that acrylamide would decompose to acrylic acid and ammonia in a high concentration of KOH. This begs the question that if our new methodology of incorporating all the electrolyte components (KOH and zinc acetate) before the formation of hydrogels is suitable. This would also explain why other research groups might have avoided this method and opted for a more time-consuming electrolyte-soaking process when synthesizing hydrogels with similar compositions. In other words, clarification is needed on whether polyacrylamide (not acrylamide monomers) is stable when subjected to a high concentration of KOH.

To answer this question, we tried to reproduce the hydrogel reported by Chen et al with a slight modification.²⁰ The only modification to the procedure was during the final step of the synthesis, radical polymerization was initiated using UV irradiation instead of

heating at 60°C for two hours. Their hydrogel is chosen because the polymer compositions are very similar to our work, which are polyacrylamide and polyacrylic acid.

Following their procedure, a clear and colorless hydrogel was successfully synthesized, and it was left to dry in the oven at 40°C for two days. After two days of drying, the hydrogel was submerged in a beaker of electrolyte for 20 hours. To prove that the electrolyte was in fact absorbed by the hydrogel, the mass of the dried hydrogel before and after soaking in the electrolyte was recorded. There was a 541 % increase in mass (from 1.13 g to 7.23 g). That hydrogel also released a small amount of pungent smell similar to $B_{3.0}Z_{0.2}$, which was deduced as NH_3 gas. Although no further analysis was carried out, we believed that the distinct NH_3 smell alone was a strong enough prove that polyacrylamide had undergone similar hydrolysis reaction to form acrylic acid and ammonia. Hence, we have concluded that polymerized acrylamide is also prone to chemical reaction with concentrated KOH, and therefore should be excluded from the proposed formulations.

Although, the problem of polyacrylamide decomposition is not well-reported in literature, we have found that *Tan et al* also synthesized similar alkaline hydrogels using polyacrylamide.³⁵ After soaking in KOH solution, their hydrogel also showed similar unwanted hydrolysis reaction to form acrylic acid and ammonia. However, the mechanism detailing the acrylamide decomposition was not included nor justified in this work.

4.5 New Formulation

Having a deeper understanding on the reactions that happened during the synthesis of hydrogels, some modifications on the formulation were made. First and foremost, as

detailed in sections 4.1 and 4.4, addition of a highly concentrated KOH solution promotes the hydrolysis of acrylamide and polyacrylamide into acrylic acid and ammonia. Therefore, acrylamide was excluded from the final hydrogel formulation, leaving only potassium polyacrylate as the main polymer chain.

Besides that, in section 4.1, we noticed that at high concentration of KOH solution, radical polymerization can be initiated without the addition of TMEDA or exposing the reaction mixture to UV light. This was not reported in literature since most of research group working on similar alkaline hydrogels used a post-synthesis KOH soaking method to introduce ionic component to the electrolyte (unlike our method where KOH solution is mixed with all reactants before polymerization). It turned out that this pre-mixing approach not only allows us to shorten the total synthesis time (from an average of 48 hours for drying of hydrogel and then soaking them in KOH solution to approximately 3 hours in the case of pre-mixing of KOH), but also allows us to omit TMEDA (accelerator of polymerization), the most toxic reactant in the proposed formulation. Thus, using KOH pre-mixing method makes the synthesis more environmentally benign, which is considered as a significant step forward in terms of green chemistry principles.

Additionally, the radical initiator, ammonium persulfate (APS), will be replaced with potassium persulfate (KPS), to avoid any potential in the formation of ammonium hydroxide when exposed to KOH. Since improvements due to the cellulose addition are minor and cellulose-embedded samples required further optimization in order to eliminate agglomeration, we decided to exclude the cellulose additive in the following studies on further optimization of the hydrogel composition. We initially planned to add glycerol to give the hydrogel antifreeze properties. Since no experiments had been carried out yet at

this point for glycerol, they will still be included in future experiments. A comparison between the old formulation and new formulation is summarized in Table 4.5.1.

Table 4.5.1: Comparison between the old formulation and the new formulation.

Old plan	New formulation
<ul style="list-style-type: none"> • Polymer network consists of polyacrylamide and potassium polyacrylate. • Ammonium persulfate (APS) is used as radical initiator and TMEDA is used as radical accelerator. • Reaction mixture is exposed to UV light for polymerization. • Different variants of cellulose are added to improve the stretchability of the hydrogel. • Glycerol is added to give the hydrogel antifreeze properties. 	<ul style="list-style-type: none"> • Polymer network consists of only potassium polyacrylate • Potassium persulfate (KPS) is used as radical initiator. High concentration of KOH is used as radical activation • Glycerol is added to give the hydrogel antifreeze properties

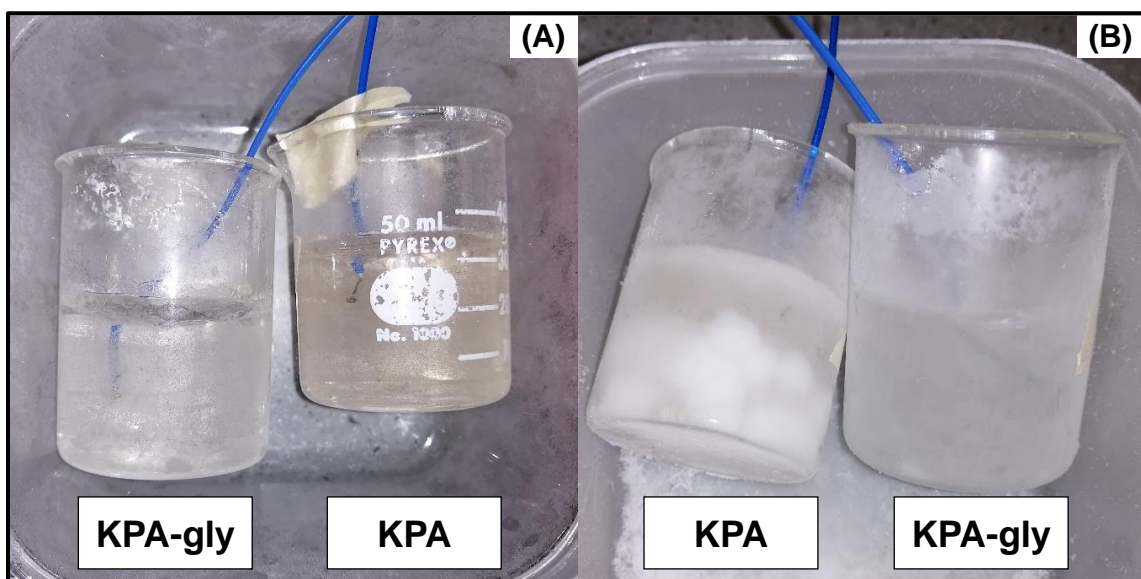
4.6 Potassium Polyacrylate Hydrogel with Glycerol: Synthesis, Freezing and Mechanical Properties

Alkaline potassium polyacrylate hydrogel (KPA) is a well-studied electrolyte and was recently published by *Ivey et al*, one of the leading groups in the area of flexible batteries from University of Alberta.³⁶ Comparing work demonstrated by these researchers, we introduced some modifications of the synthetic procedure. As such, instead of initiating polymerization in an 60°C oven, the reaction mixture was poured into a mold set up in an ultrasonic bath and the polymerization was initiated through ultrasonic agitation. These hydrogels were not synthesized through UV irradiation because no hydrogels were formed after 6 hours of exposing the solution mixture in UV light. We discovered that the agitation

step played a vital role to ensure KPS dissolve into the solution mixture and start the radical polymerization process.

Moving on, to synthesize KPA with antifreeze properties, 0.35 mL of glycerol (1% total volume of the reaction mixture) was also incorporated. Unfortunately, the reaction mixture remained a viscous liquid despite increasing the time in the ultrasonic bath. We later discovered that increasing the amount of MBAA crosslinker (from 0.0336 g to 0.0945 g) helped in the formation of a clear and colorless solid hydrogel (KPA-Gly). However, due to time constraint, experiments were not carried out to accurately pinpoint the reason why MBAA crosslinker will affect the synthesis KPA-Gly nor were we able to optimize the amount of MBAA needed to form KPA-Gly with desired flexibility.

Figure 4.6.1: Low-temperature tests of KPA and KPA-Gly in (A) -25 °C and (B) -80 °C



The antifreeze properties of both KPA and KPA-Gly were compared and demonstrated in Figure 4.6.1. A low-temperature (-23°C) observation was initially carried out after leaving KPA and KPA-Gly overnight in the laboratory freezer. Both hydrogels

remained transparent, flexible, and homogeneous without any crystallized water present (Figure 4.6.1(A)). Furthermore, the same samples were frozen at -80°C (left overnight prior observing), and visible large crystals of ice were identified for KPA but not for KPA-Gly sample (Figure 4.6.1(B)).

In order to rationally guide us on the anti-freeze effect of KOH, zinc acetate, and glycerol, a set of samples were prepared (see Table 4.6.1). These samples were left in the freezer (-23°C) overnight and the photos before and after they were frozen are shown in Figure 4.6.2. From the figure, it is obvious that samples 1 to 5 were frozen but not for samples 6 to 8. This simple test allowed us to identify that 6.0 M KOH solution without glycerol contributes to the antifreeze properties, withstanding temperature as low as -23°C . This explains why KPA in Figure 4.6.1 remained transparent and flexible in -23°C but not in -80°C . However, glycerol, an antifreeze agent is still needed to make hydrogels functional in more extreme temperatures (such as -80°C).

Figure 4.6.2: Photos of 5 mL samples of different chemical compositions before and after they were frozen. These samples were prepared to study the antifreeze properties of the electrolyte system and not the hydrogel.

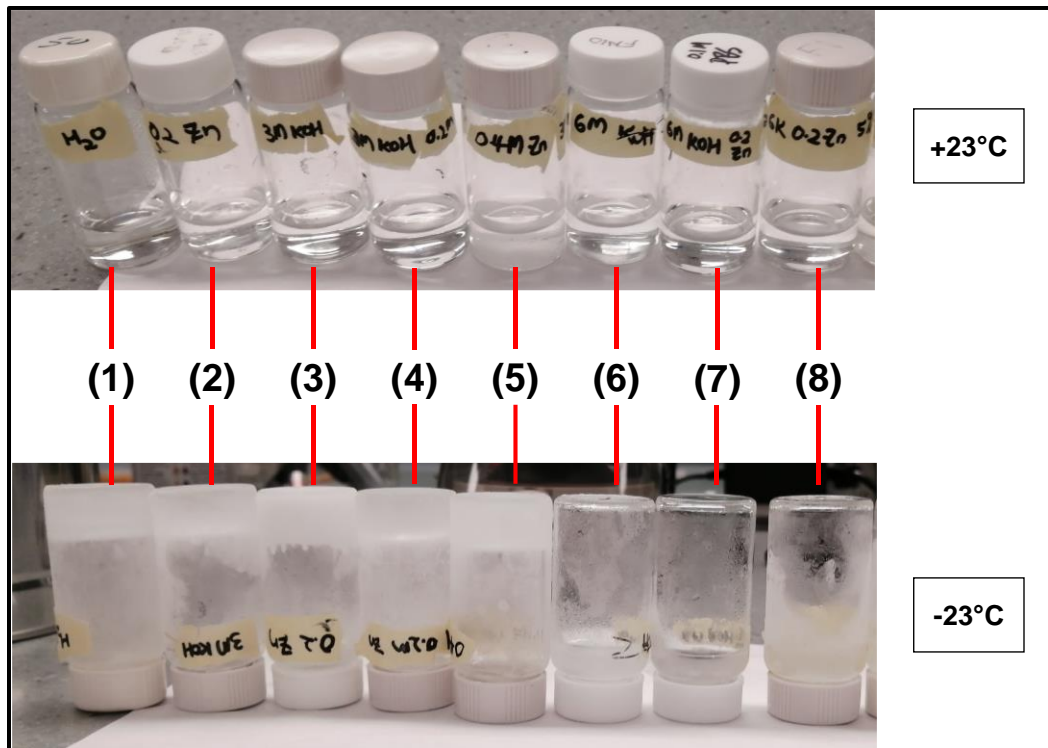
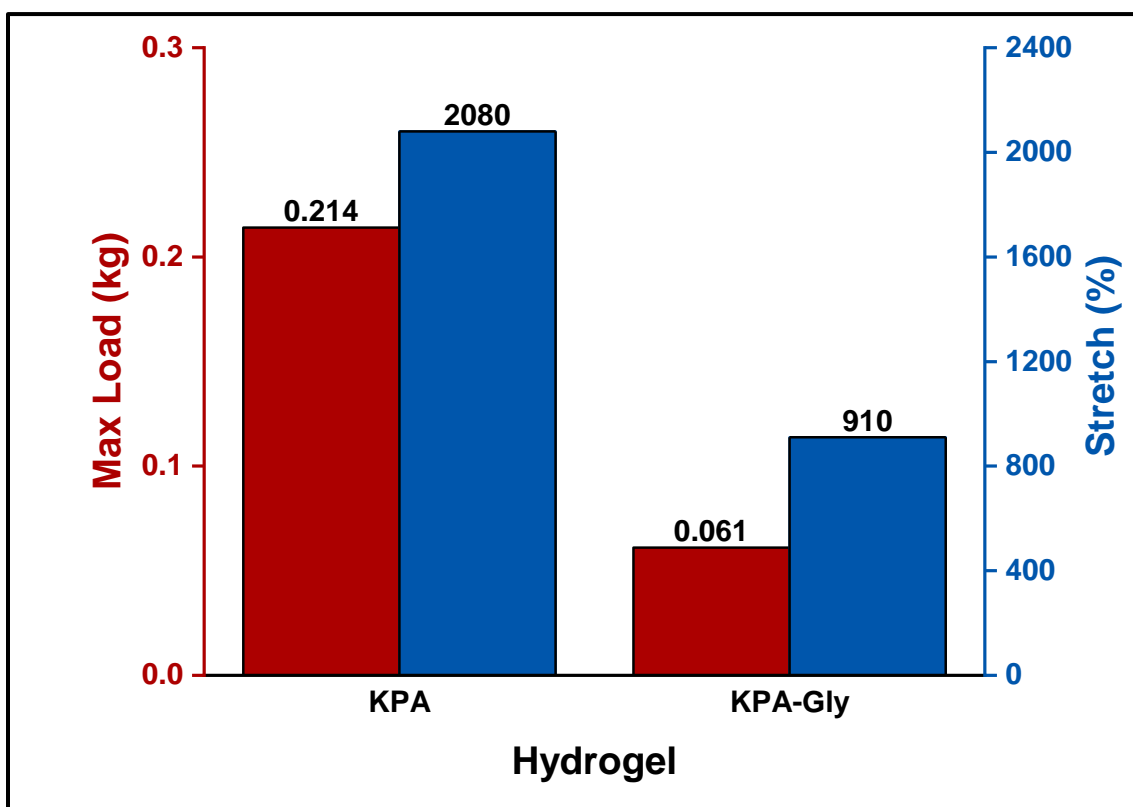


Table 4.6.1: Chemical compositions of the prepared sample to study the antifreeze properties of the electrolyte system and not the hydrogel.

Sample	Chemical compositions
1	Distilled water
2	0.2 M Zn(Ac) ₂
3	3.0 M KOH
4	3.0 M KOH with 0.2 M Zn(Ac) ₂
5	3.0 M KOH with 0.4 M Zn(Ac) ₂
6	6.0 M KOH
7	6.0 M KOH with 0.2 M Zn(Ac) ₂
8	6.0 M KOH, 0.2 M Zn(Ac) ₂ , 5% vol glycerol

We had approached analytical laboratories in Canada that offer a cryo-differential scanning calorimetry services to estimate the onset temperature of crystallization of all hydrogels and their respective liquid fractions. This would greatly help us identify an exact freezing point for formulations used in this work through precise analytical method. However, due to the highly alkaline nature of our samples, there is a risk of damaging the expensive crucible used to hold the analytes during the test. Hence, the tests could not be carried out.

Figure 4.6.3: Bar chart of the max load (red) and percentage of stretch (blue) of KPA and KPA-Gly.



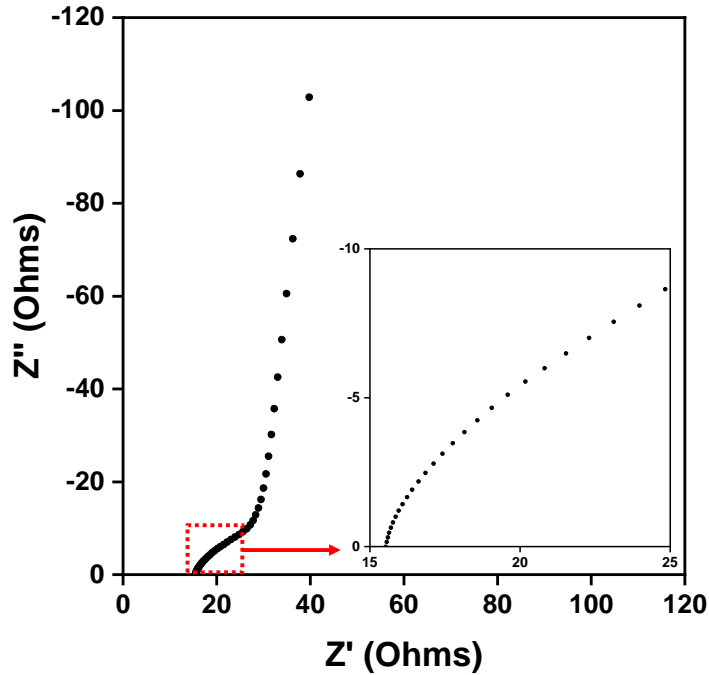
Similar tensile strength tests were treated to KPA and KPA-Gly to assess the mechanical properties of these newly synthesized hydrogels. From Figure 4.6.3, KPA-Gly

was both weaker and less stretchable when compared to the KPA. This is because the amount of MBAA crosslinker used for KPA-Gly (0.0945 g) was much higher than KPA (0.0336 g). Recall that MBAA acts as a chemical crosslinker, and they cannot be reformed once broken (section 1.3). In the case of KPA-Gly, since the amount of MBAA used was so much higher, the hydrogel became weak and brittle, ultimately weakening its mechanical properties.

4.7 Charge Transport Properties Analysis

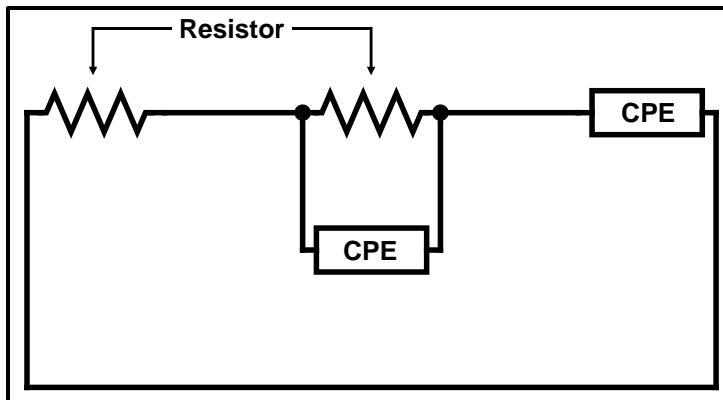
KPA and KPA-Gly had been chosen as our final formulations in this project and were subjected to thorough electrochemical analysis. As such, the total ionic conductivity and the charge transfer characteristics of these two electrolytes were evaluated according to procedure described in section 3.4. For the low-temperature analysis, it has to be clarified that these tests can only be carried in the freezer set to one temperature, making it difficult to collect experimental data at varying temperatures below the freezing point of water (0°C).

Figure 4.7.1: Nyquist plot of KPA without any elongation recorded at room temperature (23°C)



Let's start from the discussion of Nyquist plot and the overall ionic conductivity (σ) of the hydrogel extrapolated from the Nyquist plot. Figure 4.7.1 shows a Nyquist plot recorded for KPA at room temperature. All Nyquist plots recorded for both KPA and KPA-Gly (in room temperature or in the freezer) were very similar in terms of the shape. These spectra can be found in the appendix section. As mentioned in the theory section, Bandara and Mellandar defined the shape that will appeared in the Nyquist plot for an electrolyte material as a semicircle with a straight spike.³¹ However, this was not the case for our hydrogels. The shape recorded was a quarter circle (region within the red box) with a tilted spike (the region outside of the red box).

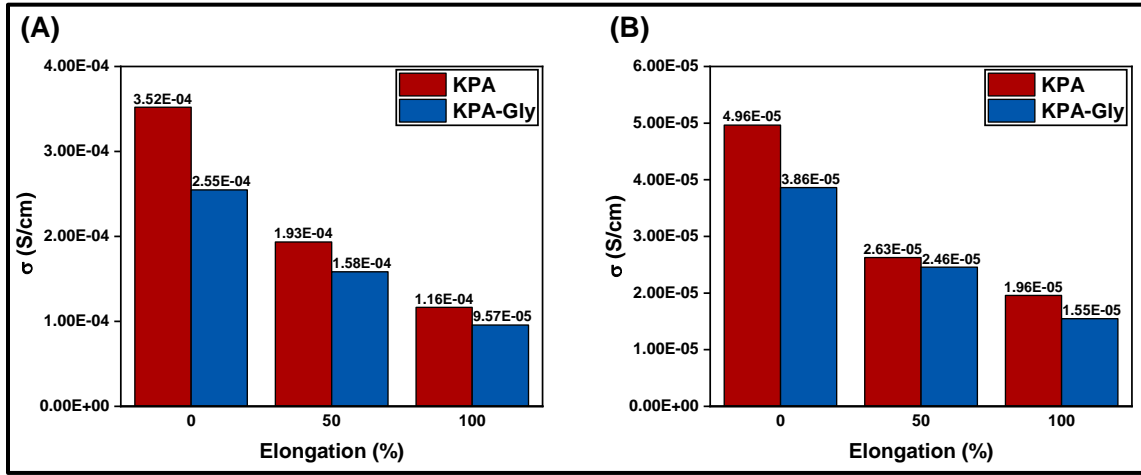
Figure 4.7.2: The circuit diagram used to describe all KPA and KPA-Gly spectra recorded. CPE stands for Constant Phase Element. It is a common element used to describe the behavior of a non-ideal capacitor.



Thus, a fitting program (ZView) was used to help us determine the bulk resistance values (R_{bulk}) of the hydrogels. To fit our data accurately, a different equivalent circuit (see Figure 4.7.2) was used instead of the equivalent circuit adopted by Bandara-Mellandar (equivalent circuit from Figure 2.6.3 in theory section).³¹ This is because the equivalent circuit defined by Bandara-Mellandar are more applicable for electrolyte material in an ideal situation (ideal capacitor or liquid electrolyte with extremely low resistance). The equivalent circuit shown in Figure 4.7.2 is more commonly used for real-world battery testing.

Then, these R_{bulk} values were used to calculate the hydrogels ionic conductivity through equation 2.6.4. The calculated values are summarized in the appendix section. For the ease of comparison, the ionic conductivities are shown as bar charts in Figure 4.7.3.

Figure 4.7.3: Bar charts of the fitted ionic conductivity values of charge transport properties of KPA and KPA-Gly at 23°C (A) and -23°C (B) versus percentage elongation.



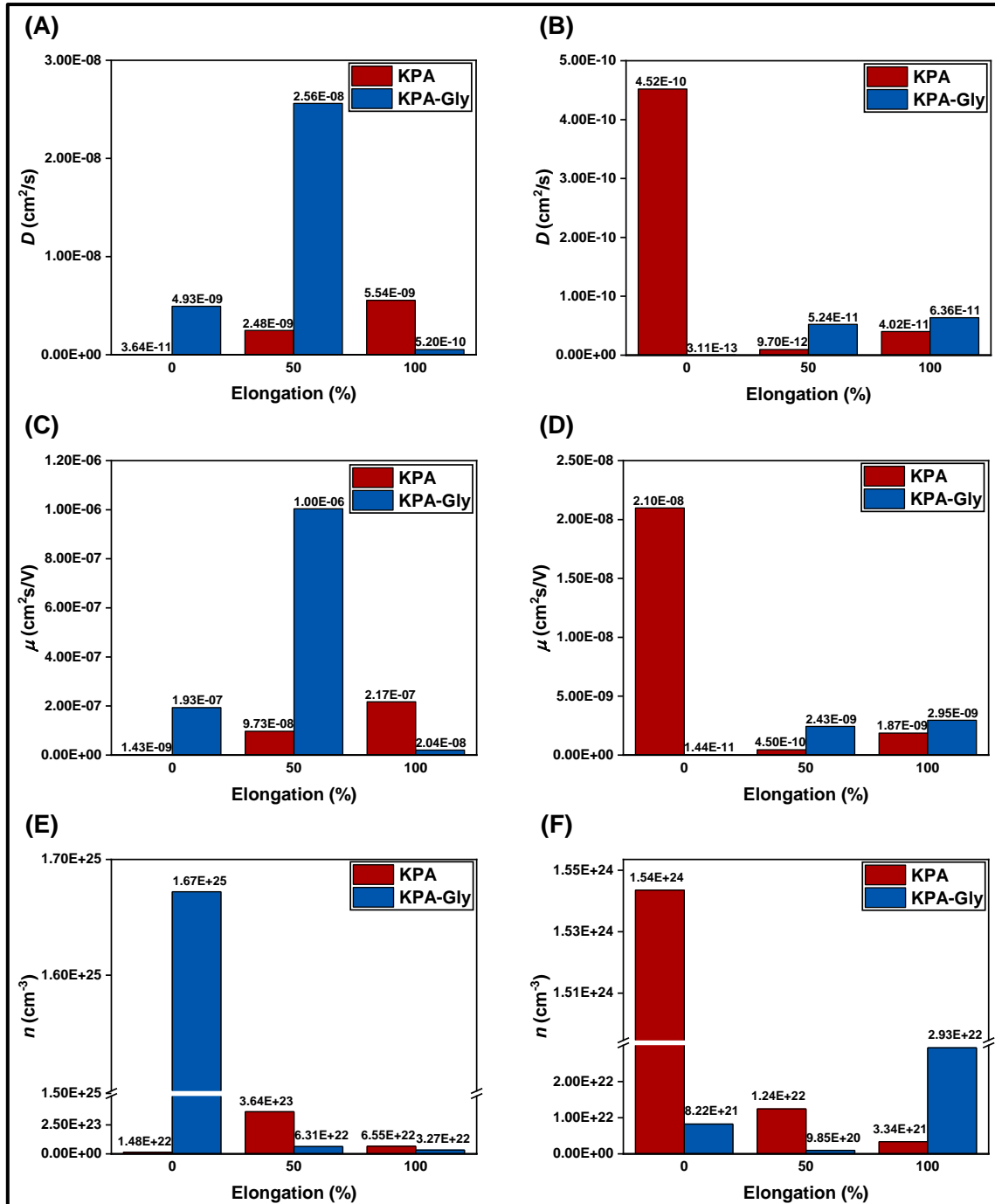
First and foremost, with increasing elongation, the ionic conductivities decreased very slightly for both KPA and KPA-Gly at both temperatures. However, these decrease in values were still within the same range of magnitude. This observed trend was very comparable to the impedance over time studies shown in sections 4.1 to 4.3, where the increased in impedance was proposed to be mainly due to an increased in distance travelled for the ions in the hydrogel to the polarized stainless steel. Both KPA and KPA-Gly also demonstrated a lower conductivity with decreasing temperature (comparing Figure 4.7.3(A) and (B)). This is a typical behaviour of ionic conductors related directly to the temperature-dependent kinetics of mobile ions.

Furthermore, comparing these two electrolytes, KPA-Gly (blue) showed overall lower conductivity than KPA (red) regardless of temperature. This drop in conductivity for the glycerol-containing electrolyte is associated with the formation of strong hydrogen bonds between glycerol with the OH^- ions in the electrolyte, limiting the movement of the ions. Although only 1 vol% of antifreeze was introduced, there was a visible drop in

conductivity. This effect was already observed by our previous group member and other research groups dealing with various antifreeze additives regardless of hydrogel formulations.²⁸ This also justifies that the introduction of antifreeze additives has to be at a minimal level so that it will not affect the conductivity of the hydrogel.

Since the formulation for KPA was identical to the work published by *Ivey et al*,^{36,37} comparison was made on the ionic conductivity values to their work. We realised that the ionic conductivity of KPA in our work (0.35 mS/cm) was about three orders of magnitude lower than what was reported by Ivey et al (about 180 mS/cm). This discrepancy in value might be caused by a few factors. First, since our hydrogel was formed in a sonication bath instead of heating in an oven, it might affect the polymerization process, giving us a less porous hydrogel, ultimately affecting the ionic conductivity of the hydrogel. Second, the shape of KPA synthesized in this work was very different. This heavily affects how the EIS experiments had to be carried out. Since EIS is a very sensitive method, the way the hydrogel was sandwiched between the stainless-steel electrodes will affect the shape of the Nyquist plot. Third, as mentioned before, hydrogels are extremely flexible, and their shape can be easily changed when force is applied (clamped). This characteristic makes it problematic to maintain consistent contact with the stainless-steel electrodes, increasing the difficulty to reproduce certain results. Nevertheless, an improvement in the low-temperature feature of the hydrogel was achieved via the incorporation of glycerol. This is considered a novelty and contribution to further improvement of this type of alkaline solid electrolytes.

Figure 4.7.4: Bar charts of all the calculated charge transport properties of KPA and KPA-Gly at 23°C (A, C, E) and -23°C (B, D, F)



Moving on to the charge transport properties of both KPA and KPA-Gly, the graphs of $\tan(\phi)$ against frequency were plotted. It is important to clarify here that the $\tan(\phi)$ values

were calculated based on experimental Z' and Z'' values, unlike the ionic conductivity values from the previous section where they were determined using a fitting program. The values for $\tan(\phi)$ and their respective frequencies were then used to calculate diffusion coefficient (D), average mobility of ion (μ), and charge density (n) based on equations 2.8.1 to 2.8.3. These calculated values are summarized in the appendix section.

Figure 4.7.4 shows the bar chart of all the calculated values. At first glance, the calculated D values have identical trend as μ . This is expected because these two properties are related by the Nernst Einstein relation. The electron charge, e , Boltzmann constant, k_b , and temperature, T , in the equations are constant (compare between equation 2.8.1 and 2.8.2).

Since the overall ionic conductivity of an electrolyte system is affected by these three charge transport properties, we were expecting to observe similar behaviours when comparisons were made between different elongations, temperature, or between different hydrogels (KPA and KPA-Gly). However, none of them displayed any similarity in trends. Hence, a second KPA sample was synthesized and treated with similar electrochemical impedance tests to find out the range errors of the calculated values. The mean and standard deviation for σ and D were summarized in Table 4.7.1, while μ and n in Table 4.7.2.

Table 4.7.1: The mean and standard deviation (Std. Dev) of σ and D for two KPA samples.

Elongation (%)	T (K)	σ (Scm ⁻¹)		D (cm ² s ⁻¹)	
		Mean	Std. Dev	Mean	Std. Dev
0	296.15	3.54×10^{-4}	1.72×10^{-6}	5.47×10^{-11}	1.84×10^{-11}
50		1.90×10^{-4}	3.92×10^{-6}	1.66×10^{-8}	1.41×10^{-8}
100		1.17×10^{-4}	3.57×10^{-7}	4.01×10^{-9}	1.53×10^{-9}
0	250.15	4.87×10^{-5}	9.24×10^{-7}	3.30×10^{-10}	1.22×10^{-10}
50		2.63×10^{-5}	7.37×10^{-8}	4.20×10^{-11}	3.23×10^{-11}
100		1.83×10^{-5}	1.30×10^{-6}	2.01×10^{-11}	2.01×10^{-11}

Table 4.7.2: The mean and standard deviation (Std. Dev) of μ and n for two KPA samples

Elongation (%)	T (K)	μ (cm ² sV ⁻¹)		n (cm ⁻³)	
		Mean	Std. Dev	Mean	Std. Dev
0	296.15	2.15×10^{-9}	7.20×10^{-10}	1.16×10^{24}	3.84×10^{23}
50		6.50×10^{-7}	5.52×10^{-7}	6.69×10^{21}	5.73×10^{21}
100		1.57×10^{-7}	6.00×10^{-8}	5.43×10^{21}	2.09×10^{21}
0	250.15	1.53×10^{-8}	5.65×10^{-9}	2.28×10^{22}	8.02×10^{21}
50		1.95×10^{-9}	1.50×10^{-9}	2.06×10^{23}	1.58×10^{23}
100		9.33×10^{-10}	9.33×10^{-10}	7.11×10^{27}	7.11×10^{27}

From Table 4.7.1 and 4.7.2, besides the values for ionic conductivity, the calculated charge transport properties had extremely large errors. This is consistent with other literature that tried to use the model from Bandara and Mellandar to calculate charge transport properties of hydrogels.³⁸ The large errors might be once again caused by the inconsistent contact between the hydrogels and the stainless steel. This is particularly problematic with managing a moving medium that was squeezed and had changing geometry that was difficult to measure.

All quantities estimated via analysis of impedance spectra were compared to polymer based on polyethylene oxide (PEO) and polyacrylonitrile (PAN) matrix with Li salt as ion conducting fraction. The average ionic conductivity of these PEO and PAN-based electrolyte has an overall range of magnitude at 10^{-5} S/cm.^{31,38} Although the reference material is chemically different than hydrogels investigated in this project, there are no data available for alkaline hydrogels that have composition comparable to our materials. For this reason, results presented in this section will be only discussed in relevance to our modifications (effect of glycerol and temperature).

As such, going back to the bar charts in Figure 4.7.4, comparisons were made for values of D at room temperature. They varied within 10^{-8} to 10^{-11} cm²/s, which is slightly lower range than referenced data ($D = 10^{-10}$ cm²/s for PAN-based and 10^{-8} cm²/s for PEO-based). These differences are negligible, and the ion transport coefficients are comparable to values reported for state-of-the-art polymer electrolytes in commercial Li-ion battery. With respect to temperature effect, slightly lower D values are obtained which is expected given the temperature-driven dependence. There is no clear trend related to effect of glycerol addition, perhaps due to a very low content of glycerol (1 vol%), which will not introduce significant variation in electrical parameters. The difference between D values for KPA and KPA-Gly samples are expected to lay within the experimental error, therefore further speculations could potentially lead us to overinterpretation.

Similar to the diffusion coefficients, ionic mobilities calculated in this work were compared to one reported for polymer electrolyte for Li-ion battery. At room temperature, ionic mobility of our hydrogel (between 10^{-6} to 10^{-9}) remained comparable to PAN-based (10^{-9}) but not PEO-based (10^{-3}) hydrogels. Last but not least, the calculated charge density,

n, is higher (between 10^{22} to 10^{25}) than the range reported for PAN-based (10^{20}) and PEO-based (10^{13}) hydrogel. A very general conclusion that can be drawn by comparing these values is that both KPA and KPA-Gly contain much more ions, which holds promise for being a suitable material for metal-air battery applications. However, the mobility of these ions is still limited or not as efficient to migrate towards the polarized electrodes.

5 Conclusion and Future Work

The overall goal of the project was to synthesize a solid electrolyte that can function at low temperature for ZABs. The initial formulation of polymer matrix chosen to realize this goal was a copolymerization between polyacrylamide and potassium polyacrylate. MBAA was added to crosslink between these polymer chains. The electrolyte system for alkaline ZABs (6.0 M KOH and 0.2 M Zn(Ac)₂) was added before the polymerization step to reduce the overall synthesis time of this hydrogel. Three different variants of cellulose were incorporated into the hydrogel to further improve the stretchability of hydrogel. Addition of cellulose into the polymer matrix improved the stretchability of the hydrogels in general. However, agglomerates were formed during the addition, impeding the movement of ions in the hydrogel, and reducing the overall conductivity of the hydrogels. Through a few simple experiments and analysis, we realized that acrylamide is not suitable for this project as it will readily decompose to acrylic acid and ammonia in extremely basic condition. This leads to the removal of acrylamide monomer in our initial formulation.

After changing our formulation, 1 vol% of glycerol was incorporated to KPA to make KPA-Gly. Although cryo-DSC cannot be carried out to accurately determine the freezing point of these hydrogels, simple experiments in the freezer available in the department gave us insight that the antifreeze properties had been improved from -25°C to -80°C. Electrochemical Impedance Spectroscopy (EIS) was used to study the conductivity and charge transport properties of KPA and KPA-Gly. The model proposed by Bandara and Mellandar was used to calculate the diffusion coefficient, average mobility of ions, and the density of ions present in these two hydrogels.³¹ We learnt that there were a lot of factors

that will affect the results of these electrochemical properties of the hydrogel, affecting the accuracy of these values.

Moving forward for this project, a lot of work still can be done to improve the functionality of the hydrogels. First and foremost, scanning electron microscopy images of KPA synthesized from different methodology (polymerization through heat or sonication) can be recorded. This analysis will give us an idea on the porosity of the hydrogel, further improving the ionic conductivity of these hydrogel by choosing a more suitable method.

Besides that, improvement has to be made on the electrochemistry setup. As mentioned before, it is difficult to accurately record the Nyquist plot of the hydrogels since they are extremely soft. We need to design a setup that does not involve clamping the hydrogels but still able to hold the hydrogels firmly in place during the EIS experiments. This setup also needs to be small enough to fit the freezer available in the department for low temperature experiments and have at least one degree of freedom so that Nyquist plots of the hydrogels after elongation can be recorded. To account for the inaccuracy of these results, multiple Nyquist plots of KPA and KPA-Gly should be recorded.

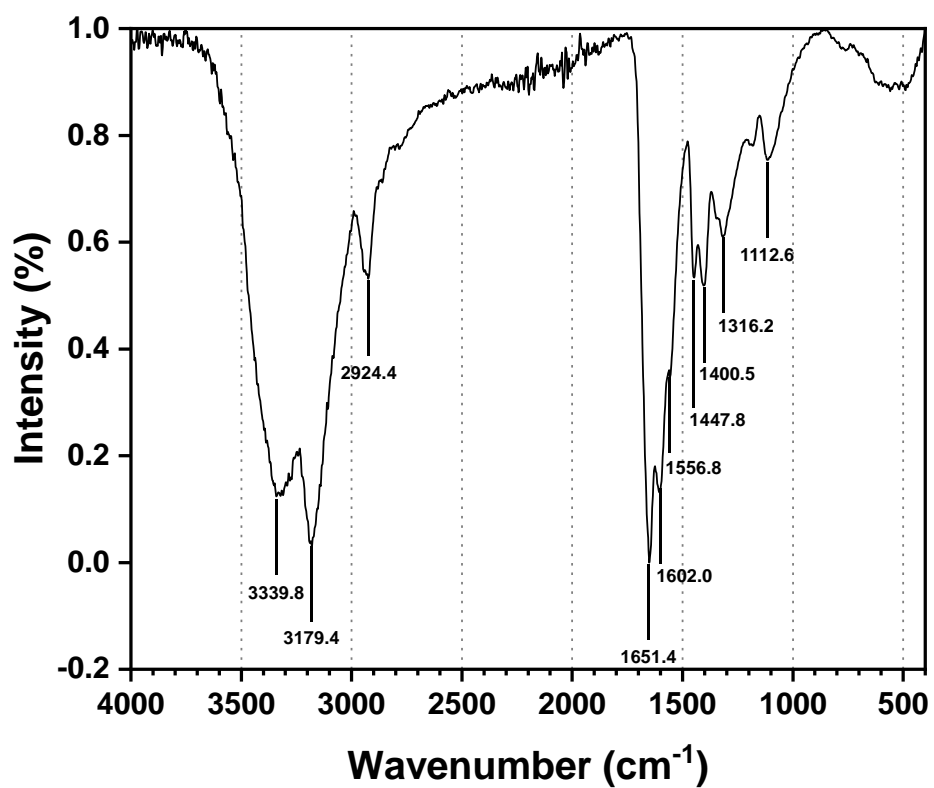
Multiple different models for calculation of charge transport properties of hydrogels should also be explored. For example, Chan and Kammer tried to investigate the charge transport properties of PEO-based hydrogel through its dielectric properties (ϵ_r).²⁷ Adopting the Cole-Cole and Havriliak-Negami model, Wang *et al* were able to gain an in depth understanding on the capacitive behavior of their acrylic material, aiding them into designing a suitable material for supercapacitors.³⁹ Simulation of the charge transport properties can also be carried out through simulation program designed for electrical

engineers, such as COMSOL. These simulations allow us to visualize the movement of the ions in different conditions where experiment cannot be carried out (such as in extremely low temperature in our case).

6 Appendix

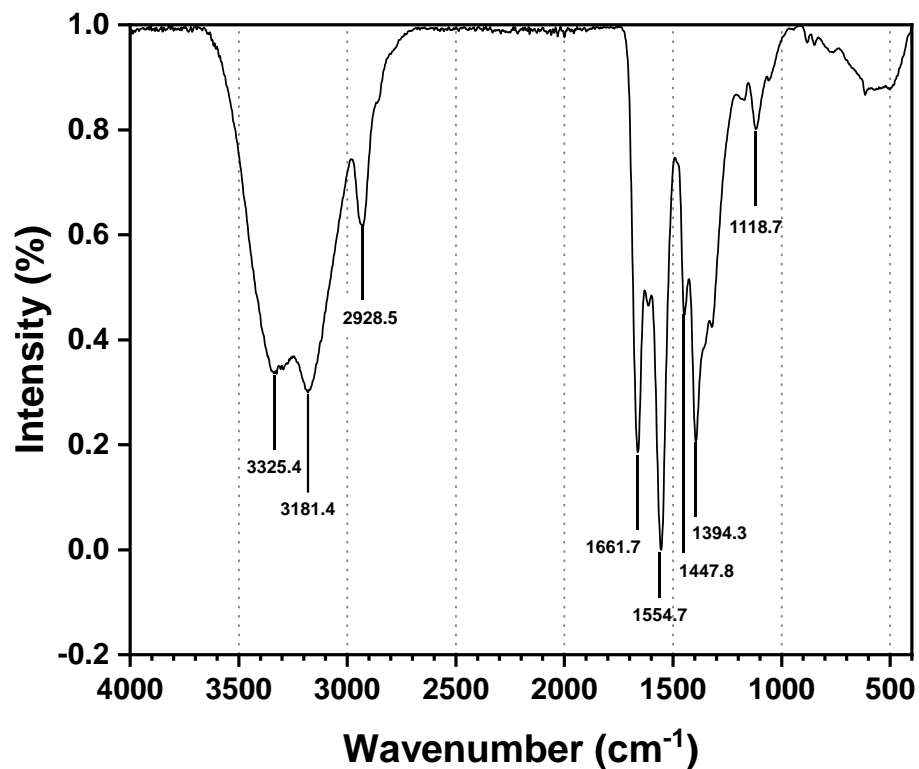
6.1 FTIR Spectra

Figure 6.1.1: FTIR spectrum of $B_{0.0}Z_{0.2}$



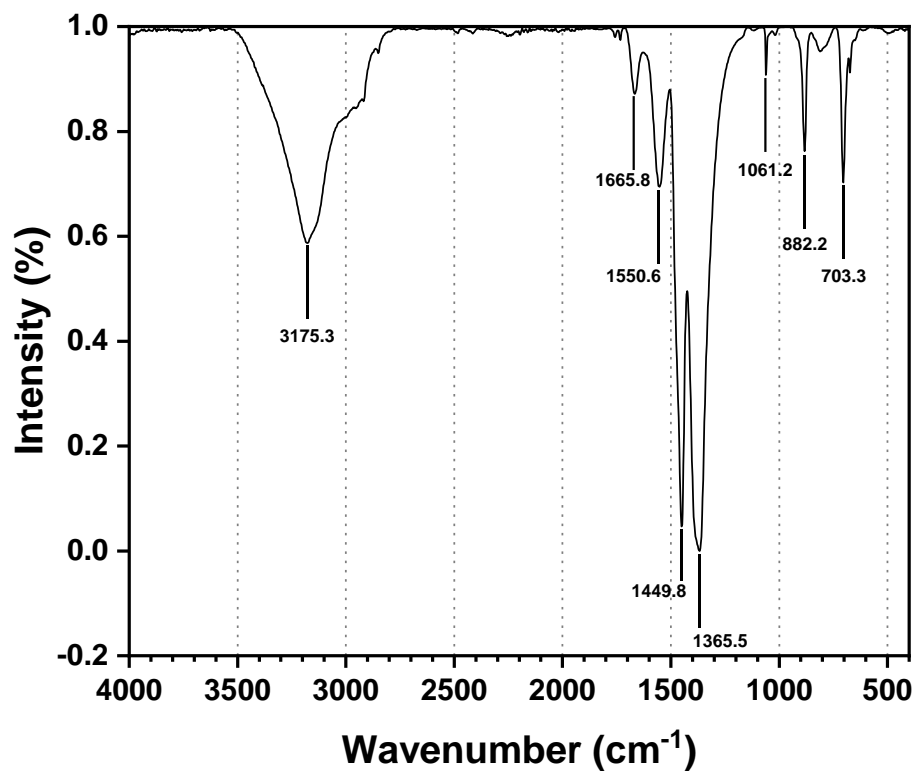
Wavenumber (cm ⁻¹)	Assignments
1112.6	C-O stretch
1316.2	C-O stretch
1400.5	O-H bend
1447.8	C-H bend
1556.8	N-H bend
1602.0	C=C stretch
1651.4	C=O stretch
2924.4	C-H stretch
3179.4	N-H stretch
3339.8	N-H stretch

Figure 6.1.2: FTIR Spectrum of $B_{1.5}Z_{0.2}$



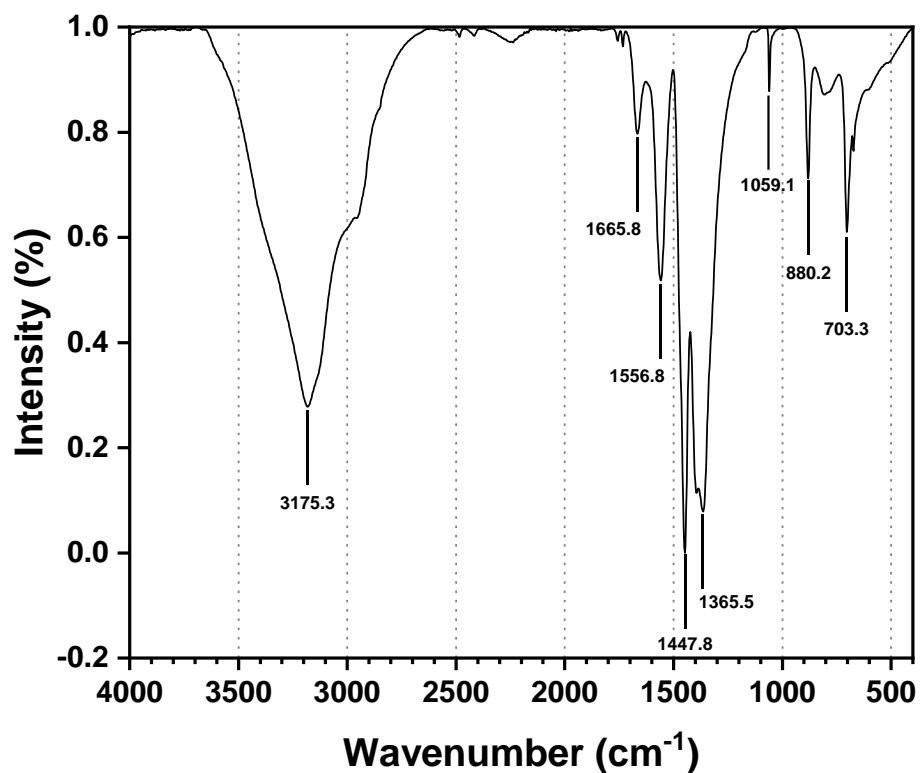
Wavenumber (cm ⁻¹)	Assignments
1118.7	C-O stretch
1394.3	O-H bend
1447.8	C-H bend
1554.7	N-H bend
1661.7	C=O stretch
2928.5	C-H stretch
3181.4	N-H stretch
3325.4	N-H stretch

Figure 6.1.3: FTIR spectrum for B_{3.0}Z_{0.2}



Wavenumber (cm ⁻¹)	Assignments
703.3	C=C bend
882.2	C=C bend
1061.2	C-N bend
1365.5	O-H bend
1449.8	C-H bend
1550.6	N-H stretch
1665.8	C=O stretch
3175.3	N-H stretch

Figure 6.1.4: FTIR spectrum for B_{4.5}Z_{0.2}



Wavenumber (cm ⁻¹)	Assignments
703.3	C=C bend
880.2	C=C bend
1059.1	C-N bend
1365.5	O-H bend
1447.8	C-H bend
1556.8	N-H bend
1665.8	C=O stretch
3175.3	O-H stretch

6.2 Experimental Nyquist plot

Figure 6.2.1: Nyquist plot of KPA at 23°C

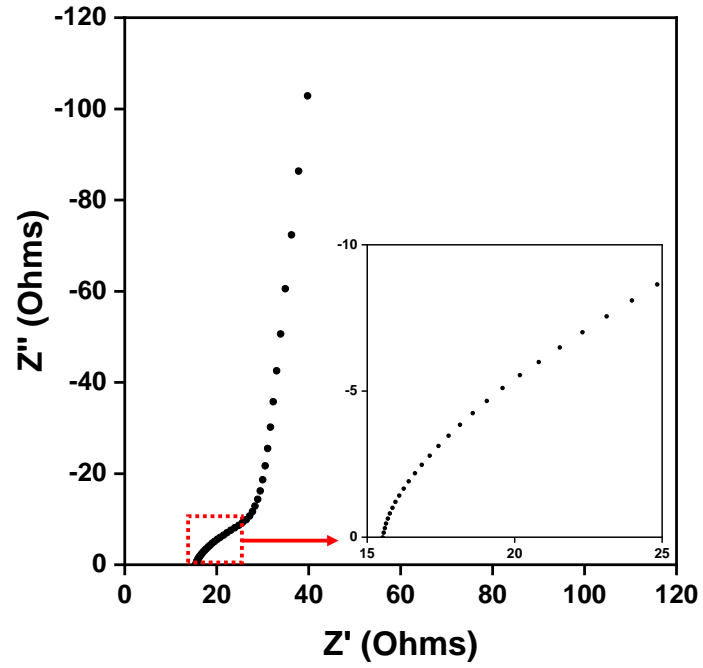


Figure 6.2.2: Nyquist plot of KPA at 23°C after 50% elongation

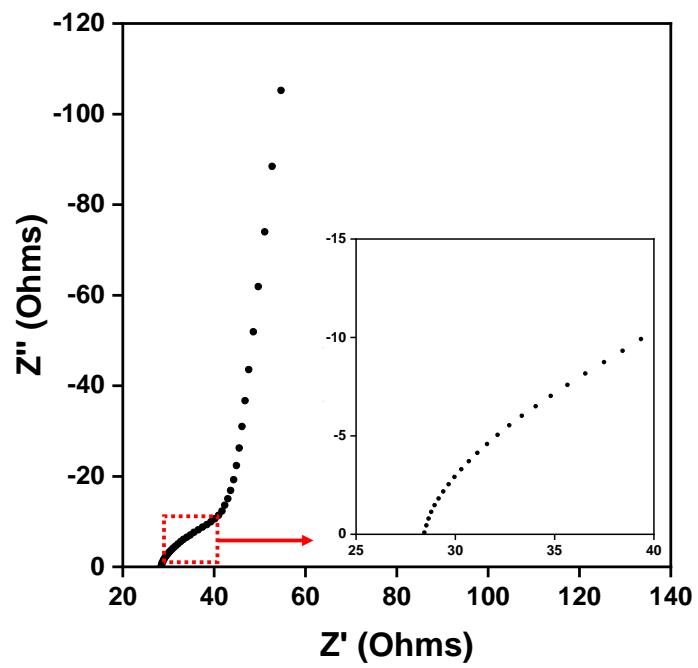


Figure 6.2.3: Nyquist plot of KPA at 23°C after 100% elongation

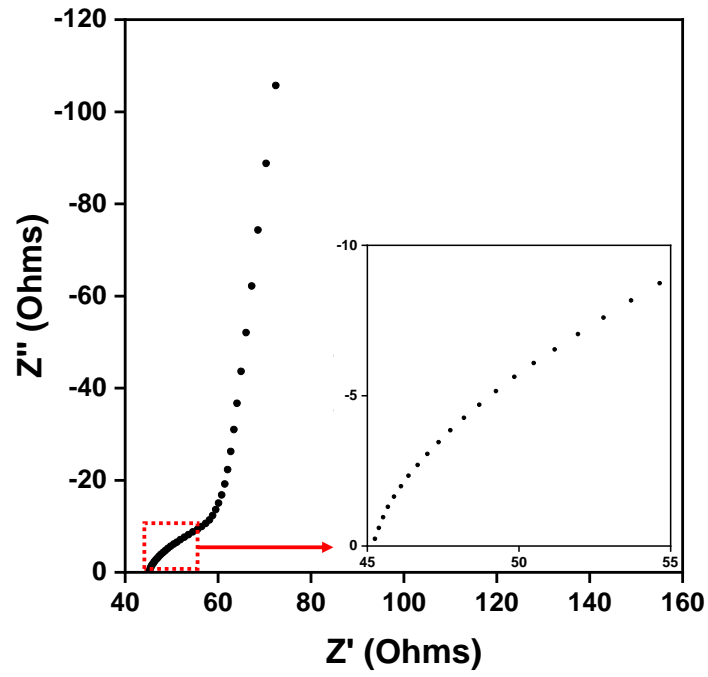


Figure 6.2.4: Nyquist plot of KPA at -23°C

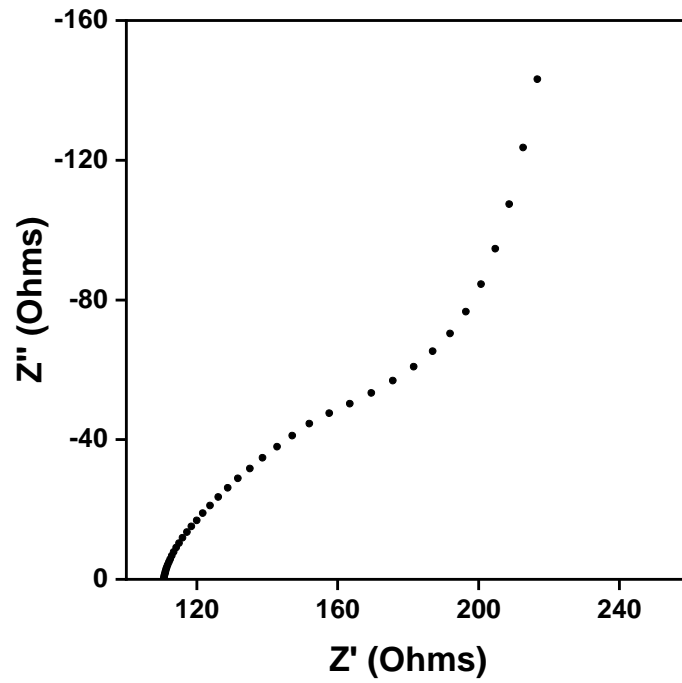


Figure 6.2.5: Nyquist plot of KPA at -23°C after 50% elongation

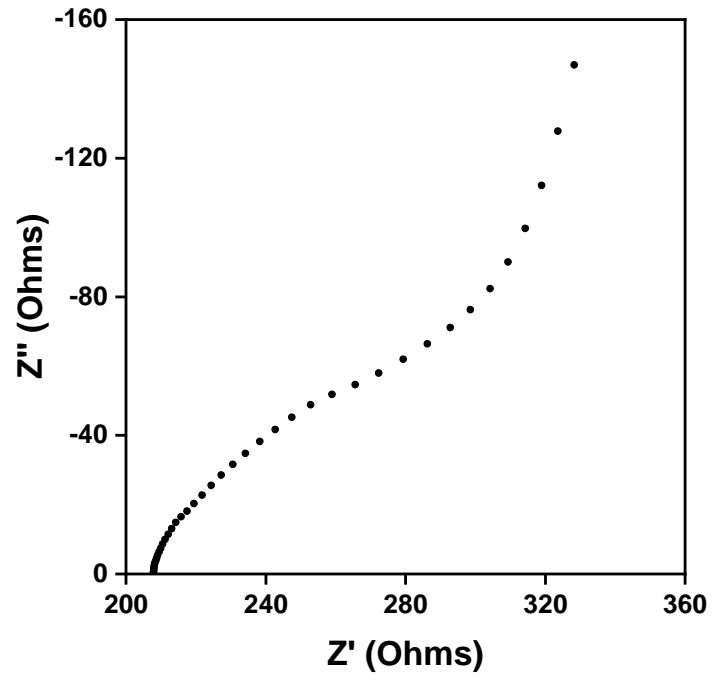


Figure 6.2.6: Nyquist plot of KPA at -23°C after 100% elongation

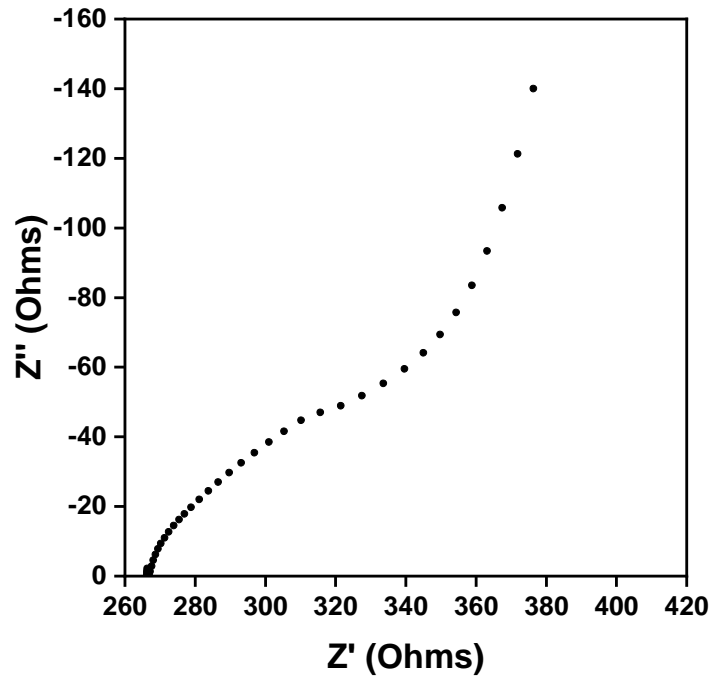


Figure 6.2.7: Nyquist plot of KPA-Gly at 23°C

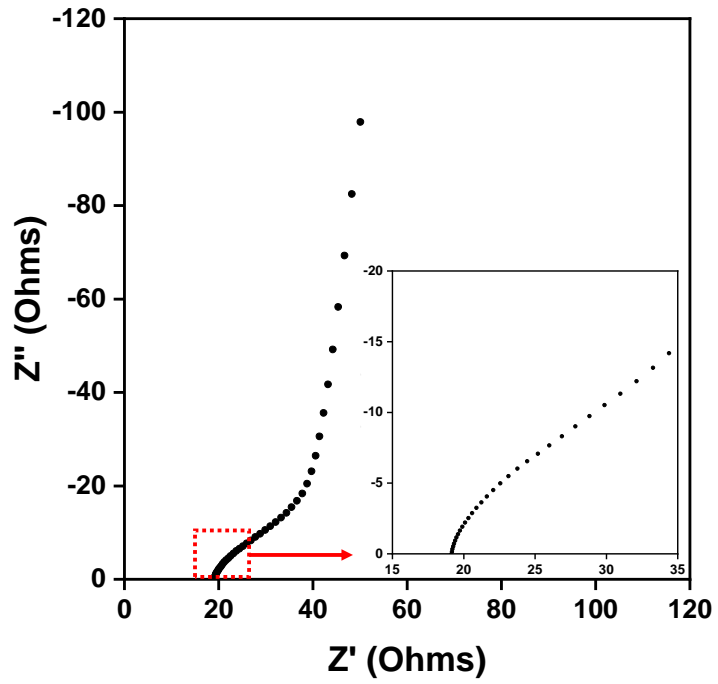


Figure 6.2.8: Nyquist plot of KPA-Gly at 23°C after 50% elongation

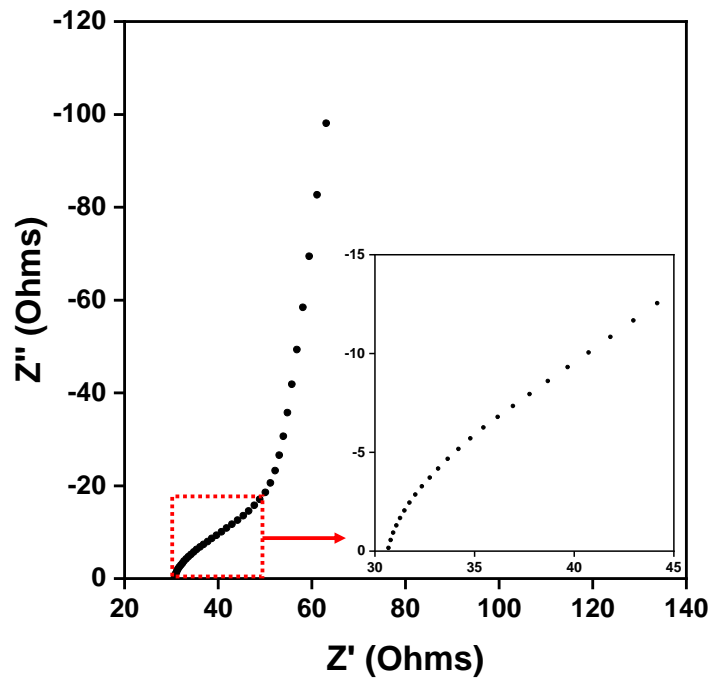


Figure 6.2.9: Nyquist plot of KPA-Gly at 23°C after 100% elongation

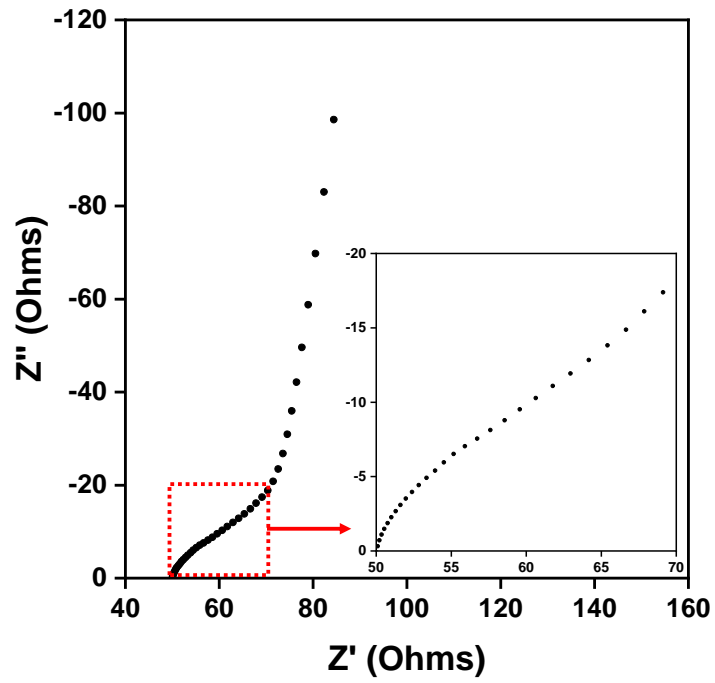


Figure 6.2.10: Nyquist plot of KPA-Gly at -23°C

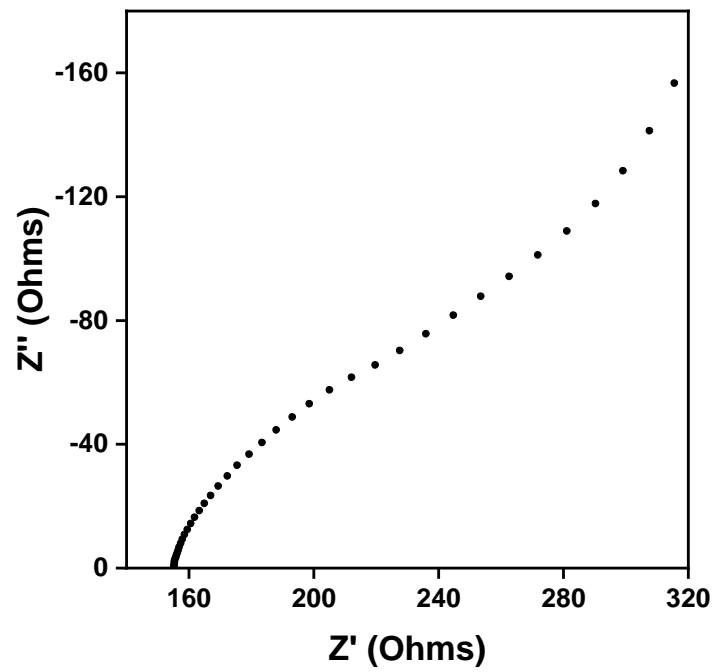


Figure 6.2.11: Nyquist plot of KPA-Gly at -23°C after 50% elongation

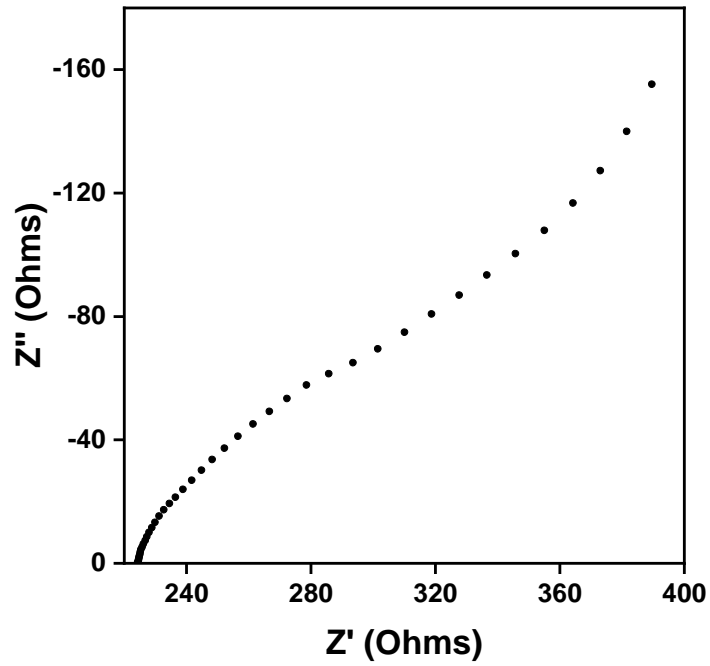


Figure 6.2.12: Nyquist plot of KPA-Gly at -23°C after 100% elongation

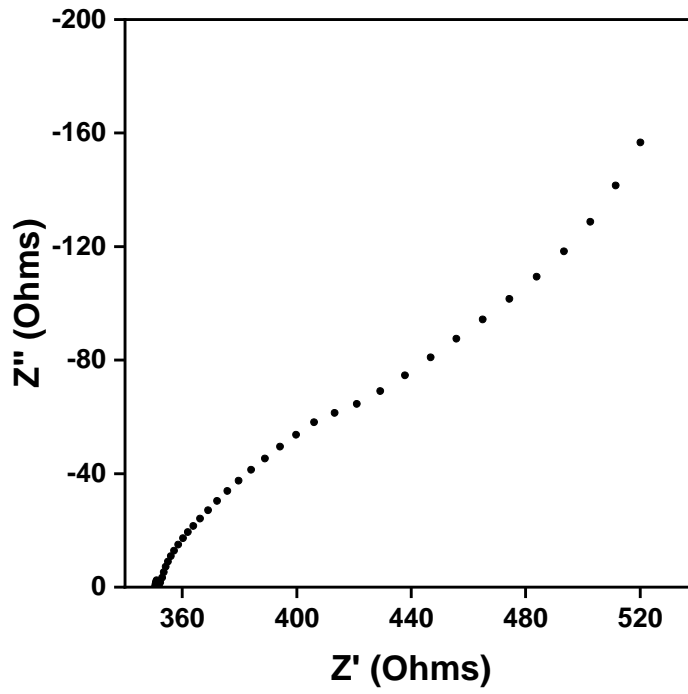


Table 6.2.1: Values of ionic conductivity of KPA based on R_{bulk} determine through fitting

Elongation (%)	T (K)	R_{bulk} (Ω)	σ (Scm^{-1})
0	296.15	29.91	3.52×10^{-4}
50		43.75	1.93×10^{-4}
100		60.77	1.16×10^{-4}
0	250.15	212.10	4.96×10^{-5}
50		322.40	2.63×10^{-5}
100		361.12	1.96×10^{-5}

Table 6.2.2: Values of ionic conductivity of KPA-Gly based on R_{bulk} determine through fitting

Elongation (%)	T (K)	R_{bulk} (Ω)	σ (Scm^{-1})
0	296.15	41.34	2.55×10^{-4}
50		53.46	1.58×10^{-4}
100		73.94	9.57×10^{-5}
0	250.15	272.60	3.86×10^{-5}
50		344.40	2.46×10^{-5}
100		457.80	1.55×10^{-5}

6.3 Calculation of Charge Transport Properties

Table 6.3.1: Values of $\tan(\phi)$ extrapolated from plotting Z'/Z'' against frequency of KPA

Elongation (%)	T (K)	$\tan(\phi)$	$\sqrt{\delta}$	f (s ⁻¹)	t_2 (s)
0	296.15	1257.49	2514.98	46440	2.15×10^{-5}
50		344.10	688.20	17770	5.63×10^{-5}
100		295.29	590.58	21530	4.64×10^{-5}
0	250.15	579.97	1159.94	26120	3.83×10^{-5}
50		1515.31	3030.61	26120	3.83×10^{-5}
100		758.89	1517.77	6812	1.47×10^{-4}

Table 6.3.2: Calculated values of D , μ , and n of KPA

Elongation (%)	T (K)	D (cm ² s ⁻¹)	μ (cm ² sV ⁻¹)	n (cm ⁻³)
0	296.15	3.64×10^{-11}	1.43×10^{-9}	1.54×10^{24}
50		2.48×10^{-9}	9.73×10^{-8}	1.24×10^{22}
100		5.54×10^{-9}	2.17×10^{-7}	3.34×10^{21}
0	250.15	4.52×10^{-10}	2.10×10^{-8}	1.48×10^{22}
50		9.70×10^{-12}	4.50×10^{-10}	3.64×10^{23}
100		4.02×10^{-11}	1.87×10^{-9}	6.55×10^{22}

Table 6.3.3: Values of $\tan(\phi)$ extrapolated from plotting Z'/Z'' against frequency of KPA-Gly

Elongation (%)	T (K)	$\tan(\phi)$	$\sqrt{\delta}$	f (s ⁻¹)	t_2 (s)
0	296.15	368.47	736.94	46440	2.15×10^{-5}
50		191.99	383.97	17770	5.63×10^{-5}
100		533.67	1067.34	21530	4.64×10^{-5}
0	250.15	3581.81	7163.63	26120	3.83×10^{-5}
50		1042.79	2085.58	31640	3.16×10^{-5}
100		710.02	1420.03	8252	1.21×10^{-4}

Table 6.3.4: Calculated values of D , μ , and n of KPA-Gly

Elongation (%)	T (K)	D (cm ² s ⁻¹)	μ (cm ² sV ⁻¹)	n (cm ⁻³)
0	296.15	4.93×10^{-9}	1.93×10^{-7}	8.22×10^{21}
50		2.56×10^{-8}	1.00×10^{-6}	9.85×10^{20}
100		5.20×10^{-10}	2.04×10^{-8}	2.93×10^{22}
0	250.15	3.18×10^{-13}	1.44×10^{-11}	1.67×10^{25}
50		5.24×10^{-11}	2.43×10^{-9}	6.31×10^{22}
100		6.36×10^{-11}	2.95×10^{-9}	3.27×10^{22}

7 References

1. Lamb, W. F. *et al.* A review of trends and drivers of greenhouse gas emissions by sector from 1990 to 2018. *Environ. Res. Lett.* **16**, (2021).
2. Sonoc, A. & Jeswiet, J. A review of lithium supply and demand and a preliminary investigation of a room temperature method to recycle lithium ion batteries to recover lithium and other materials. *Procedia CIRP* **15**, 289–293 (2014).
3. Clark, S., Latz, A. & Horstmann, B. A review of model-based design tools for metal-air batteries. *Batteries* **4**, 1–26 (2018).
4. Pascal, H., Conrad, L. B., Miloš, V., Anna, K. D., Arnd, G., Jürgen, J. & Philipp, A. A rechargeable room-temperature sodium superoxide (NaO₂) battery. *Nat. Commun.* **12**, 228–232 (2013).
5. Vardar, G. *et al.* Electrochemistry of magnesium electrolytes in ionic liquids for secondary batteries. *ACS Appl. Mater. Interfaces* **6**, 18033–18039 (2014).
6. Yang, S. & Knickle, H. Design and analysis of aluminum/air battery system for electric vehicles. *J. Power Sources* **112**, 162–173 (2002).
7. Pei, P., Wang, K. & Ma, Z. Technologies for extending zinc-air battery's cyclelife: A review. *Appl. Energy* **128**, 315–324 (2014).
8. Korde, J. M. & Kandasubramanian, B. Naturally biomimicked smart shape memory hydrogels for biomedical functions. *Chem. Eng. J.* **379**, 122430 (2020).
9. Wu, D., Xu, J., Chen, Y., Yi, M. & Wang, Q. Gum Arabic: A promising candidate for the construction of physical hydrogels exhibiting highly stretchable, self-healing and tensility reinforcing performances. *Carbohydr. Polym.* **181**, 167–174 (2018).

10. Talebian, S. *et al.* Self-Healing Hydrogels: The Next Paradigm Shift in Tissue Engineering? *Adv. Sci.* **6**, (2019).
11. Ahmed, E. M. Hydrogel: Preparation, characterization, and applications: A review. *J. Adv. Res.* **6**, 105–121 (2015).
12. Peng, Q. *et al.* Recent advances in designing conductive hydrogels for flexible electronics. *InfoMat* **2**, 843–865 (2020).
13. Lao-atiman, W. *et al.* Model-based analysis of an integrated zinc-air flow Battery/Zinc Electrolyzer System. *Front. Energy Res.* **7**, 1–15 (2019).
14. Xu, M., Ivey, D. G., Xie, Z. & Qu, W. Rechargeable Zn-air batteries: Progress in electrolyte development and cell configuration advancement. *J. Power Sources* **283**, 358–371 (2015).
15. Lee, J., Hwang, B., Park, M. S. & Kim, K. Improved reversibility of Zn anodes for rechargeable Zn-air batteries by using alkoxide and acetate ions. *Electrochim. Acta* **199**, 164–171 (2016).
16. Li, Y. *et al.* Advanced zinc-air batteries based on high-performance hybrid electrocatalysts. *Nat. Commun.* **4**, 1–7 (2013).
17. Miao, H. *et al.* All-solid-state flexible zinc-air battery with polyacrylamide alkaline gel electrolyte. *J. Power Sources* **450**, 227653 (2020).
18. Gilliam, R. J., Graydon, J. W., Kirk, D. W. & Thorpe, S. J. A review of specific conductivities of potassium hydroxide solutions for various concentrations and temperatures. *Int. J. Hydrogen Energy* **32**, 359–364 (2007).
19. Zhao, S. *et al.* A New Solid-State Zinc–Air Battery for Fast Charge. *Energy Technol.* **8**, 1–8 (2020).

20. Chen, R. *et al.* A Flexible and Safe Aqueous Zinc-Air Battery with a Wide Operating Temperature Range from -20 to 70 °C. *ACS Sustain. Chem. Eng.* **8**, 11501–11511 (2020).
21. Ma, L. *et al.* Super-Stretchable Zinc–Air Batteries Based on an Alkaline-Tolerant Dual-Network Hydrogel Electrolyte. *Adv. Energy Mater.* **9**, 1–8 (2019).
22. Chen, Z. *et al.* Gel polymer electrolyte with MXene to extend cycle lifespan of flexible and rechargeable Zinc–Air batteries. *J. Power Sources* **523**, 231020 (2022).
23. Li, Z., Li, X., Jiang, Y., Ding, Q. & Han, W. Nanocellulose composite gel with high ionic conductivity and long service life for flexible zinc-air battery. *Polym. Test.* **104**, 107380 (2021).
24. Zhang, Y. *et al.* Alkaline sodium polyacrylate-starch hydrogels with tolerance to cold conditions for stretchable zinc-air batteries. *Compos. Part B Eng.* **224**, 109228 (2021).
25. Song, Z. *et al.* A Rechargeable Zn–Air Battery with High Energy Efficiency and Long Life Enabled by a Highly Water-Retentive Gel Electrolyte with Reaction Modifier. *Adv. Mater.* **32**, 1–10 (2020).
26. Zhao, N. *et al.* Flexible Hydrogel Electrolyte with Superior Mechanical Properties Based on Poly(vinyl alcohol) and Bacterial Cellulose for the Solid-State Zinc-Air Batteries. *ACS Appl. Mater. Interfaces* **11**, 15537–15542 (2019).
27. Chan, C. H. & Kammer, H. W. Impedance spectra of polymer electrolytes. *Ionics (Kiel)*. **23**, 2327–2337 (2017).
28. Thibodeau, J. & Ignaszak, A. A Flexible Ionic Polymer for “Soft Machines” –

- Where is the Low Temperature Limit? *ChemElectroChem* **9**, (2022).
29. Lu, C. *et al.* Ultra-strong hydroxypropyl cellulose/polyvinyl alcohol composite hydrogel by combination of triple-network and mechanical training. *Int. J. Biol. Macromol.* **184**, 200–208 (2021).
 30. Sun, Y. *et al.* Highly Conductive and Reusable Electrolyte Based on Sodium Polyacrylate Composite for Flexible Al-Air Batteries. *J. Electrochem. Soc.* **167**, 080502 (2020).
 31. Bandara, T. M. W. J., Dissanayake, M. A. K. L., Albinsson, I. & Mellander, B. E. Mobile charge carrier concentration and mobility of a polymer electrolyte containing PEO and Pr4N⁺ I⁻ using electrical and dielectric measurements. *Solid State Ionics* **189**, 63–68 (2011).
 32. Furman, O. S., Teel, A. L. & Watts, R. J. Mechanism of base activation of persulfate. *Environ. Sci. Technol.* **44**, 6423–6428 (2010).
 33. Reichle, R. A., McCurdy, K. G. & Hepler, L. G. Zinc Hydroxide: Solubility Product and Hydroxy-complex Stability Constants from 12.5–75 °C. *Can. J. Chem.* **53**, 3841–3845 (1975).
 34. Wang, Y. *et al.* A facile strategy for high performance recyclable polymer systems: Via dynamic metal ion crosslinking. *J. Mater. Chem. A* **7**, 3577–3582 (2019).
 35. Tan, M. J. *et al.* Acrylamide-derived freestanding polymer gel electrolyte for flexible metal-air batteries. *J. Power Sources* **400**, 566–571 (2018).
 36. Tran, T. N. T. *et al.* Compositional Effects of Gel Polymer Electrolyte and Battery Design for Zinc-Air Batteries. *Batter. Supercaps* **3**, 917–927 (2020).

37. Tran, T. N. T., Clark, M. P., Chung, H. J. & Ivey, D. G. Effects of Crosslinker Concentration in Poly(Acrylic Acid)-KOH Gel Electrolyte on Performance of Zinc-Air Batteries. *Batter. Supercaps* **3**, 409–416 (2020).
38. Arof, A. K., Amirudin, S., Yusof, S. Z. & Noor, I. M. A method based on impedance spectroscopy to determine transport properties of polymer electrolytes. *Phys. Chem. Chem. Phys.* **16**, 1856–1867 (2014).
39. Wang, H., Yang, L., Zhang, X. & Ang, M. H. Permittivity, loss factor and Cole-Cole model of acrylic materials for dielectric elastomers. *Results Phys.* **29**, 104781 (2021).

Curriculum Vitae

Candidate's full name:

Chun Keat Khor

Universities attended:

Bachelor of Science in Chemistry (Honours), University of New Brunswick

Publication:

- 1) N. A. Richard, C. K. Khor, S. M. Hetherington, S. L. Mills, A. Decken, C. A. Dyker. Iminophosphorano-Substituted Bispyridinylidenes: Redox Potentials and Substituent Constants from Tolman Electronic Parameters. *Chem. Eur. J.*, **26**, 17371– 17375 (2020).

Conference Presentations:

- 1) ^{15}N Chemical Shifts as a Predictor of the Relative Strength of Bispyridinylidene (BPY) Organic Reducing Agents. Science Atlantic ChemCon, Wolfville, Nova Scotia.